Università degli Studi di Napoli Federico II
Ph.D. Program in
Information Technology and Electrical Engineering
XXXV Cycle

Thesis for the Degree of Doctor of Philosophy

Automation of robot-assisted surgical procedures

by
Cristina Iacono

Advisor: Prof. Fanny Ficuciello

Scuola Politecnica e delle Scienze di Base
Dipartimento di Ingegneria Elettrica e delle Tecnologie dell'Informazione

per chi mi ha voluto bene sempre

Automation of robot-assisted surgical procedures

Ph.D. Thesis presented
for the fulfillment of the Degree of Doctor of Philosophy
in Information Technology and Electrical Engineering
by

Cristina Iacono

January 2024

Approved as to style and content by

Fanny Ficuciello Digitally signed by Fanny Ficuciello
DN: cn=Fanny Ficuciello, o=University of Naples Federico II, ou=University, email=fanny.ficuciello@unina.it, c=IT
Date: 2024.03.16 20:05:44 +01'00'

Prof. Fanny Ficuciello, Advisor

Università degli Studi di Napoli Federico II
Ph.D. Program in Information Technology and Electrical Engineering
XXXV cycle - Chairman: Prof. Stefano Russo

itee PhD
enformation technology
electrical engineering

http://itee.dieti.unina.it

Candidate's declaration

I hereby declare that this thesis submitted to obtain the academic degree of Philosophiæ Doctor (Ph.D.) in Information Technology and Electrical Engineering is my own unaided work, that I have not used other than the sources indicated, and that all direct and indirect sources are acknowledged as references.
Parts of this dissertation have been published in international journals and/or conference articles (see list of the author's publications at the end of the thesis).

Napoli, March 11, 2024

Cristina Iacono

Cristina Iacono

The field of surgical procedures has undergone a significant transformation in the last three decades with the introduction of robotic surgery. In operating rooms, robotic devices are now integrated into the planning and execution of surgical treatments with advantages over traditional laparoscopy, such as enhanced dexterity, improved ergonomics, motion scaling, and effective tremor filtering. Over the past decade, robotic systems, particularly the da Vinci robotic system from Intuitive Surgical Inc. in Sunnyvale, CA, have played a pivotal role in minimally invasive robot-assisted procedures. Despite these advancements, surgical robotics still has limitations: surgical procedures success robustly depends on the surgeon's ability and the minimal access to the surgeon field brings a heavy mental workload to surgeons. At the same time, the surgical environment is strongly unstructured and prone to complications. For this reason, there is the need for advanced assistive control features capable of augmenting surgeon's skills and facilitating autonomous execution of surgical tasks to ensure consistently high-quality intervention. As surgical robotics moves towards increased autonomy, vision-based techniques, haptics and data-driven algorithms constitute key concepts in robotic scenarios. This thesis aims to address the limitations of surgical robotics by contributing to different levels of autonomy of surgical robotic procedures. Each chapter of the thesis examines part of the research work conducted during the Ph.D. and concerns one or more of the many fields that contribute to robotics automation.

Keywords: Surgical Robotics; Shared Control; Automation in surgery; Vision-based Control

Sintesi in lingua italiana

Il campo delle procedure chirurgiche ha subito una trasformazione significativa negli ultimi tre decenni con l'introduzione della chirurgia robotica. Nelle sale operatorie, i dispositivi robotici sono ora integrati nella pianficatione e nell'esecuzione dei trattamenti chirurgici con vari vantaggi rispetto alla laparoscopia tradizionale, come una maggiore destrezza, una migliore ergonomia, lo scalamento del moto e un il filtraggio del tremore. Negli ultimi dieci anni, i sistemi robotici, in particolare il sistema robotico da Vinci di Intuitive Surgical Inc. a Sunnyvale, CA, hanno svolto un ruolo fondamentale nelle procedure robotizzate mini-invasive. Nonostante questi progressi, la robotica chirurgica ha ancora dei limiti: il successo delle procedure chirurgiche dipende fortemente dalla capacità del chirurgo e l'accesso minimo al sito chirurgico comporta un pesante carico di lavoro mentale ai chirurghi. Allo stesso tempo, l'ambiente chirurgico è fortemente destrutturato e soggetto a complicazioni. Per questo motivo, vi è la necessità di funzioni avanzate di controllo assistivo in grado di aumentare le competenze del chirurgo e facilitare l'esecuzione autonoma delle attività chirurgiche per garantire costanza nella qualità degli interventi. Mentre la robotica chirurgica avanza verso una maggiore autonomia, le tecniche basate sulla visione, sensibilità aptica e gli algoritmi basati sui dati costituiscono concetti chiave negli scenari robotici. Questa tesi si propone di affrontare i limiti della robotica chirurgica contribuendo a diversi livelli di autonomia delle procedure robotiche chirurgiche. Ogni capitolo della tesi esamina parte del lavoro di ricerca condotto durante il Ph.D. e riguarda uno o più dei molti campi che contribuiscono all'automazione robotica.

Parole chiave: Robotica Chirurgica; Controllo condiviso; Automazione nella chirurgia; Controllo basato sulla Visione.

Contents

Acknowledgements

The research presented in this dissertation has been partially supported by the Research Project "PROSCAN "strumenti micro-meccanici e robotici per la diagnosi e la terapia del tumore alla prostata". I would like to express my sincere thanks to the ICAROS Lab and PRISMA Lab for providing me with state-of-the-art facilities and an intellectually stimulating environment.

A special note of appreciation goes to my tutor, Prof. Fanny Ficuciello, whose guidance, patience, and expertise have been instrumental in the shaping of this research. I would also like to thank Prof. Bruno Siciliano for always inspiring me from the moment I decided to start the university in Automation Engineering until now.

The time I spent at the Worcester Polytechnic Institute under the supervision of Prof. Fisher was an extraordinary phase of my learning journey. I am profoundly grateful for the opportunity to work in an international setting, which broadened my perspective and exposed me to new methodologies and cultures.

Finally, I would like to acknowledge the countless researchers, colleagues, and peers whose direct and indirect contributions have enriched this journey.

List of Acronyms

The following acronyms are used throughout the thesis.

AI	Artificial Intelligence
ALPSO	Augmented Lagrangian Particle Swarm Algorithm
CNN	Convolutional Neural Network
DH	Denavit-Hartemberg
DOF	Degree of Freedom
dVSS	da Vinci® Surgical System
dVRK	da Vinci® Research Kit
ECM	Endoscope Camera Manipulator
EKF	Extended Kalman Filter
EMG	Electromyography
FDA	Food and Drug Administration
FLANN	Fast Library for Approximate Nearest Neighbors
FPGA	Field Programmable Gate Array

FRVF	Forbidden Region Virtual Fixture
GVF	Guidance Virtual Fixture
IEC	International Electrotechnical Commission
ICAROS	Interdepartmental Center for Advances in Robotic Surgery
ICG	Indocyanine Green
IMU	Inertial Measurement Unit
IoU	Intersection over Union
ISO	International Organization for Standardization
ISO/IEC	International Organization for Standardization (ISO) and International Electrotechnical Commission (IEC)
JIGSAWS	JHU-ISI Gesture and Skill Assessment Working Set
LC	Laparoscopic Cholecystectomy
LMI	Linear Matrix Inequality
LS	Laparoscopic Surgery
LoA	Level of Autonomy
MATA	Prisma Dataset
MIS	Minimally Invasive Surgery
MIRS	Minimally Invasive Robotic Surgery
ML	Machine Learning
MTM	Master Tool Manipulator

MVC	Maximum Voluntary Contraction
OS	Open Surgery
PSM	Patient Side Manipulator
PSO	Particle Swarm Optimization
QLA	Quad Linear Amplifier
RALP	Robot-Assisted Laparoscopic Prostatectomy
RAS	Robot-Assisted Surgery
RCM	Remote Center of Motion
R-CNN	Recurrent Convolutional Neural Network
RF	Random Forest
RMSE	Root Mean Square Error
ROS	Robot Operating System
SAW	Surgical Assistant Workstation
SUJ	Setup Joints
SIFT	Scale-Invariant Feature Transform
VF	Virtual Fixture
YOLO	You Only Look Once

List of Figures

List of Tables

Chapter 1

Introduction

1.1 Minimally Invasive Surgery

The closing decades of the 20th century witnessed a profound transformation in the field of surgical procedures, marking the beginning of a technological revolution that continues to redesign the practice of medicine, with a particular focus on reducing invasiveness. This transformative era has seen the widespread adoption of minimally invasive interventional treatments across various medical disciplines. Evidences supporting the benefits of these less invasive procedures, such as diminished complications, lower mortality and morbidity risks and quicker return to normal activities, have caused a global reevaluation of conventional surgical and radiological practices. This focus on less or minimal invasiveness has, therefore, become the subject of intense research in recent years. Minimally Invasive Surgery (MIS) approaches have been applied to various surgical specialties, including general surgery, urology, thoracic surgery, plastic surgery, and cardiac surgery and dentistry. In all these applications, the pain, discomfort, disability, or other complications consequential to surgery are often due to the trauma caused by gaining access to the surgical area of interest rather than from the procedure itself [1].

As previously mentioned, MIS refers to all surgical procedures that require reducing the size of the incision in the patient's body. Thoracic surgery, traditionally associated with significant morbidity and prolonged recovery periods, has witnessed a great impact with the introduction of minimally invasive approaches. Plastic surgery, primarily known for its focus on aesthetics, has incorporated MIS to enhance precision and minimize scarring in various cosmetic and reconstructive procedures. Minimally invasive dentistry aims to achieve the treatment objective by using a surgical process that eliminates the minimum amount of healthy tissue. With the help of an endoscope, a medical instrument equipped with an illuminating source, the operating surgeon can inspect and visualize the internal body cavities on a monitor and provide instructions for surgical maneuvers without any obstacles to observing. Endoscopically assisted surgery is gaining popularity and becoming a commonly used practice to simplify complicated procedures that require bigger access to visualize the interested area [2]. Magnifying the optical operating field is crucial in several surgical specialties, including general surgery, gynecological surgery, orthopedic surgery, neurosurgery, pediatric surgery, ophthalmology, otolaryngology, oral and maxillofacial surgery, plastic surgery and podiatric surgery. Microsurgery is the term used to describe the surgical techniques that require an operating microscope and the necessary specialized instrumentation. The advancements in technology and techniques have led to the ability to do anastomosis of successively smaller blood vessels and nerves [3].

General surgery stands at the forefront of this paradigm shift, as minimally invasive techniques have been successfully applied to procedures ranging from appendectomies to complex abdominal surgeries with laparoschopic approach. Laparoscopic Surgery (LS) is a minimally invasive surgical technique that uses a laparoscope, a thin, telescopic rod with a camera at the end, allowing the surgeon to access the inside of the body without making large incisions in the skin. Instead of the 6–12 inch cut necessary for Open Surgery (OS), LS uses two to four small incisions, called keyhole, of half an inch or less for the surgical instruments and the camera. During LS, the operation inside can be either identical to the OS approach, with the only difference being the method of access, either different, with the same aim and principle. An abundance of case studies, trials and meta-analyses have demonstrated the advantages of LS. Patients undergoing laparoscopic operations have less postoperative pain, less impairment of vital functions, shorter hospital stays, and they resume usual activities more rapidly. LS is most commonly used in gynecology, urology, and gastroenterology, comprehending procedures such as inguinal hernia repair, cholecystectomy, colorectal surgery, appendectomy, gastric, pancreas, and liver surgery. The first attempts at laparoscopically repairing inguinal hernias were made in the 1980s, and since then, significant advantages have been found in terms of pain relief. Studies show that there is no higher risk of severe intra-abdominal injuries, such as intestinal, blood vessels, or bladder injuries, compared to open surgery. The first laparoscopic removal of a gallbladder was made in 1985 and, since then, this procedure has undergone rapid development, making Laparoscopic Cholecystectomy (LC) the gold standard for the surgical treatment of gallbladder stone disease. Most studies on laparoscopic colorectal procedures have shown several benefits to patients. These include reduced pain, less damage to lung function, resulting in lower rates of pneumonia, and faster recovery of intestinal function. Patients find this technique particularly attractive due to the minimal access with four small incisions. Indeed, the conventional approach results in larger access trauma compared to the relatively small intra-abdominal surgical trauma, while in the laparoscopic approach, access trauma and intra-abdominal surgical trauma coincide. [4].

Although LS is considered the third patient-friendly medical revolution following the introduction of asepsis and anesthesia, it poses several challenges to surgeons. LS requires the use of different instruments and presents reduced tactile sensations. The operating field is displayed on a monitor, causing changes in the surgeon's posture. The surgeon must develop new strategies to compensate for the two-dimensionality and resulting loss of depth perception. The camera is not controlled directly by the surgeon but by an assistant. Additionally, the long and rigid instruments require considerable agility. In conventional surgery, there are seven Degree of Freedoms (DOFs), whereas LS provides only four. This loss of freedom increases the difficulty of suturing and tying knots. Nevertheless, critical voices claim technical difficulties in LS, especially in mastering video-eye-hand coordination, physical and mental workload. Given these, it is not surprising that LS has a substantial learning curve and thus an associated longer training for surgeons. Another argument against LS is the higher cost due to longer operating times and the need for new instruments, which are sometimes only used once. As with all areas of medicine, the issue of the expense of LSs is increasingly important, especially when it is compared with traditional, open operations. However, even though the direct cost per operation is higher, the indirect cost to society decreases by allowing patients to return to work more quickly.

1.2 Minimally Invasive Robotic Surgery

Market and research offer various surgical robotic platforms. These robots come equipped with advanced technology such as high-frequency ultrasound, microscopes, drills, and endoscopes that have significantly improved patient outcomes. Many medical and surgical practices that wouldn't be possible without robotic technology have been made achievable. Surgical robots have been successfully incorporated in several MIS domains. For example, surgical robots have been used in orthopedic surgery for precise bone cutting and in other areas where rigid anatomical parts are mostly present in the surgical environment. Additionally, surgical robots, accompanied by image-based preoperative plans without human interruption except in emergency situations, have found application in procedures like stereotactic radiosurgery and minimally-invasive neurosurgery.

Microsurgery is an area in which robotics can have a significant impact on patient benefits and public health. The precision required in microsurgery is extremely high, and the surgical workspace is small. Robots can deliver sub-millimeter tool motion scaling and physiological tremor attenuation, which are crucial to performing surgical tasks at the limits of human capabilities. However, the large footprint of some commercial robotic systems used in MIS makes them unsuitable for direct microsurgical use [5].

The shift from OS to LS has been a significant advancement in reducing scarring and hospitalization time for patients. However, it can sometimes limit the surgeon's dexterity, ergonomics, sensory feedback, and visualization compared to OS. The development of surgical robotic systems has addressed these limitations and improved the overall surgical experience. The limitation of standard laparoscopic instruments to only 4 DOFs is a considerable disadvantage to surgeons' dexterity, particularly for beginners. Though this limitation has minor implications during ablative surgery, such as organ dissection, vessel clipping, coagulation, and anatomical structure division, it considerably reduces dexterity during reconstructive surgery, shortening the learning curve. Moreover, surgical robotic platforms can significantly improve surgeons' ergonomics with respect to laparoscopy. A study published in 2015 compares the ergonomics of standard laparoscopy with laparoscopy using an ergonomic commercial chair or using the popular surgical platform da Vinci® Surgical System (dVSS). It shows significantly lower muscle pain (including neck pain, shoulder pain, wrist pain, and back pain) for surgeons who use the dVSS, with respect to the alternatives [6], [7]. Surgical robots have also gained widespread acceptance due to the significantly improved accuracy and precision of surgical techniques. Robot-Assisted Surgery (RAS) offers 3D visualization and limits the fulcrum effect, which amplifies tremors in LS. Furthermore, the learning curve for robotic surgery is considerably shorter, and surgeons without prior laparoscopic experience can successfully transfer their surgical skills from open surgery to robot-assisted laparoscopic surgery.

Throughout history, technology has played a crucial role in advancing medical procedures. From the introduction of laparoscopy in 1910 to the development of RAS in 1983 and the world's first in vivo miniaturized robotic surgery in 2016, the use of surgical robotic platforms for MIS has made significant progress. With advancements in the field, there has been a shift from OS to MIS such as LS, and robotic laparoscopic systems have been developed. As technology becomes cheaper, smaller, and faster, these systems continue to reduce in size and become more procedure-specific [8]. Urology and gynecology were the first medical specialties to adopt robotics in surgery and, since then, many other specialties have also started utilizing this technology. RAS has dramatically improved the safety and performance of intracorporeal suturing, which is crucial in urological and gynecological procedures. It is now becoming increasingly common for robots to be used in radical prostatectomies. Studies have shown that the Robot-Assisted Laparoscopic Prostatectomy (RALP) is superior to open and laparoscopic radical prostatectomy in various aspects since it has lower estimated blood loss and shorter hospital stays. It results in lower rates of readmissions, nerve injury, reoperations, deep vein thrombosis, and sepsis, as well as better continence rates and return of sexual function. Five years after its initial approval for use in urology, RAS has been adopted for radical hysterectomy for endometrial and cervical cancer. Since then, the robot-assisted procedure has been widely adopted, resulting in a significantly better postoperative quality of life index [9].

There are different surgical robotic platforms commonly used to substitute laparoscopic instruments in many clinical procedures for Minimally Invasive Robotic Surgery (MIRS). The dVSS, which was developed by Intuitive Surgical® Inc., Sunnyvale, CA, was the first surgical robotics system to receive clearance by the US Food and Drug Administration (FDA) in the year 2000, and it is now the most used robotic surgery system in the world. It is commonly used for general LS surgeries and has become one of the most frequently used robotic surgical systems. Over the years, the FDA has also approved the dVSS for thoracoscopic, urological, and gynecological surgeries, as well as an adjunct to some cardiac procedures [10]. Surgeons have used the dVSS in more than 10 million minimally invasive procedures through 2001, and there are more than 6700 dVSS installed in hospitals in 69 countries worldwide [11]. The widespread use of dVSS is possible due to the advanced wristed instrumentation (EndoWrist®) that allows 7 DOFs, tremor filtration, a high-resolution three-dimensional visualization system, and a comfortable user console [12]. The dVSS is a teleoperated robot composed of a surgical console, a patient-side cart and a vision cart. The surgical console is located outside the sterile site and is controlled by the surgeon through two master controllers and pedals. During a surgical procedure, a 3D endoscope captures a visual of the surgical site. This visual is then processed by the vision cart and transmitted to the surgeon through a stereo visor. Ultimately, the patient-side is the system's operative part, consisting of four arms holding instruments and an endoscope. The instrumentation, inspired by the human hand, improves surgical precision and comprises graspers, needle drivers, clip appliers, and energy instruments. The da Vinci®platforms on the market are: (i) da Vinci®Xi that is the most advanced platform from Intuitive Surgical®, shown in Figure 1.1; (ii) da Vinci®X which has the same arm architecture of da Vinci®Xi with modular components; (iii) da Vinci®SP that is a surgical platform designed for single-port access with a single-arm delivering three multijointed instruments.

Despite their benefits, surgical robotics have some limitations. During surgical procedures, the visibility of the surgical site is often limited, and the tools used must work very closely with each other. Additionally, expert surgeons must develop skills to compensate for the lack of haptic feedback,

Figure 1.1. Da Vinci Xi® Surgical System.

relying on visual perception instead. All of this while performing kinematically complex and repetitive tasks, whose success is strongly dependent on the surgeon's ability. In summary, surgical robotics still lacks advanced assistive control features that could notably support a surgeon's activity and perform surgical tasks with autonomy for a high-quality intervention. Despite their potential, surgical robotics still lacks advanced assistive control features that could significantly support a surgeon's activity and perform surgical tasks with autonomy for a high-quality intervention. Many surgical procedures could benefit from the application of advanced control techniques, allowing the surgeon to work under less stressful conditions and perform the surgical procedures with more accuracy and safety.

1.3 Thesis Overview

The thesis contributes to the field of automation in robot-assisted surgical procedures by addressing critical aspects essential for the advancement of surgical robotics:

Vision Perception: Perception is essential in a robotic system. In particular, in surgical robotics, vision perception plays a key role as it is the only feedback to the surgeon in the absence of force feedback to characterize the surgical site. The thesis explores state-of-the-art methodologies and frameworks for enhancing vision perception. In this thesis there is a significant contribution to this topic through the development of vision-based control frameworks that not only augment the perceptual capabilities of surgical robots but also lay the groundwork for more accurate and context-aware surgical interventions

Modeling: It is crucial to identify the kinematic and dynamic properties of robotic arms to effectively control the robot in an unstructured environment such as a surgical site and estimate external forces. This thesis work contributes to the field thanks to an accurate characterization of the dynamic model of the da Vinci® Research Kit (dVRK) surgical robotic systems.

Force Feedback: Most of the currently available robotic surgery systems do not have haptic feedback capability. In addressing this deficiency, the thesis contributes to demonstrating the capacity of force feedback to reduce unintentional damages and accelerate the learning curve for novice surgeons. Additionally, the thesis explores the broader implications of force feedback, providing a comprehensive framework for implementing advanced control algorithms, including impedance control and virtual fixtures.

Data Collection: Data collection plays a crucial role in the fields of Artificial Intelligence and robotics. It is essential for training robots to navigate, interact with the environment, and perform complex tasks, operating with greater autonomy and precision. The open access design of the dVRK incentivizes and enables researchers to easily access and collect data. For these reasons, an important part of the thesis contributes to the creation of a dataset based on the suturing task with dVRK that will be used for further research.

1.4 Thesis Structure

The rest of the thesis is structured as follows:

Chapter 2 explores the concept of autonomy in surgical robotics and examines the literature that serves as a foundation of the research contribution.

Chapter 3 presents a method to identify the complete dynamical model of the PSM arm of the dVRK robot. The more precise dynamic model of the dVRK was needed to be able to actuate model-based control techniques such as impedance control. The proposed model is tested using a residual-based approach for external force estimation acting on the PSM end-effector.

Chapter 4 introduces the use of force feedback to improve performances in robot-assisted surgical procedures. In particular, a control framework has been developed that includes impedance control and Forbidden Region Virtual Fixture (FRVF) to avoid the collision between the surgical instruments starting from the endoscopic images. It is demonstrated through a user study how the use of force feedback facilitates the use of the surgical robot for inexperienced surgeons.

Chapter 5 explains the development of a control framework for human-robot interaction in medical applications that are characterized by an RCM constraint. The method proposes a control strategy that ensures both the RCM kinematic constraint and repulsive VFs constraint in a human-robot interaction framework, in which the doctor guides the manipulator throughout the surgical application.

Chapter 6 presents a deep learning-based method for the localization and segmentation of the biliary tract to help the surgeon better visualize the biliary tract without using Indocyanine Green (ICG). A database of laparoscopic images has been constructed and annotated to train the deep learning algorithm.

Chapter 7 proposes a novel dataset from several surgeons with different skill levels, who performed the suturing task on the dVRK.

The dataset includes kinematics, video, interaction force, electromyographic signal and acceleration, angles, and angular velocity of the surgeon's right wrist. The data has been organized by surgical gestures part of the suture procedure.

Chapter 2

State-of-art in Robotic Surgery

The thesis aimed to propose new control strategies and computer vision algorithms that allow different levels of robot autonomy to reduce the surgeon's workload and improve the quality of surgical procedures. This chapter presents the concept of autonomy in the context of surgical robotics. The definition is provided in Section 2.1, accompanied by a systematic taxonomy designed to classify surgical robots. Subsequently, an overview of the related works in robotic surgery, starting from Level 0 and moving toward Level 5, is presented in Section 2.2. In Section 2.3, the robotic hardware and software used to test the advanced control method developed in this thesis are discussed. This section provides an overview of the dVRK setup, its kinematic model, and a general formulation of the dynamic model. The models serve as a foundation for the subsequent chapters, particularly Chapter 3, where detailed analysis and implementation of the dynamic model will be discussed.

2.1 Autonomy

Traditionally, autonomy is considered a fundamental component of robots. Figure 2.1 shows examples of commercially available systems for different clinical applications. In [13], the authors present a classification of telerobots based on control architecture and user interaction. Three categories are defined depending on the degree of user interaction: direct or manual control, shared control and supervisory control robotic systems. In direct control, the surgeon operates the slave robot directly through the master console, leaving no autonomy to the slave robot. Apparently, this mode has the most surgeon involvement. At the other end, in supervisory control, the procedure is executed by the robot, while the surgeon (supervisor) gives high-level directives. Finally, in shared control, the surgeon and the controller share the manipulator's command and work together to carry out a task. Obviously, shared control combines the intelligence of the surgeon and the robot thus, the robot presents limited autonomy.

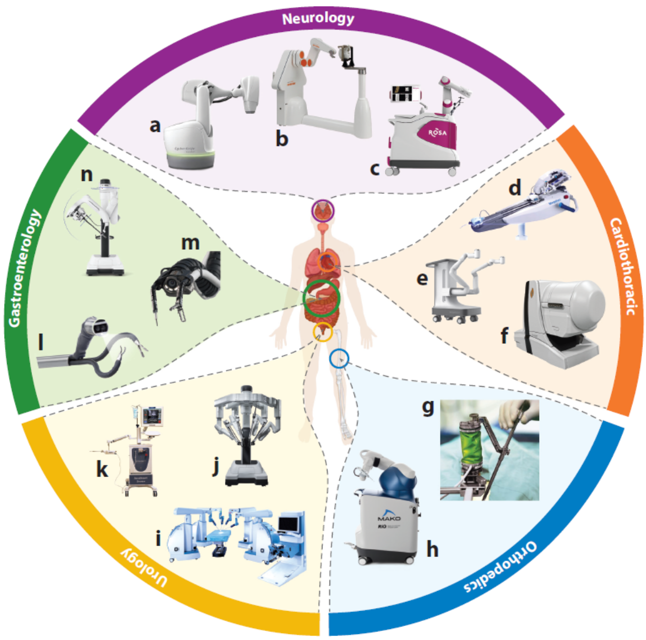

Figure 2.1. Commercially available systems organized by clinical application [14]: (a) CyberKnife M6, Accuray; (b) Neuromate, Renishaw; (c) ROSA ONE, Zimmer Biomet; (d) Magellan, Hansen Medical; (e) Monarch, Auris Health; (f) Niobe, Stereotaxis; (g) Renaissance, Mazor Robotics; (h) Mako, Stryker; (i) Senhance, TransEnterix; (j) da Vinci Xi, Intuitive Surgical; (k) AquaBeam, PROCEPT BioRobotics; (l) SPORT, Titan Medical; (m) Flex Robotic System, Medrobotics; (n) da Vinci SP, Intuitive Surgical.

The most common type of surgical robot is the master–slave telesurgery device, commonly used for MIRS. In an effort to standardize the autonomous capabilities of surgical robots, the International Organization for Standardization (ISO) and International Electrotechnical Commission (IEC) (ISO/IEC) defined Level of Autonomy (LoA) based on the human versus robotic functions of the system. In [15], the authors present a 6-stage classification scale for surgical robots:

- **LoA 0 — No autonomy**: the human surgeon is in charge of all actions. Teleoperated robots or prosthetic devices with motion scaling are included because the output represents the surgeon's desired motion.

- **LoA 1 — Robot Assistance**: the human surgeon directly and continuously controls the robotic system while the surgical robot performs teleoperation and low-level functions like tremor filtering and minor safety features, mechanical guidance or assistance.

- **LoA 2 — Task-level autonomy**: the surgeon maintains a discrete, rather than continuous, control of the system, while the system is trusted to execute specific tasks and sub-tasks for a short time.

- **LoA 3 — Conditional autonomy**: the human surgeon is involved with high situation awareness while the robotic system can conduct large sections of the surgical procedure and make low-level decisions.

- **LoA 4 — High-level autonomy**: the human surgeon only approves and has the ability to emergency stop the procedure, while the robotic system executes complete procedures.

- **LoA 5 — Full autonomy**: the robot can complete the treatment planning and execution without a human fallback option.

The following section will present each level of autonomy along with its enabling technologies and applications. An overview of related works that contributed to the research presented in this thesis will be provided.

2.2 Control in robotic surgery

2.2.1 Level 0

There is a vast amount of literature available on level 0 systems. The dVSS introduced the paradigm of transparent teleoperation. In this system, the surgical instruments on the patient's side replicate the movements performed by the surgeon on the control interface. However, the system also includes some algorithmic autonomy, such as tremor suppression and redundancy resolution. These features do not interfere with the surgeon's actions. The bulk of commercially available platforms for robotic surgery belong to level 0.

2.2.2 Level 1

Level 1 autonomy aims to support the surgeon in executing the surgical procedure without ever taking control of the action. In the surgical context, enabling technologies necessary to achieve level 1 can be identified in tool tracking, eye tracking, and tissue interaction sensing.

Surgical tool tracking is a core component for developing assistive technologies, such as augmented reality and haptic feedback. In the literature, most tracking methods used to correct the surgical tool position error are realized using the robotic system's sensors or external sensors integration, but still obtaining limited accuracy. A significant improvement is introduced by image-based approaches, detecting the tool's position and orientation in the camera reference frame. In [16], the authors presented a survey about vision-based and markerless surgical tool tracking. The works can be classified based on the segmentation and tracking methods [17], most of them exploiting Random Forest (RF) or Convolutional Neural Network (CNN) techniques. In [18], the authors combine a region-based segmentation technique with point-based pose estimation, using prior knowledge of the instrument shape through classification with a RF, besides temporal motion is incorporated with a Kalman filter. Du et al. [19] proposed a 2D tracker based on a Generalized Hough Transform using Scale-Invariant Feature Transform (SIFT) features, which can both handle complex environmental changes and recover from tracking failure. They extended the work in [20], presenting a 2D pose estimation framework for articulated endoscopic surgical instruments, which involves a fully convolutional detection-regression network (FCN) and a multi-instrument parsing component. Chapter 4 proposes an Extended Kalman Filter (EKF) for tool tracking without the use of markers coupling vision and kinematics information.

Tissue interaction sensing is an important technology for level 1 robot autonomy. Monitoring the force between a tool and tissue helps prevent damage and improves surgical skills training. In surgery, tactile information is traditionally used for diagnosis, making haptic perception crucial. Moreover, without haptic feedback, surgeons performing RAS may damage healthy tissues due to poor force regulation. Force sensors can measure instrument tip forces, but their size, cost, and environmental requirements in MIRS limit their use in operating rooms. In the literature [21, 22], the external wrench is estimated by combining the dVRK dynamic model with motor currents. However, this approach may be prone to noise in the measured data, potentially compromising accurate force detection. In this thesis, specifically in Chapter 3, 4 and 7, a sensorless force estimation method has been used. The method directly uses dynamic parameters and thus needs an accurate dynamic model of the robot to be employed, further analyzed in Section 2.3 and Chapter 3.

As previously mentioned, level 1 autonomy systems aim to assist the surgeon during the surgical procedure. Such systems comprise Passive Assistance technologies that provide the surgeon with additional information, including assisted planning before the surgery and augmented reality during the procedure; and Active Assistance systems, which perform actions that affect the surgical procedure, such as applying forces to the user interface or restricting the motion of surgical instruments based on force sensors, precomputed forbidden areas, etc.

In the interest of safety and due to the unique conditions of the surgical environment, there are various situations that may require restriction of the motion of the robot. For instance, it may be necessary to apply a RCM constraint to robots that don't mechanically provide it to use them in surgical applications.

During OS, surgeons heavily rely on tactile and force feedback. However, MIS severely hampers such feedback and is completely lost in current MIRS. Shared control techniques based on VF can be an effective way to implement active assistance systems, rendering haptic cues to the surgeon. There are two types of VFs: Forbidden Region Virtual Fixtures (FRVFs) and Guidance Virtual Fixtures (GVFs). FRVFs are used to simulate barriers around forbidden regions, while GVFs attract the robot end-effector towards the desired path. VFs are commonly used in teleoperated robots to allow haptic feedback or guidance and, therefore, actively assist the user through force rendering at the master side.

Rosenberg was the first author to introduce VF [23]. Since its introduction, shared control techniques have had great success in surgical applications and for collision and obstacle avoidance. An extensive review of VF literature can be found in [24]. Moreover, VFs have found application in major branches of robotic surgery research, providing haptic information to the users [25]. Recently, many authors have considered VFs use in shared control teleoperation, and multiple works were presented to introduce active constraints in surgical robotics for task and safety accomplishments. Selvaggio *et al.* propose online VFs generation and adaptation guiding the surgeon during procedures [26]. A large number of works used VFs implementations to solve a specific sub-task. Chen *et al.* presented active constraints to assist in knot tying in robotic laparoscopy [27]. Moccia *et al.* proposes a vision-based method for robot-aided polyp dissection where the VF is adapted to the change in the polyp's shape and the guidance constraint is enforced through an impedance control [28]. Li *et al.* presented an online collision avoidance method for real-time interactive control of a surgical robot in geometrically complex environments, such as the sinus cavities [29]. Ren et al. [30] proposed dynamic active constraints using medical images. The system builds potential fields to reduce the contact force between the tooltips. Xia et al. [31] reduced the proportional gain in an admittance control law according to the distance between the tool tip and the nearest obstacle. This allowed the system to avoid collisions smoothly. Rydén *et al.* showed a method to create FRVF to protect an object from undesired contacts, using point cloud streamed by an RGB-D camera [32]. This method uses depth information and is generally applicable only for collision avoidance on the tooltips. Wide literature is available on dynamic VFs, especially dealing with collision avoidance between the tooltip and the beating heart [33–35]. In [36] and [37] Marinho *et al.* propose a vector-field inequalities method to provide dynamic active-constraint for collision avoidance of any number of robots and moving objects sharing the same workspace. Further research work about dynamic active constraints to prevent tools' collision has been proposed by Banach *et al.* in [38]. The authors proposed FRVF strategy to avoid surgical tool clashing and, simultaneously, the collision with patient anatomy using the elastoplastic frictional force control model. Chapters 5 and 4 contribute to the topic of applying FRVF in different surgical scenarios.

Many different kinds of mechanically constrained RCM manipulators have been proposed in the literature ([39, 40] and [41]) since it is generally considered a safer solution respect to imposing the RCM vis software control [40]. Nevertheless, the second paradighm constitute a more flexible solution to the problem, also allowing the use of the same manipulator both for OS and for MIRS. Different approaches have been adopted to derive a formalization of the RCM as a kinematic constraint and to actively enforce it. In particular, Ortmaier et al. [42] proposed an inverse kinematic control to enforce the motion constraint preventing any force from being exerted on the trocar during robotic surgery. However, the adoption of position control in a surgical operation can result in high contact forces in case of rigid interaction. For this reason, From et al. [43], while addressing the RCM constraint in task space, introduced Cartesian impedance control to perform the tasks safely. A step further in enforcing the RCM constraint was performed in [44], where it is proposed an improved dynamic control approach that takes advantage of task redundancy for the RCM constraint. Similarly, in [45] an adaptive decoupling controller exploiting task redundancy was also proposed. In [46] a formalization of the constraint which explicitly models the translation motion along the link axis is presented. This is the distinguishing feature with respect to [47].

2.2.3 Level 2

In order to achieve level 2 task autonomy, a robot must be able to free surgeons from the physical and cognitive burdens associated with complex and repetitive tasks such as tissue retraction, suturing, and ablation. A significant amount of literature is available on the automation of suture tasks, which can significantly reduce the cognitive burden on surgeons. Autonomous suturing task is generally divided into two stages: inserting the needle and tying a knot with a surgical thread. Gesture classification can enhance the robot's ability to activate at the right time and minimize disruption to the surgical workflow. It also enables the robot to follow the clinician's work plan, thus providing dedicated support depending on the phase of the operation [48]. A crucial aspect of these data-driven algorithms is the collection of large datasets, specifically those that record the execution of surgical procedures by robotic systems, including the kinematics, dynamics, and video information recording the movements of the surgeon. Chapter 7 presents an overview of a dataset collected during the execution of the surgical suture with the dVRK.

Another investigated application at this level of autonomy is stiffness mapping: the ability to autonomously estimate the tissue properties by mechanical contact, which would substitute manual palpation for identifying and dissecting malignant masses. Haptics technology aims to restore this ability.

2.2.4 Level 3

Level 3 conditional autonomy comprises systems capable of independently extracting the necessary parameters required to plan a specific task from the information available. This level of autonomy is enabled by enabling technologies such as tissue modeling, high-level feature tracking, and advanced imaging. These technologies can be applied in advanced suturing procedures, where real-time imaging is used to extract the length of each suture and suturing points automatically. Additionally, they can be utilized for the autonomous navigation of flexible endoscopic robots in unstructured environments and for autonomous anastomosis.

2.2.5 Level 4

Level 4 systems have the capability to make and execute clinical decisions automatically while still being monitored by a surgeon. These systems rely on enabling technologies, such as organs and tumor segmentation in preoperative images (MRI, CT, and ultrasound), which find applications in procedures like debridement and tumor resection. In order to successfully perform tumor resection, robotic systems must integrate preoperative and intraoperative imaging modalities (white-light endoscopy, fluoroscopy, or near-infrared fluorescence) [14]. In recent years, many advancements have been made in object detection, and the results have also been proven in the medical domain, both in pre-operative and intraoperative imaging [49–51]. The work [52] applies CNN to video for localizing objects in real-time. With respect to other imaging algorithms, acyolo is very fast and thus appealing for real-time applications. Many works in literature use acyolo to detect and localize anatomical structures lesions, tumors, and other clinically relevant medical objects. In [53], the authors used acyolo to detect anomalies like esophagitis and polyps during endoscopy. Authors in [54] propose a modification of the algorithm that combines acyolo with a Resnet CNN model for disease classification and detection during capsule endoscopy. A comprehensive review of the application of You Only Look Once (YOLO) in the medical domain can be found in [55].

2.3 da Vinci Research Kit

Figure 2.2. Da Vinci Research Kit at Interdepartmental Center for Advances in Robotic Surgery (ICAROS) center.

Initially, the scope of engineering research on the dVSS was limited to utilizing the system's data. To address this limitation and enable research on advanced control techniques, the dVRK was introduced. The dVRK research platform is based on the dVSS, developed and distributed by Intuitive Surgical Inc®. It comprises a set of first-generation da Vinci components that can be utilized to construct a telerobotics platform.

The full platform includes the surgeon's console and the patient-side console. The surgeon's console presents a stereo viewer that shows the surgical scene thanks to an Endoscope Camera Manipulator (ECM) with 4 DOFs at the patient's side. Furthermore, the surge on's console includes two Master Tool Manipulators (MTMs), each with eight DOFs, enabling natural and dexterous hand manipulation and a foot-pedal tray. On the patient's side, the two PSMs and an ECM are controlled by the MTMs with coordinated foot-pedal movements. In this setup, the dVRK slave manipulators (PSMs) are integrated into a Setup Joints (SUJ), an articulated structure comprising non-actuated arms, as shown in Figure 2.3. The feature of the SUJ is that control over the joints is achieved by employing brakes, allowing precise control over the robot's movements. Additionally, the angular position of the joints can be accurately determined by utilizing potentiometers.

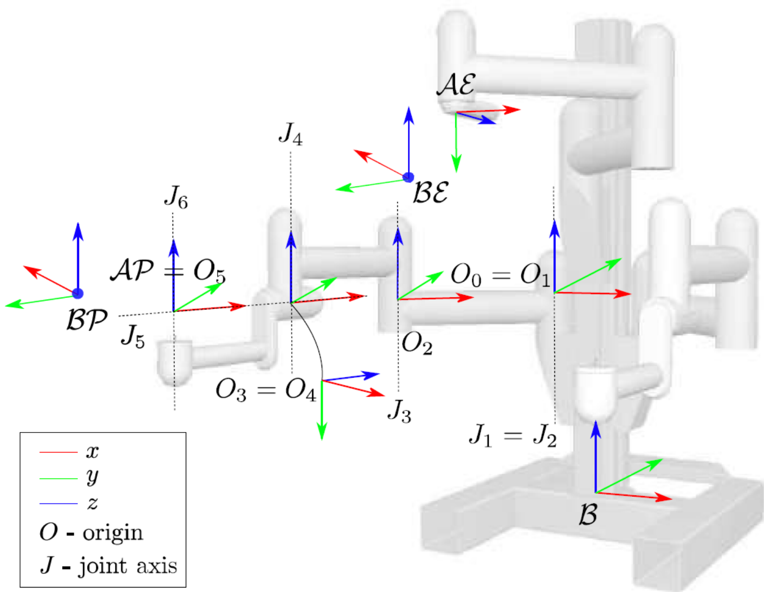

Figure 2.3. SUJ arm kinematics.

The interface between the two consoles is based on custom hardware consisting of motor controllers, coupled with Field Programmable Gate Arrays (FPGAs) and connected to a PC running the control loops [56] and provides full access to all levels of control through open-source electronics and software. In Figure 2.2, the dVRK, present at Interdepartmental Center for Advances in Robotic Surgery (ICAROS) of the University of Naples Federico II, is shown. The open controller developed by the Johns Hopkins University LCSR and Worcester Polytechnic Institute (WPI) AIM Lab [57] permits complete control of the dVRK robotic arms with Robot Operating System (ROS) framework. The controller allows position, velocity and current control, allowing for advanced techniques such as impedance control, force control, and bilateral tele-manipulation control to be developed and tested. Each manipulator arm is powered by one controller box with two sets of custom electronics boards, where each set consists of an IEEE-1394 (FireWire) FPGA control board and a Quad Linear Amplifier (QLA). All control boxes are daisy chained on an IEEE-1394 bus and connected to a Linux control computer. The FPGA board m rely gathers sensor data, transmits them to the control PC, receives motor torque commands from the PC and latches them to the hardware. All computation, including servo-level control, occurs on the control PC. The component-based software system is based on the open-source cisst/Surgical Assistant Workstation (SAW) package. It includes components for low-level I/O, servo-level control, cartesian mid-level control and teleoperation [58].

In general, the software can be arranged into the following functional layers: (a) hardware interface (I/O), (b) low-level control (e.g., PID), (c) high-level control, (d) teleoperation, (e) application. The low-level control layer consists of a PID joint controller for each manipulator, which is a general-purpose SAW component configured via an XML file. The high-level control is provided by two components that are specific for the da Vinci MTM and PSM. These provide the forward and inverse kinematics, trajectory generation, and gripper control. The teleoperation layer is provided by two instances of a general-purpose SAW component, each of them connecting one MTM to one PSM. Finally, the application layer is provided by a console application that emulates the master console environment of a da Vinci system. Each layer also includes an optional Qt Widget that can be used to visualize and interact with the corresponding SAW component.

2.3.1 dVRK Kinematic and Dynamic Models

The primary goal of the dVRK is to introduce a comprehensive and inclusive open control architecture. This innovative architecture acts as a versatile and dynamic platform, poised to facilitate cutting-edge research in the rapidly evolving context of surgical robotics. By embracing openness and collaboration, the dVRK not only facilitates researchers but also promotes a vibrant community of experts, engineers, and medical professionals who are dedicated to advancing the frontiers of surgical technology in enabling the development and testing of novel surgical procedures, enhancing the precision and safety of robotic-assisted surgeries, and ultimately improving patient outcomes [59–61].

The development of an accurate dynamic model is essential for the advancement of surgical robotics and the creation of innovative control strategies [62, 63], which can significantly assist surgeons by enabling autonomous or semi-autonomous execution of surgical tasks. A comprehensive understanding of the dynamic parameters of the robot manipulator is crucial to successfully utilize the dynamic model. Although data-driven techniques are gaining popularity in robotics research, a dynamic model of a robotic system remains essential for developing advanced control strategies. Dynamic models provide clear descriptions of a system's physics and mechanics, enabling control engineers to understand the system's behavior and create control algorithms based on fundamental principles. Model-based control techniques rely on dynamic models to optimize performance, stability, and safety. By accurately capturing the dynamics of the system, control algorithms can account for factors such as friction, inertia, and external pressures, minimizing potential dangers. Machine learning approaches can complement model-based control strategies and dynamic models, improving the theoretical foundation, interpretability, and robustness of robotic control for achieving precise and reliable control of robotic systems. Several research papers in the literature focused on identifying the dynamic model of the entire dVRK robotic system. For instance, Fontane li et al. proposed an extensive method for dynamic identification of the PSM and MTM arms, utilizing the recursive Newton-Euler approach, as presented in their work [64]. This approach assesses various factors such as mass/inertia, centrifugal, Coriolis, and gravity contributions to compute joint torques. However, the method still exhibits a 30% discrepancy between those calculated using the identified dynamic model and measured torques for most joints. In the paper by Sang et al. [21], they used least-square regression, screw theory, and Lagrange dynamics equations to describe the dynamics of the PSM. Similarly, Piqué et al. [22] expanded on Fontanelli's work [64] by adding driving inertia to the friction model contribution. In contrast, Fischer's research [65] stands out from other studies by providing a fully open-source solution for dynamic model identification. This work goes beyond the limitations of a single robotic platform and can be applied to a wide range of generic robotic systems to a wide range of generic robotic systems.

ECM arm kinematics

The ECM is a 4-DOF actuated arm, shown in Figure 2.4, which moves the endoscopic camera about the RCM through revolute and prismatic joints, combined in an RRPR sequence, where R and P correspond to revolute and prismatic joints respectively. The axis J_1, J_2 J_3 and $J4$ all intersect in one point, modeling the RCM mechanism.

PSM arm kinematics

Each PSM is a 7-DOFs actuated arm, which moves a surgical instrument about a RCM, a fixed fulcrum point that is invariant to the configuration of the PSM joints. The PSM 's DOFs are arranged in the sequential order of RRPRRRR. Axis J_2 is a double parallelogram mechanism, and axis J_3 is a prismatic joint that is used for insertion of the surgical instrument. During the translation of the J_3, a counterweight attached to link 2 moves in the negative direction of the movements. The counterweight moves at a third of the rate of J_3. Axes J_4, J_5, and J_6 form the non-spherical wrist of the PSM, allowing for additional degrees of freedom. Axis J_7 controls the motion of the gripper jaws. Figure 2.5 shows the PSM and a representation of the axes detailed above with the acdh frames.

PSM arm dynamics

To compute a symbolic dynamic model for the PSM arm, the Euler-Lagrange method [66] can be employed. The Lagrangian function, denoted

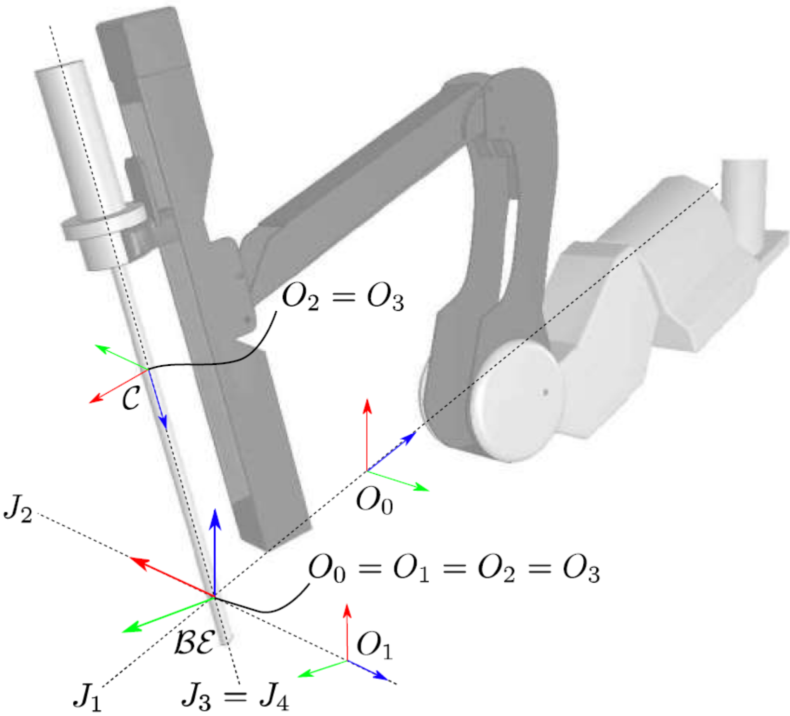

Figure 2.4. Schematic of the ECM kinematics with the DH frames.

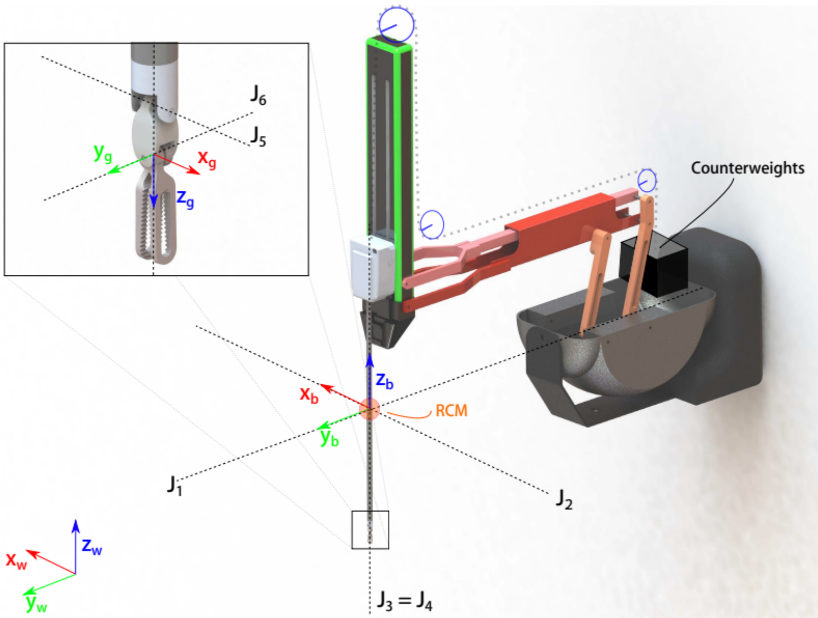

Figure 2.5. Schematic of the PSM kinematics with the DH frames.

as L, is defined as the difference between the kinetic energy (T) and potential energy (V) of the PSM. This approach considers the PSM manipulator as an n-DOFs manipulator. By utilizing the Eule -Lagrange equations:

$$\frac{d}{dt}\left(\frac{\partial L}{\partial \dot{q}_i}\right) - \frac{\partial L}{\partial q_i} = 0 \ , \tag{2.1}$$

the dynamic model of the system can be derived as follows:

$$\boldsymbol{\tau} = \boldsymbol{B}(\boldsymbol{q})\ddot{\boldsymbol{q}} + \boldsymbol{C}(\boldsymbol{q}, \dot{\boldsymbol{q}})\dot{\boldsymbol{q}} + \boldsymbol{G}(\boldsymbol{q}) + \boldsymbol{\tau}_f + \boldsymbol{\tau}_s \ . \tag{2.2}$$

In the given context, subscript i represent the joint numbers, the variables $\boldsymbol{q}$, $\dot{\boldsymbol{q}}$, $\ddot{\boldsymbol{q}}$, and $\boldsymbol{\tau}$, all belonging to the vector space $\mathbb{R}^n$, correspondingly denote the joint angles, velocities, accelerations, and torque vectors. The matrices $\boldsymbol{B}(\boldsymbol{q})$ and $\boldsymbol{C}(\boldsymbol{q}, \dot{\boldsymbol{q}})$, both belonging to the vector space $\mathbb{R}^{n \times n}$, denote the mass/inertia matrix and the matrix accounting for the centrifugal and Coriolis effects, respectively. Additionally, $\boldsymbol{G}(\boldsymbol{q})$, an element of $\mathbb{R}^n$, represents the vector associated with gravitational forces. The elements $\boldsymbol{\tau}_f$, $\boldsymbol{\tau}_s \in \mathbb{R}^n$ represent the joint friction and the stiffness torque vector respectively and provide additional torques to establish a comprehensive dynamic model.

In [67], the authors computed the dynamic model of the PSM arm using the recursive Newton-Euler approach, suitably modified to include the dynamic effects of the counterweight used to balance the motion of the instrument along the prismatic joint and the links of the double parallelogram mechanism. The dynamic model allows computing the joint torques $\boldsymbol{\tau}_{PSM} \in \mathbb{R}^n$, taking into account the inertia, Coriolis, centrifugal and gravity generalized forces. The contributions due to joint friction and elastic forces acting on some of the joints can be added separately:

$$\boldsymbol{\tau}_{PSM} = \boldsymbol{\tau} + \boldsymbol{\tau}_f + \boldsymbol{\tau}_s \ . \tag{2.3}$$

The torque $\boldsymbol{\tau}_f$ is the friction contribution and it was set to

$$\boldsymbol{\tau}_f = \boldsymbol{F}_v \dot{\boldsymbol{q}} + \boldsymbol{F}_s sgn(\dot{\boldsymbol{q}}) \ , \tag{2.4}$$

where $\boldsymbol{F}_s = diag\,\{F_{s1}, ..F_{s6}\}$ and $\boldsymbol{F}_v = diag\,\{F_{v1}, ..F_{v4}, \boldsymbol{F}_{vl}\}$ represent the static friction and viscous friction coefficients matrices both belonging to

the vector space $\mathbb{R}^{n\times n}$, and $\boldsymbol{F}_{vl} \in \mathbb{R}^{2\times 2}$ models the friction of the last two joints, that are coupled.
The elastic contribution $\boldsymbol{\tau}_s$ models the elastic forces acting on some joints. In particular, for joints 1 and 2, the elasticity is created by the power cables, while an elastic torque produced by a torsional spring is present on joint 4. These torques tend to bring back the joints to their zero angular positions and can be modeled as:

$$\boldsymbol{\tau}_s = \boldsymbol{K}\boldsymbol{q} \ , \tag{2.5}$$

with $\boldsymbol{K} = diag\{K_{e1}, K_{e2}, 0, K_{e4}, 0, 0\}$.
Finally, the mass and inertia properties have been neglected for the last three links, and the corresponding parameters have been set to zero.

MTM arm kinematics

The two MTMs are used to remotely control the two PSMs and the ECM. Both MTMs are almost identical except for their wrists, which are mirrored. Each MTM has eight DOF, with the last not being actuated by a motor and used to control the gripper of the instrument, enabling the user to open and close it. The overall structure may rotate about the vertical axis J_1. The two actuated join s of the parallelogram are those about axes J_2 and J_3. The axes J_4, J_5 J_6 and J_7 intersect in the same point and correspond to revolute joints. Figure 2.6 shows the MTM with the DH frames.

MTM arm dynamics

The computation of the dynamic model of the MTM arm, as for the PSM arm, can be performed using the recursive Newton-Euler approach. The version of the algorithm for closed kinematic chains must be modified to include the parallelogram mechanism. The algorithm allows calculating ing the joint torques $\boldsymbol{\tau}_{MTM} \in \mathbb{R}^n$, taking into account the inertia, Coriolis, centrifugal and gravity torques. The contributions due to joint friction and elastic torques acting on some of the joints are added separately:

$$\boldsymbol{\tau}_{MTM} = \boldsymbol{\tau} + \boldsymbol{\tau}_f + \boldsymbol{\tau}_s \ . \tag{2.6}$$

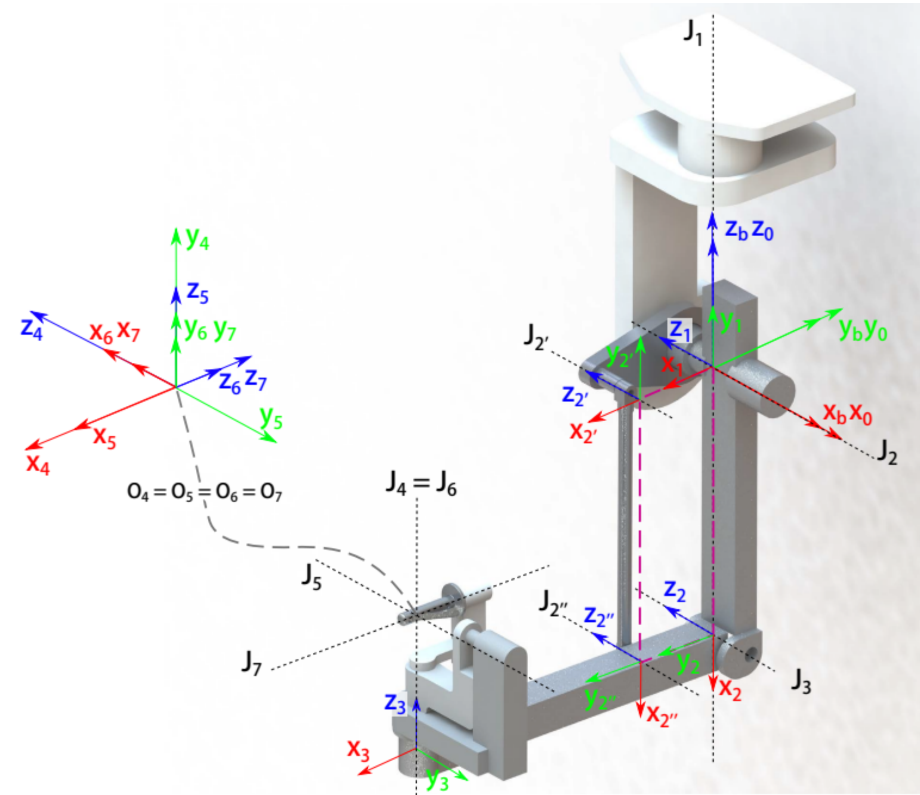

Figure 2.6. Schematic of the MTM kinematics with the DH frames.

The friction contribution $\boldsymbol{\tau}_f$ has been set as the sum of viscous and static friction, as in (2.4), with $\boldsymbol{F}_s$ and $\boldsymbol{F}_v$ set as diagonal matrices. The torque $\boldsymbol{\tau}_s$, set as in (2.5) with diagonal $\boldsymbol{K}_e$, models the elastic torques acting on joint 1, due to the power cables, and on joints 4, 5 and 6, caused by torsional springs.

2.4 Kuka LBR Med

Medical robotics applications in research often use standard commercially available industrial robots for their quality and accuracy. Nevertheless, these systems have to meet the requirements of a variety of domains and tasks, and thus, they usually provide large workspaces and payloads.

In recent years, KUKA released a new lightweight designed for safe physical human-robot interaction, such as KUKA LBR. The LBR Med is a highly efficient and versatile robot that can perform a wide range of tasks in the healthcare industry, such as diagnostics, treatment, and surgical interventions. Its seven-axis lightweight design makes it flexible and easy to integrate into various medical products. This robot is known for its precision and repeatability without requiring additional devices for calibration. It is equipped with an extensive safety structure that includes force/torque sensor systems, single fault safety, safety interfaces, and configurable safety events. Additionally, the LBR Med is based on the KUKA LBR iiwa robot and has redundant integrated torque sensors, making it sensitive to external influences and capable of safe collision detection.

The KUKA LBR Med R800 robot is provided with seven rotational joints with torque sensors for each joint. The modified Denavi-Hartenberg (MDH) link frames are shown in 2.7, where the KUKA Med robot is shown at zero joint position. The MDH Kinematic parameters are listed in [68].

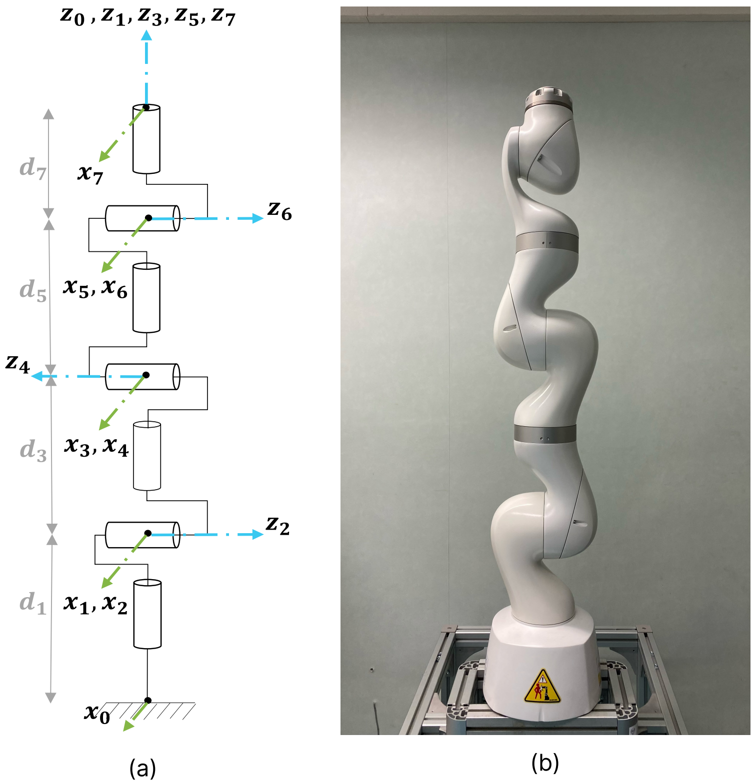

Figure 2.7. Schematic of the Kuka Med kinematics with the MDH frames.

Chapter 3

da Vinci Research Kit Patient Side Manipulator Dynamic Model using Augmented Lagrangian Particle Swarm Optimization

This chapter addresses the problem of the dynamic model of the PSM, starting from the works cited in the literature and the general formulation already presented in Section 2.3. The dynamic model has been modified to take into account a novel friction model definition and computation. The ALPSO algorithm has been utilized to identify the dynamic parameters with a restricted optimization method with physical consistency. A model-based sensorless force estimation method was used to test the dynamic model. Sections 3.2, 3.3 and 3.4 present the methods used for the identification of the dynamical parameters. In Section 3.5, the experimental evaluation is presented.

3.1 Introduction

The dVSS, developed by Intuitive Surgical Inc. in Sunnyvale, CA, is recognized as the leading system for MIRS treatments. It offers significant advantages over traditional surgical equipment, revolutionizing the field of robotic surgery [61].

In surgical robotics, the accurate characterization of the dynamic model is a fundamental requirement. This precise understanding of the model is essential as it lays the foundation for developing and implementing robust control algorithms, optimizing the overall performance and efficiency of robotic systems in surgical environments, and effectively handling the often unpredictable dynamics of the robot. It is crucial in enabling the precise control of the robot's movements and ensuring the smooth, efficient, and accurate execution of complex surgical tasks, which are often characterized by their need for high precision and reliability. Furthermore, the comprehensive understanding of the dynamic model allows researchers and engineers to design and implement control strategies that take into account the robot's interactions with the dynamic and unstructured surgical environment, compensating for external forces and disturbances. Such strategies are vital in maintaining the precision and efficacy of the robot's tasks, which directly impacts the success of surgical procedures.

Dynamic parameter identification is crucial in designing control algorithms for surgical robotics. Traditionally, this has been achieved by using linear regression methods that rely on the linear nature of the robot model. The model comprises specific equations that relate to a particular set of dynamic parameters. Accurate estimation and integration of these parameters result in a robust dynamic model that can be used for designing advanced control algorithms that ensure the safety of surgical robots. These algorithms consider the dynamic properties of the robot and its interaction with the environment, resulting in more precise and responsive control. Integrating these algorithms in surgical robotics reduces the risk of unintended movements and enables smoother and more controlled motions. [69, 70].

Despite significant progress in developing the dynamic model for the dVRK, there are still challenges to overcome, especially regarding friction effects. Most studies assume that the dynamic parameters for the robot joints are linear, which does not fully capture the complexities of the dVRK's cable-driven structure. Nonlinear and undefined elastic effects caused by the cables can impact the accuracy and reliability of the dynamic model, which can affect the performance of control algorithms used in surgical robotics. It is an ongoing research challenge to address these issues and improve the dynamic modeling of the dVRK to enhance the overall performance and safety of the system.

To ensure physical consistency in robotic systems, in all of the approaches cited in Section 2.3, constrained optimization methods such as Linear Matrix Inequality (LMI) are used. These techniques guarantee optimal solutions while preserving the necessary physical features of the system through semidefinite programming [71]. However, using LMI can lead to conservative solutions, resulting in suboptimal performance due to overestimating the constraints. Additionally, satisfying LMIs constraints for physical consistency can be computationally expensive, especially for high-dimensional models such as surgical platforms, and may not fully account for all aspects of physical consistency, such as modeling uncertainties or nonlinear effects. Therefore, it is essential to carefully weigh the trade-offs and consider alternative options when using LMIs for physical consistency in dynamic robot models.

The ALPSO method can help overcome some of the drawbacks of LMIs methods to improve physical consistency [72]. It is an approach for solving optimization issues with constraints, such as physical consistency requirements in dynamic robotics models. ALPSO combines the benefits of Augmented Lagrangian techniques and Particle Swarm Optimization (PSO) to find optimal solutions that fulfill the stated constraints. The performance and accuracy of the dynamic model can be improved by defining the optimization problem with ALPSO to search for solutions that are less conservative than those provided by LMIs. ALPSO can handle non-linear constraints, making it suitable for capturing advanced physical consistency needs.

This work introduces a new and comprehensive dynamic model for the PSM arm of the dVRK robot. In contrast to previous research, the proposed model includes a detailed static friction model that covers static, Coulomb, and viscous friction terms. Moreover, it accounts for the Stribeck effect, which is most observable at low speeds [73]. A significant innovation is the adoption of an arctangent function to ensure the model's continuity around zero velocity, which effectively addresses significant issues caused by friction effects in the cable-driven structure of the dVRK dynamic model. The study employs ALPSO strategy to address constrained optimization problems and uses a superposition method to estimate friction, which differs from conventional optimization methods for parameter identification. The proposed model's validity is confirmed through a force estimation approach, which enables the computation of contact forces between the PSM and surrounding tissues. This force estimation method directly employs dynamic parameters and serves as a validation technique.

The primary goal of this proposed dynamic model is to establish a robust foundation for developing and implementing advanced control techniques on the dVRK robot. By accurately capturing the robot's dynamic behavior and characteristics, this model serves as a strong basis for developing and optimizing control algorithms that can enhance the dVRK system's performance, accuracy, and autonomy.

3.2 Friction Model of the PSM

In section 2.3 a comprehensive overview of the dVRK kinematic and dynamic model in literature is presented. The DH parameters corresponding to the reference frames in Figure 3.1 are provided in Table 3.1. These parameters describe the kinematic relationships between the PSM's joints and reference frames.

As stated above, the proposed work contributed to innovating the formulation of the friction model for the dVRK PSM with respect to the formulation presented in (2.4). Due to the relatively slow movements of the PSM in comparison to other robotic manipulators, a comprehensive classical friction model is used. This model takes into account the Striebeck effect that occurs at low velocities. An arctangent function is included to ensure smooth transitions around the zero-velocity region. The final result is a continuous friction model function that can be expressed using the following equation:

$$\boldsymbol{\tau}_f = \frac{2}{\pi}\arctan(c\dot{\boldsymbol{q}})\left(\left(\boldsymbol{F}_c + (\boldsymbol{F}_s - \boldsymbol{F}_c)e^{-|\dot{\boldsymbol{q}}|/\dot{\boldsymbol{q}}_s}\right) + \boldsymbol{F}_v\dot{\boldsymbol{q}}\right). \tag{3.1}$$

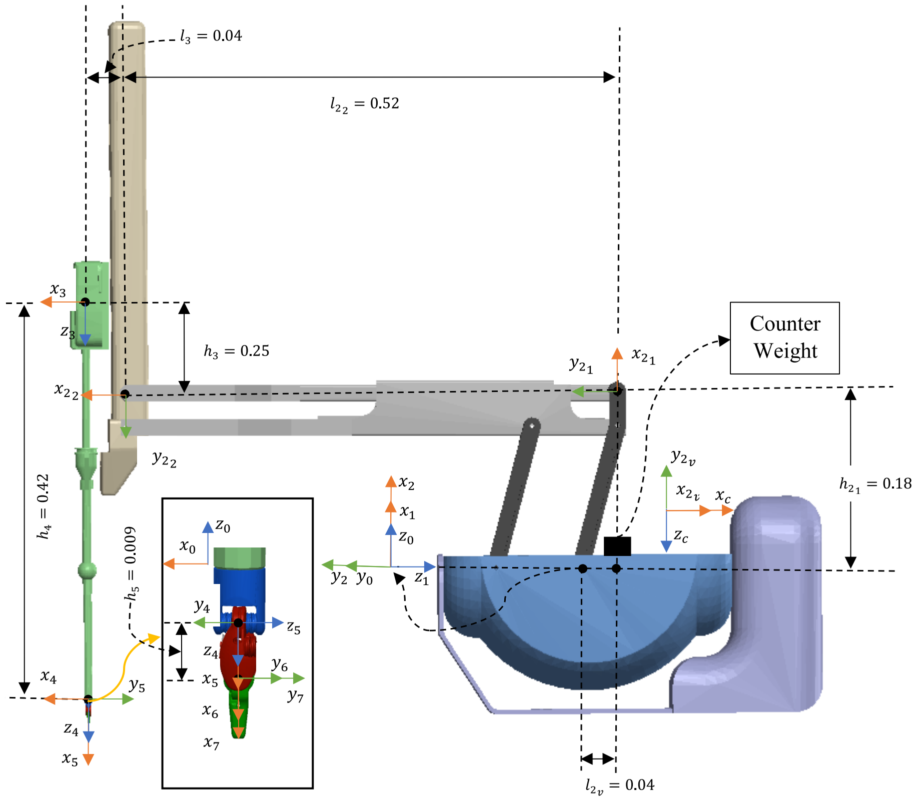

Figure 3.1. Kinematics of the PSM in the dVRK robotic system.

This formulation takes into account predefined linearity and Striebeck velocity constants represented by c and $\dot{\boldsymbol{q}}_s$ respectively. The terms $\boldsymbol{F}_s$, $\boldsymbol{F}_c$, and $\boldsymbol{F}_v$ represent the static friction coefficient, the Coulomb friction coefficient, and the viscous friction coefficient. Incorporating the friction (3.1) in the model (2.2) allows the PSM arm's dynamics to more accurately account for friction, which contributes to improved control and performance. This results in smoother and more precise motion during surgical procedures.

Table 3.1. The DH parameters describe the kinematic properties of the dVRK's PSM arm.

joint	type	prev	succ	a_i	α_i	d_i	θ_i
1	R	—	2	0	$\pi/2$	0	$q_1 + \pi/2$
2	R	1	2_v,c	0	$-\pi/2$	0	$q_{-}\pi/2$
2_v	R	2	2_1	l_{2_v}	0	0	$\pi/2$
2_1	R	2_v	2_2	h_{2_1}	0	0	$-q_2 + \pi/2$
2_2	R	2_1	3	l_{2_2}	0	0	q_2
3	P	2_2	4	l_3	$-\pi/2$	$q_3 - h_3$	0
4	R	3	5	0	0	h_4	q_4
5	R	4	6,7	0	$\pi/2$	0	$q_5 + \pi/2$
6	R	5	—	h_5	$\pi/2$	0	q_6
7	R	5	—	h_5	$\pi/2$	0	q_7
c	P	2	—	0	$-\pi/2$	$q_3/3$	0

3.3 PSM Dynamic Parameters Identification

This section outlines the methodology employed for defining the dynamic model of the PSM. It describes the approach of formulating a constrained optimization problem to identify feasible parameters and introduces a proposed technique for estimating friction. The combination of these methods enables a comprehensive characterization of the PSM's dynamics, ensuring accurate modeling and enhanced performance in surgical applications.

3.3.1 Dynamic Modeling of the PSM

The dynamic model of a rigid robot exhibits linear behavior with respect to various dynamic parameters such as inertia, mass distribution, and friction. These parameters play a crucial role in determining the robot's response and behavior during operation. The aforementioned parameters can be suitably combined to create a set of barycentric parameters, which encapsulate the essential characteristics of the robot's dynamics. In a more extensive context, when condensing the equations governing the PSM as a manipulator with n-DOFs into a compact set of linear equations, the dynamic model can be represented as follows:

$$\boldsymbol{\tau} = \boldsymbol{Y}(\boldsymbol{q}, \dot{\boldsymbol{q}}, \ddot{\boldsymbol{q}})\boldsymbol{\beta} \ . \tag{3.2}$$

The matrix $\boldsymbol{Y} \in \mathbb{R}^{n\times p}$ serves as a regression matrix, dependent on the joint positions, velocities, and accelerations. Meanwhile, the unknown vector $\boldsymbol{\beta} \in \mathbb{R}^{p}$ comprises the dynamic parameters, encompassing a total of p elements. The suitable parameter vector $\boldsymbol{\beta}$ contains the masses (m_i), center of masses location $(l_i : [l_i^x, l_i^y, l_i^z])$, inertia parameters of the links $((I_{xx_i}, I_{xy_i}, I_{xz_i}, I_{yy_i}, I_{yz_i}, I_{zz_i})$, friction coefficients $(F_{s_i}, F_{c_i}, F_{v_i})$ and stiffness coefficients (K_i) of the dynamic parameters of the link i. In total, each robot link involves 16 parameters that require identification. Within the set of dynamic parameters, some parameters do not show themselves in the dynamic model due to the mechanical structure of the manipulator and therefore unidentifiable [74]. To address this issue, numerical decomposition methods can be employed to determine an identifiable minimum subset of dynamic parameters, leading to the following outcome:

$$\boldsymbol{\tau} = \boldsymbol{Y}_r(\boldsymbol{q}, \dot{\boldsymbol{q}}, \ddot{\boldsymbol{q}})\boldsymbol{\beta}_r \ , \tag{3.3}$$

where $\boldsymbol{Y}_r \in \mathbb{R}^{n\times r}$ is the new reduced regression matrix with and $\boldsymbol{\beta}_r$ is the identifiable minimum set of dynamic parameter with dimension $r < p$. All identified dynamical parameters must be physically feasible values to define the consistent dynamical behaviour of the robot. In order to obtain physically consistent parameters, some constraints should be defined. For the generic link L_i, the conditions that guarantee the physical feasibility of the inertial parameters are possible with the positive mass and inertia tensor parameters that are $0 < m_i$, $0 < I_i$. The eigenvalues of the inertia tensors $(\sigma_x, \sigma_y, \sigma_z)$ must adhere to the conditions of the triangle inequality, namely, $\sigma_x + \sigma_y > \sigma_z$, $\sigma_x + \sigma_z > \sigma_y$, and $\sigma_y + \sigma_z > \sigma_x$, as in [75]. The notations l_i^{lb} and l_i^{ub} denote the lower and upper bounds, respectively, associated with the variable l_i. It is crucial to ensure that the center of mass lies within the feasible convex hull, satisfying the conditions $m_i l_i^{lb} < l_i$ and $m_i l_i^{ub} > l_i$, as discussed in [76]. Additionally, the stiffness coefficients K_i must be positive definite, and the friction model coefficients have both upper and lower bounds. The PSM is manipulated using excitation trajectories, to be further detailed in Section 3.3.4, for data collection in the identification process. During the motion of the PSM, the joint angular positions, velocities, accelerations, and torque values are recorded at discrete time intervals, denoted as $t = t_1, t_2, \ldots, t_m$. Equation represented by (3.3) can be expressed in the following form using the recorded samples:

$$\boldsymbol{\tau}_m = \begin{bmatrix} \boldsymbol{\tau}(t_1) \\ \boldsymbol{\tau}(t_2) \\ \vdots \\ \boldsymbol{\tau}(t_m) \end{bmatrix} = \begin{bmatrix} \boldsymbol{Y}_r(\boldsymbol{q}(t_1), \dot{\boldsymbol{q}}(t_1), \ddot{\boldsymbol{q}}(t_1)) \\ \boldsymbol{Y}_r(\boldsymbol{q}(t_2), \dot{\boldsymbol{q}}(t_2), \ddot{\boldsymbol{q}}(t_2)) \\ \vdots \\ \boldsymbol{Y}_r(\boldsymbol{q}(t_m), \dot{\boldsymbol{q}}(t_m), \ddot{\boldsymbol{q}}(t_m)) \end{bmatrix} \boldsymbol{\beta} = \boldsymbol{Y}_m \boldsymbol{\beta}_r \ , \tag{3.4}$$

where $\boldsymbol{\tau}_m$ and $\boldsymbol{Y}_m$ indicate torque vector and regressor matrix respectively. The following constrained optimization problem is defined based on the squared residual error, ($\boldsymbol{\epsilon} = \boldsymbol{\tau}_m - \boldsymbol{\tau}$) of measured torque vector $\boldsymbol{\tau_m}$ and predicted torque vector $\boldsymbol{\tau}$ to identify the dynamic parameters:

$$\begin{aligned} &\underset{\boldsymbol{\beta}_r}{\text{argmin}} \quad ||\boldsymbol{\tau}_m - \boldsymbol{Y}_m \boldsymbol{\beta}_r||^2 \quad \boldsymbol{\beta}_r \in \mathcal{D} \subseteq \mathbb{R}^r \\ &\text{subject to} \quad \begin{cases} \boldsymbol{g}(\boldsymbol{\beta}_r) = 0, & \boldsymbol{g} : \mathbb{R}^r \to \mathbb{R}^{m_e} \\ \boldsymbol{h}(\boldsymbol{\beta}_r) \leq 0, & \boldsymbol{h} : \mathbb{R}^r \to \mathbb{R}^{m_i} \end{cases} \end{aligned} \tag{3.5}$$

where $\boldsymbol{g}(\boldsymbol{\beta}_r)$ and $\boldsymbol{h}(\boldsymbol{\beta}_r)$ represents the m_e equality and m_i inequality constraints respectively and $\mathcal{D}$ denotes search space.

3.3.2 Augmented Lagrangian Particle Swarm Algorithm (ALPSO)

PSO, an intelligent technique based on evolutionary algorithms, has gained popularity in recent years for solving optimization problems. This approach offers advantages such as computational efficiency, quick results, and a random search technique that is not reliant on initial states. The ALPSO approach, which was proposed in the work of [72], offers a viable solution for tackling constrained optimization problems presented in (3.5). The methodology entails an expansion of the fundamental PSO algorithm to effectively address nonlinear equality and inequality constraints in problem-solving. By leveraging the augmented Lagrangian multipliers method, the constrained optimization problem undergoes a systematic transformation into an unconstrained problem, thereby facilitating the optimization process. Considering the following general constrained objective:

$$L(\boldsymbol{x}, \boldsymbol{\lambda}, \boldsymbol{\gamma}) = f(\boldsymbol{x}) + \sum_{i=1}^{m_e+m_i} \lambda_i \theta_i(\boldsymbol{x}) + \sum_{i=1}^{m_e+m_i} \gamma_i \theta_i^2(\boldsymbol{x}) \ , \tag{3.6}$$

$$\theta_i(\boldsymbol{x}) = \begin{cases} g_i(\boldsymbol{x}), & i = 1, \ldots, m_e, \\ \max\left(h_{i-m_e}(\boldsymbol{x}), \frac{-\lambda_i}{2\gamma_i}\right), & i = m_e+1, \ldots, m_e+m_i \end{cases} \tag{3.7}$$

where, $\boldsymbol{\theta}(\boldsymbol{x}) : \mathbb{R}^r \to \mathbb{R}^{m_e+m_i}$ is a penalty function, $\boldsymbol{g}(\boldsymbol{x})$ and $\boldsymbol{h}(\boldsymbol{x})$ define nonlinear equality and inequality constraints and $\boldsymbol{\lambda} = [\lambda_1, \ldots, \lambda_{m_e+m_i}]$ represent Lagrange multipliers. To address the issue of constraint infeasibility, penalty factors $\boldsymbol{\gamma} = [\gamma_1, \ldots, \gamma_{m_e+m_i}]$ are incorporated in (3.6), thereby ensuring that the solution to the optimization problem (3.5) corresponds to both a stationary point and a minimum of $L(\boldsymbol{x}, \boldsymbol{\lambda}, \boldsymbol{\gamma})$, guaranteeing the correctness of the identified parameters. The penalty factors and Lagrange multipliers are updated for the $k+1^{th}$ sample with the following equations [77]:

$$\gamma_i^{k+1} = \begin{cases} 2\gamma_i^k, \ if \ g_i(x^k) > g_i(x^{k-1}) \wedge g_i(x^k) > \varepsilon_g \\ \frac{1}{2}\gamma_i^k, \ if \ g_i(x^k) \le \varepsilon_g \\ \gamma_i^k, \quad else \end{cases} \tag{3.8}$$

$$\lambda_i^{k+1} = \lambda_i^k + 2\gamma_i^k + \theta_i(x^k) \ , \tag{3.9}$$

where $\varepsilon_g \approx 0$ represents the tolerance factor. Like classical PSO algorithm i^{th} particle position and velocity are updated with the following equation set for the k^{th} iteration;

$$\boldsymbol{x}_i^{k+1} = \boldsymbol{x}_i^k + \boldsymbol{v}_i^{k+1} \tag{3.10}$$

$$\boldsymbol{v}_i^{k+1} = w\boldsymbol{v}_i^k + c_1 r_1^k(\boldsymbol{x}_i^{best,k} - \boldsymbol{x}_i^k) + c_2 r_2^k(\boldsymbol{x}_i^{globalbest} - \boldsymbol{x}_i^k) \tag{3.11}$$

where w represents inertia weight, r_1^k and r_2^k are the random numbers to sent the swarm between $0-1$ and c_1, c_2 indicate scaling parameters. Consequently, the solution using the ALPSO method is given by:

$$\boldsymbol{x}_i^{best,k} = \underset{\boldsymbol{x}_i^p}{\operatorname{argmin}} \, L(\boldsymbol{x}_i^k, \boldsymbol{\lambda}_i, \boldsymbol{\gamma}_i), \quad 0 \le p \le k \tag{3.12}$$

$$x_j^{global\,best} = \underset{x_j^k}{\operatorname{argmin}}\, L(x_j^k, \boldsymbol{\lambda}_j^v, \boldsymbol{\gamma}_j^v)\ , \quad \vee j \tag{3.13}$$

where v and k represent the current iteration of the updating laws and j denotes the particle number [72]. A flowchart of the ALPSO algorithm steps is shown in Figure 3.2. The solutions to this problem can be found numerically using the software tools PYOPT package [78]. It's worth mentioning

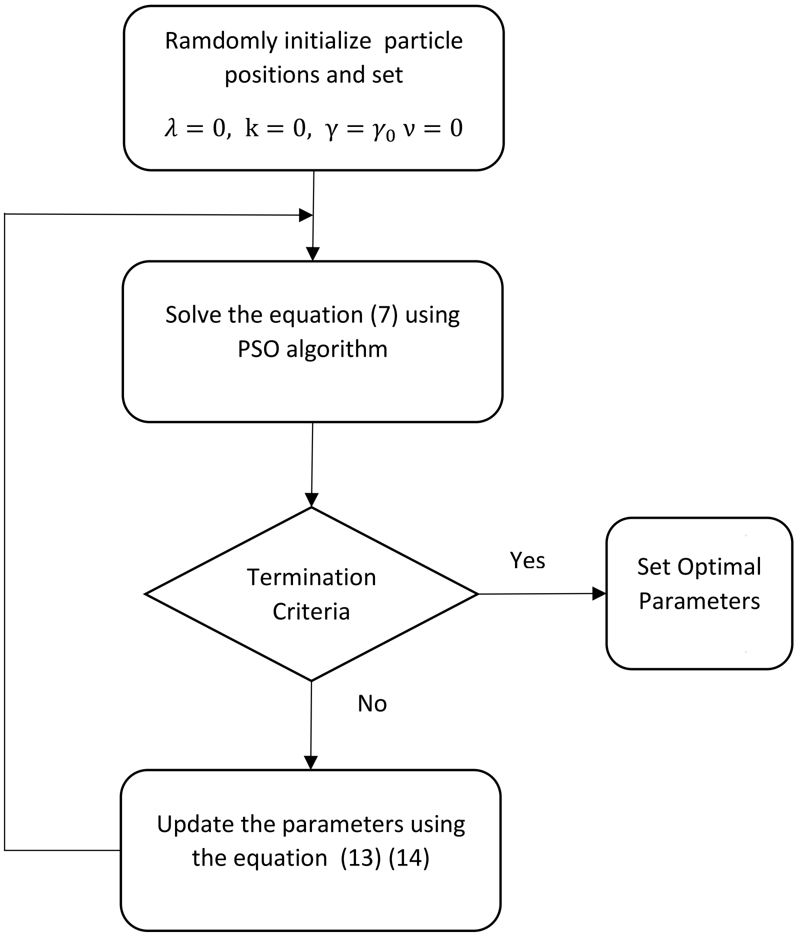

Figure 3.2. Flowchart of the ALPSO algorithm.

that the presented ALPSO solution offers several advantages over the LMI approach, such as flexibility for non-linear and complex constraints, global optimization capabilities, no need for convexity assumptions, robustness in noisy environments, parallelization support, and fewer restrictions on problem formulation.

3.3.3 Friction Estimation

The high dimensionality resulting from the large number of robot joints and the corresponding parameters to be identified poses challenges in obtaining feasible parameter solutions within the optimization problem presented in (3.5). Identifying the dynamic model parameters through the superposition method can reduce the overwhelming computational load of the optimization problem and make it easier to obtain feasible parameter sets. As proposed in [79], the friction model can be separated using the constant velocity movements for a single joint, further facilitating the parameter identification process. Since only one axis (axis m) of the PSM is moving at a constant velocity, the first term $\boldsymbol{B}(\boldsymbol{q}\ddot{\boldsymbol{q}})$ in the robot dynamic model given by (2.2) becomes zero. The Coriolis force becomes zero and the centrifugal force does not produce any effect on the moving joint torques. At the same time, the second term $\boldsymbol{C}(\boldsymbol{q}, \dot{\boldsymbol{q}})\dot{\boldsymbol{q}}$ also results in zero and the remaining dynamical model becomes $\boldsymbol{\tau}_i = \boldsymbol{G}(\boldsymbol{q}) + \boldsymbol{\tau}_f(\dot{\boldsymbol{q}})$, when moving the robot with constant velocity in positive ($\dot{\boldsymbol{q}}_f^+$) and negative ($\dot{\boldsymbol{q}}_f^-$) direction:

$$\begin{aligned} \boldsymbol{\tau}_i(\boldsymbol{q}_f^+) &= \boldsymbol{G}(\boldsymbol{q}_f^+) + \boldsymbol{\tau}_f(\dot{\boldsymbol{q}}_f^+) \ , \\ \boldsymbol{\tau}_i(\boldsymbol{q}_f^-) &= \boldsymbol{G}(\boldsymbol{q}_f^-) + \boldsymbol{\tau}_f(\dot{\boldsymbol{q}}_f^-) \ , \end{aligned} \tag{3.14}$$

where the gravitation torque $\boldsymbol{G}(\boldsymbol{q}_f)$ remains the same for the same joint position. Subtracting (3.14), the friction torque for this velocity can be isolated and calculated as:

$$\boldsymbol{\tau}_f(\dot{\boldsymbol{q}}_f) = \frac{\boldsymbol{\tau}_i(\boldsymbol{q}_f^+) - \boldsymbol{\tau}_i(\boldsymbol{q}_f^-)}{2} \ . \tag{3.15}$$

Moving one axis of the PSM at different constant velocities, the resulting torques in (3.15) give a torque-velocity relationship curve with the symmetric negative direction effect.

3.3.4 Optimal Trajectory Generation

An optimal trajectory that is used for experimentally exciting the robot joints is an important condition of the accurate, reliable, fast, and efficient identification of the dynamic model parameters. The excitation trajectories should be sufficiently rich and must excite all the modelled dynamics of the robot. In this study, finite Fourier series-based optimal excitation trajectories are employed. Creating an optimal robot excitation trajectory necessitates nonlinear optimization considering various constraints, including motion limitations in joint space angular position, velocity, acceleration, and task space collision avoidance. Notably, the model parameter vector $\boldsymbol{\beta}$ is independent of the joint torque and position measurements, based on the maximum-likelihood criteria [80]. Consequently, the problem of generating an optimal trajectory can be defined as minimizing the condition number of the regression matrix $\boldsymbol{Y}_M$ [81]. The joint angular position, velocity, and acceleration trajectories for joint i can be expressed using the following formulations [82].

$$\begin{aligned}
q_i(t) &= \sum_{n=1}^{N} \frac{a_{n,i}}{w_f n} \sin(w_f n t) - \frac{b_{n,i}}{w_f n} \cos(w_f n t) + q_{0,i} \ , \\
\dot{q}_i(t) &= \sum_{n=1}^{N} a_{n,i} \cos(w_f n t) + b_{n,i} \sin(w_f n t) \ , \\
\ddot{q}_i(t) &= \sum_{n=1}^{N} -a_{n,i} w_f n \sin(w_f n t) + b_{n,i} w_f n \cos(w_f n t) \ ,
\end{aligned} \tag{3.16}$$

where w_f defines frequency and N is the harmonics number. The sine and cosine constants of the sinusoidal functions $a_{n,i}$ and $b_{n,i}$ and the initial joint positions $q_{0,i}$ constitute the $2N + 1$ parameters that have to be identified per joint. The constraints imposed on each joint variable, encompassing position, velocity, and acceleration, as well as task space position bounds, can be mathematically expressed as follows:

$$\begin{aligned} q_{min,i} \leq & q_i \leq q_{max,i} \ , \\ \dot{q}_{min,i} \leq & \dot{q}_i \leq \dot{q}_{max,i} \ , \\ \ddot{q}_{min,i} \leq & \ddot{q}_i \leq \ddot{q}_{max,i} \ , \\ x_{min,i} \leq & x_i \leq x_{max,i} \ . \end{aligned} \tag{3.17}$$

Here, the subscripts min and max denote the minimum and maximum values of the respective variables:

$$\begin{aligned} q_{min,i} \leq & q_i \leq q_{max,i} \ , \quad \dot{q}_{min,i} \leq \dot{q}_i \leq \dot{q}_{max,i} \ , \\ \ddot{q}_{min,i} \leq & \ddot{q}_i \leq \ddot{q}_{max,i} \ , \quad x_{min,i} \leq x_i \leq x_{max,i} \ . \end{aligned} \tag{3.18}$$

3.4 External Force Estimation

Sensorless force estimation is vital for validating robot dynamic models by measuring contact forces without additional force sensors. It ensures model accuracy in real-world interactions, particularly when external forces impact the robot's motion and stability. Cost-effective and less intrusive, sensorless estimation enhances robot performance and robustness. The estimated model is validated through sensorless external force estimation using a nonlinear dynamic observer, as described in [83,84]. This approach utilizes joint positions and applied torques acquired through a technique for robot actuator fault detection and isolation. The method relies on the generalized momentum of the robot to calculate a residual vector, enabling accurate force estimation without the need for additional sensors. The identified dynamic model can be expressed as:

$$\boldsymbol{B}(\boldsymbol{q})\ddot{\boldsymbol{q}} + \boldsymbol{C}(\boldsymbol{q}, \dot{\boldsymbol{q}})\dot{\boldsymbol{q}} + \boldsymbol{G}(\boldsymbol{q}) = \boldsymbol{\tau} + \boldsymbol{\tau}_{ext} \ . \tag{3.19}$$

Here, $\boldsymbol{\tau} \in \mathbb{R}^n$ denotes the measured torque vector, while $\boldsymbol{\tau}_{ext} = \boldsymbol{J}^T(\boldsymbol{q})\boldsymbol{F_c}$ represents external torques resulting from contact forces $\boldsymbol{F_c}$. The residual vector denoted as $\boldsymbol{r}$, is described as:

$$\boldsymbol{r} = \boldsymbol{K_I}\Big(\boldsymbol{B}(\boldsymbol{q})\dot{\boldsymbol{q}} - \int_0^t \left(\boldsymbol{\tau} + \boldsymbol{C}^T(\boldsymbol{q}, \dot{\boldsymbol{q}})\dot{\boldsymbol{q}} - \boldsymbol{G}(\boldsymbol{q}) + \boldsymbol{r}\right) d\sigma\Big) \ , \tag{3.20}$$

where $\boldsymbol{K_I}$ represents a diagonal and positive definite gain matrix. The dynamic evolution of $\boldsymbol{r}$ is given by $\dot{\boldsymbol{r}} = \boldsymbol{K_I}(\boldsymbol{\tau_{ext}} - \boldsymbol{r})$. When the gain matrix is sufficiently large, $\boldsymbol{r} \simeq \boldsymbol{\tau_{ext}}$, where $\boldsymbol{\tau_{ext}}$ denotes the external torque. Consequently, the external force can be estimated as $\hat{\boldsymbol{F}}_c = \left(\boldsymbol{J}^T(\boldsymbol{q})\right)^* \boldsymbol{r}$, where $\left(\boldsymbol{J}^T(\boldsymbol{q})\right)^*$ represents the pseudo-inverse matrix of the transposed Jacobian matrix of the robot.

3.5 Experimental Evaluation

The experimental setup in this study involves using the dVRK robotic platform located at the ICAROS Center of Università degli Studi di Napoli Federico II. This section presents dynamic model parameter identification, model validation, and evaluation of external force estimation.

3.5.1 Parameter Identification and Model Validation

During the initial phase of the study, optimal excitation trajectory parameters are identified through the resolution of a constrained nonlinear optimization problem using the ALPSO algorithm, as detailed in Section 3.3.4. Figure 3.3 visually depicts the generated reference values for the joint position, velocity, and acceleration of the PSM throughout the identification process. These carefully designed trajectories play a crucial role in efficiently collecting data for parameter identification and model validation, ensuring accurate and reliable results for the subsequent stages of the study.

In the second phase, the focus shifts to identifying the friction torque of each PSM joint. To achieve this, the joints are individually moved along different constant velocity trajectories. The constant velocities are experimentally obtained by implementing the trapezoidal velocity curve. This approach allows for the isolation and accurate estimation of the friction torque for each joint, providing valuable insights into the frictional behavior of the robot's mechanisms. The collected data from these experiments form an essential part of the dynamic model parameter identification process, enabling the accurate representation of friction effects in the proposed model.

The average joint torque at constant velocity defines one point on the

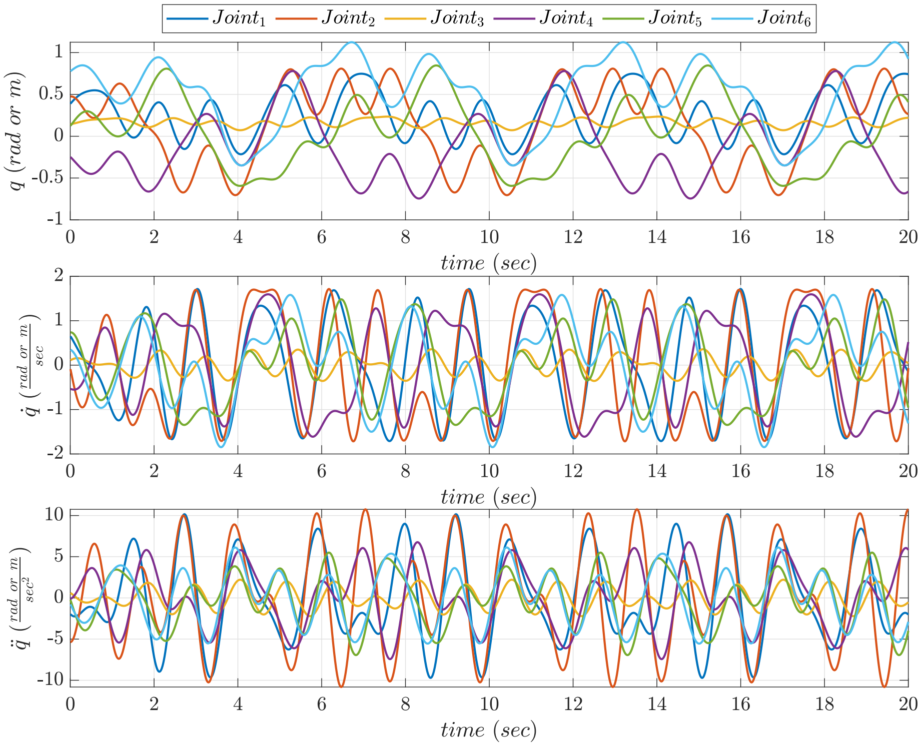

Figure 3.3. Excitation trajectories for the training data.

torque-velocity curve. In Figure 3.4, a comparison between the experimental and estimated friction torque-velocity curves of the PSM joints is depicted. The agreement between the curves validates the accuracy of the proposed dynamic model in capturing the robot joints' friction behavior.

In the third phase, all PSM joints are simultaneously moved using optimal excitation trajectories, and torque and angular motion information are recorded at each time step. The friction joint torques are subtracted from the feedback torque to apply the superposition method. By solving (3.5) using the ALPSO algorithm, a suitable set of dynamic parameters is identified. The measured and computed torques for the identification of the PSM are compared in Figure 3.5. The close alignment between the two demonstrates the effectiveness of the proposed dynamic model in accurately capturing the robot's dynamic behavior.

The validity of the estimated parameters is confirmed by comparing the measured torques with those computed using the identified dynamic model while following the test trajectory. The test trajectories are generated using the same methodology as the training trajectories and are visually represented in Figure 3.6. These test trajectories are also applied to existing PSM models by Fontanelli [64] and Wang [65] to assess the model's performance. The comparison between the measured and computed torques for the PSM is shown in Figure 3.7, demonstrating a close agreement between the two, thereby validating the accuracy of the proposed dynamic model.

The evaluation of the identification process is assessed by computing the relative Root Mean Square Error (RMSE) between the predicted joint torques, denoted as $\boldsymbol{\tau}$, and the corresponding measured torques, denoted as $\boldsymbol{\tau_m}$. This evaluation metric is given by:

$$\boldsymbol{\epsilon} = \frac{||\boldsymbol{\tau_m} - \boldsymbol{\tau}||_2}{||\boldsymbol{\tau}||_2} . \tag{3.21}$$

Table 3.2 shows the comparison between the proposed model and the existing models for the test trajectory. The proposed model performs an average of %12 and %13.2 less relative prediction errors from Wang and Fontanelli's model, respectively, achieving better results.

Table 3.2. Relative joint torque errors comparison (N)($\boldsymbol{\epsilon}$) on the test trajectory with the Wang's model (W), Fontanelli's model (F).

joint	1	2	3	4	5	6	7
W	0.124	0.246	0.329	0.421	0.658	0.426	0.852
F	0.142	0.259	0.327	0.481	0.716	0.382	0.828
N	0.089	0.241	0.295	0.299	0.542	0.316	0.434

The examination of Figures 3.4 and 3.7 reveals that the proportion of friction torques impacting the first three joints relative to the overall joint torque is lower compared to the remaining joints. Compared to other models, the reduction of the torque errors for joints 1, 2 and 3 is less than that for the other joints because friction torque is not dominant at these joints. These findings underscore the significance of investigating the friction model independently within the overall model.

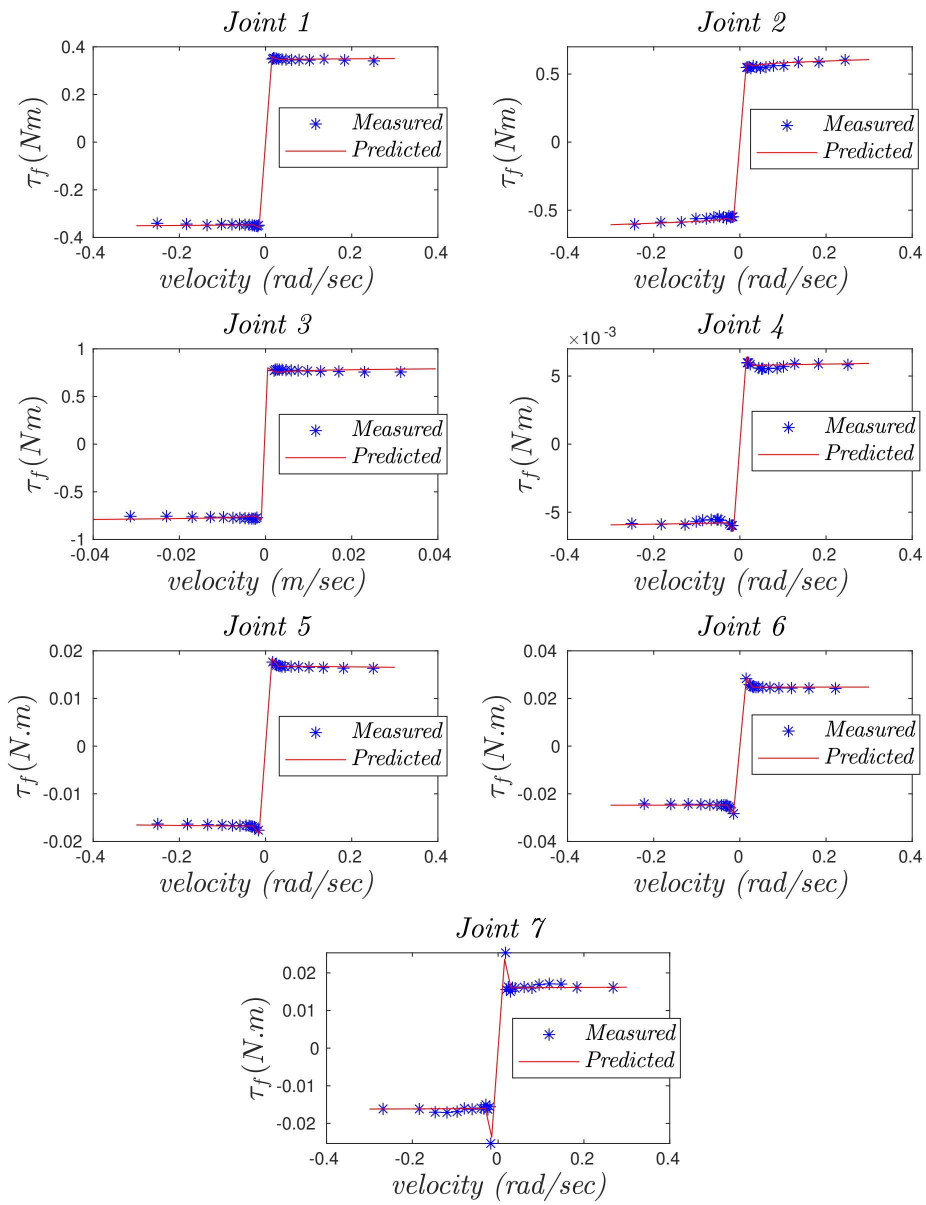

Figure 3.4. Measured and predicted friction torque/velocity curve.

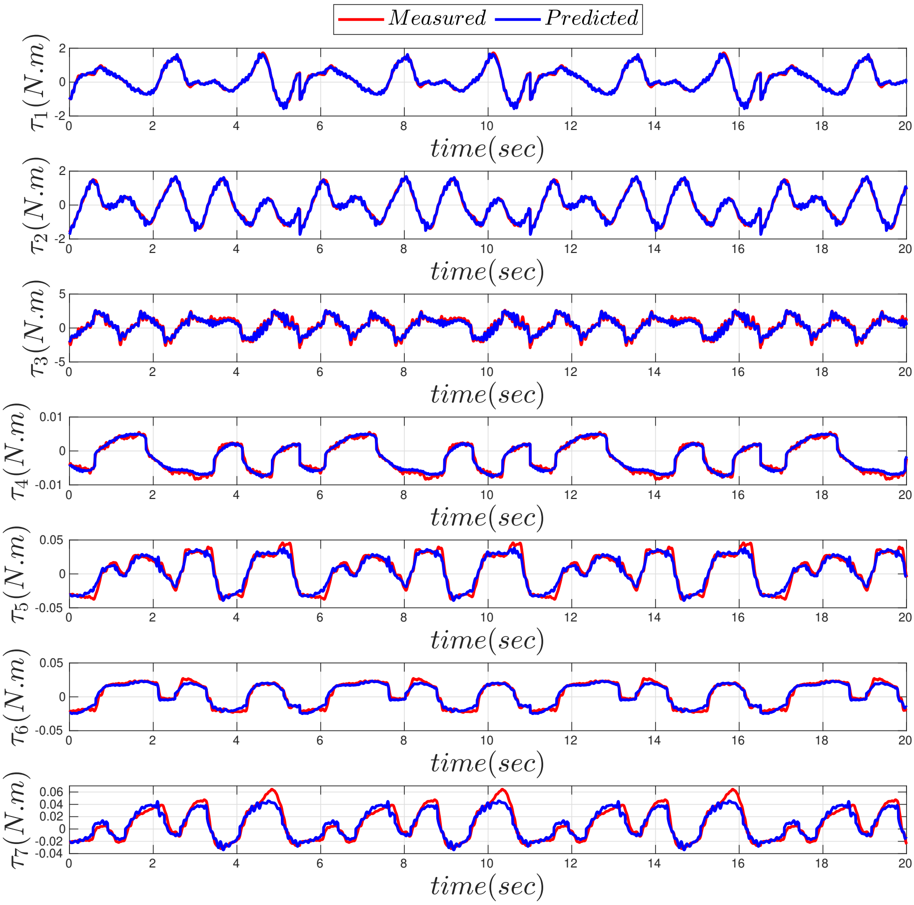

Figure 3.5. Measured and predicted torques on the training trajectory.

3.5.2 External Force Estimation Evaluation

The evaluation phase encompasses two distinct sessions, each comprising three tests to assess the performance of the proposed force estimation method. In the first session (Autonomous tests), the PSM operates autonomously, following predefined operational space trajectories designed to interact with a reference force sensor (ATI NANO 17 F/T Sensor) utilized as the ground truth for force measurements. These trajectories guide

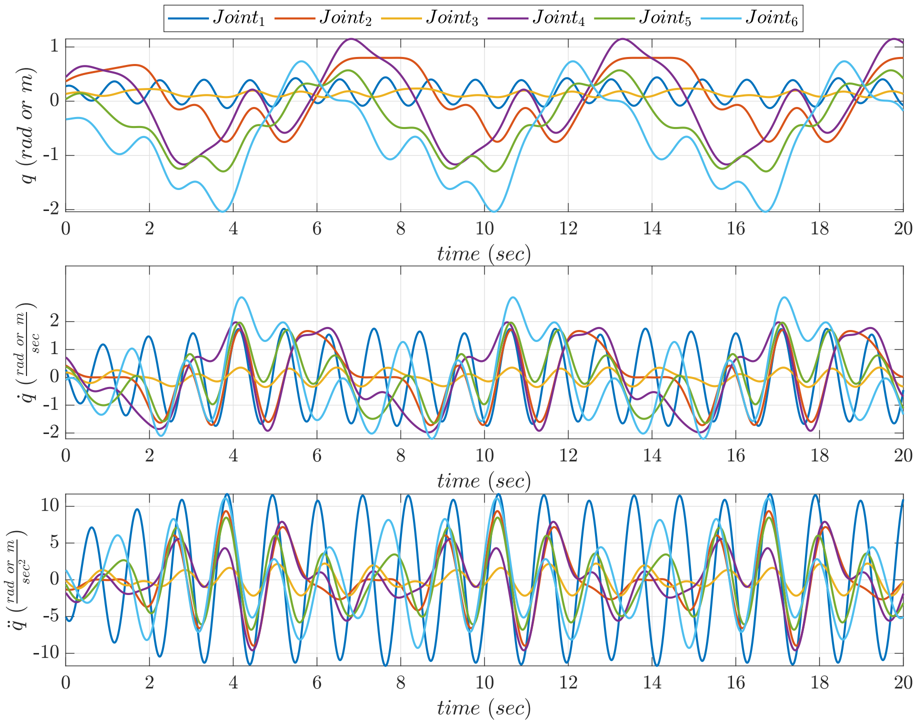

Figure 3.6. Excitation trajectories for the test data.

the PSM along the Cartesian axes (x, y, z) toward the reference force sensor, enabling force estimation comparisons. The robot's end-effector aligns with the corresponding axis of the reference force sensor during the tests, ensuring accurate force readings. In the second session (Teleoperation tests), a human operator takes control of the PSM in teleoperation mode. The operator manually commands the robot's motion along the three Cartesian axes (x, y, z) while monitoring the force estimations. This session evaluates the force estimation method's performance in real-time teleoperation scenarios, where the human operator's input influences the force measurements. The experiments in both sessions aim to validate the effectiveness and accuracy of the PSM dynamic model in different operational scenarios.

Figure 3.9 demonstrates the comparison between the estimated force

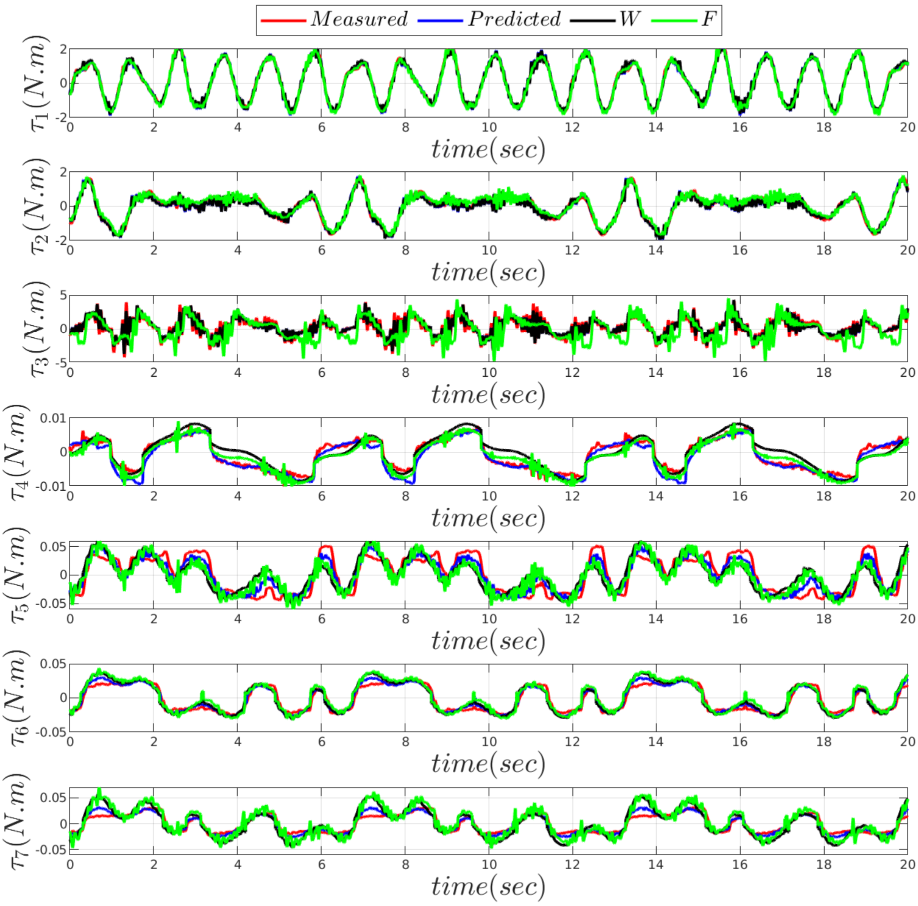

Figure 3.7. Measured and predicted torques on the test trajectory, compared to Wang's model (W) and Fontanelli's model (F).

components (x, y, z), obtained using the proposed residual method, and the corresponding components of the ATI Sensor during the Autonomous tests. In each test, the PSM reaches the ATI Sensor and exerts a force upon it. The estimated forces are compared to the measured ground truth forces, yielding Mean Absolute Errors of 0.0841 N along the x-axis and 0.0709 N and 0.0350 N along the z-axis.

Additionally, Figure 3.10 illustrates the comparison between the esti-

(a) x-axis. **(b)** y-axis. **(c)** z-axis.

Figure 3.8. PSM end-effector interacts with the ATI NANO 17 F/T Sensor along the each axis.

mated force components (x, y, z) derived from the residual method and the corresponding components of the ATI Sensor during the teleoperation movements test. In each test, the human operator touches the ATI Sensor four times while manipulating the PSM. Similar to the previous session, the estimated force components are compared to the measured values, resulting in Mean Absolute Errors of 0.7087 N along the x-axis and 0.6501 N and 0.05 N along the z-axis.

In both experimental sessions, improved force estimation is observed along the z-axis, which corresponds to the insertion axis of the PSM during interaction with the surrounding environment. This phenomenon can be attributed to the prismatic joint movement, which exerts a more significant influence on the insertion force. Conversely, the other two force components exhibit less accurate reconstruction due to factors such as friction and tendon elasticity of the surgical tools, which are challenging to model and identify, as discussed earlier in this chapter. The improved force estimation results, particularly along the z-axis, can be attributed to the accuracy of the dynamic model and the successful identification of dynamic parameters. The comprehensive model, incorporating the novel friction model and other key parameters, captures the robot's dynamics more accurately. This enables more reliable force estimation during interactions with the environment. Although challenges remain in reconstructing the x and y force components, the overall success underscores the importance of a well-

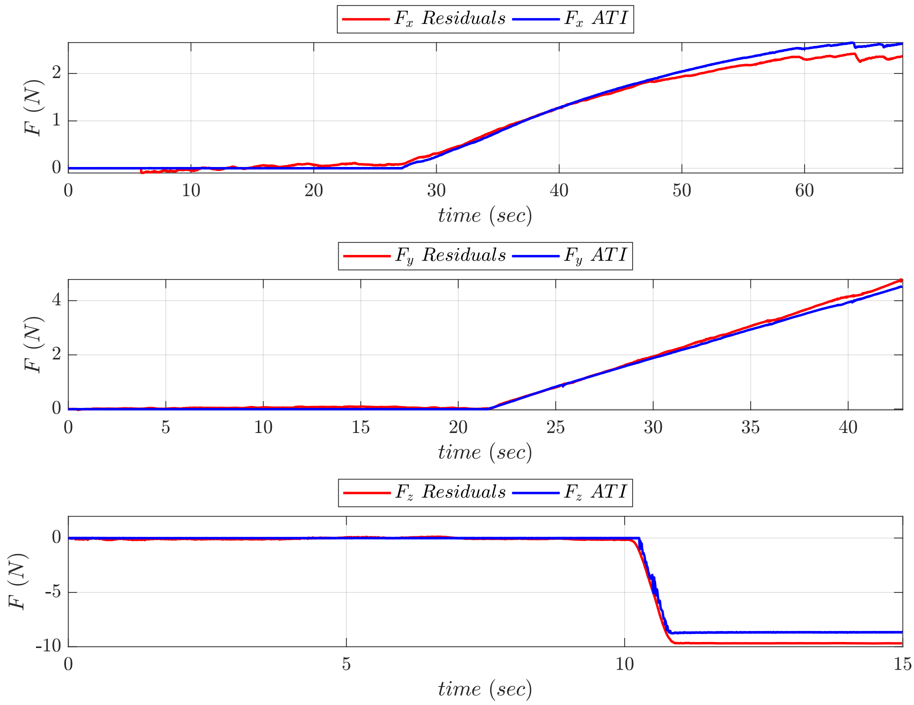

Figure 3.9. Measured and estimated force in the autonomous tests: the red lines represent the estimated residual forces, while the blue lines define the measured ATI forces.

defined dynamic model and advanced parameter identification techniques in enhancing force-sensing capabilities in robotic surgical systems.

3.6 Conclusion

This chapter presents a novel and comprehensive dynamic model for the PSM arm of the dVRK robot. One of the key objectives is to ensure feasible parameter identification, which is critical for achieving accurate and reliable control of the robot. In addition, the study aims to improve friction model usage in the dynamic modeling process, as friction plays a crucial role in the performance and behavior of the robot. To achieve this, the dynamic parameters of the PSM are identified in two stages using the

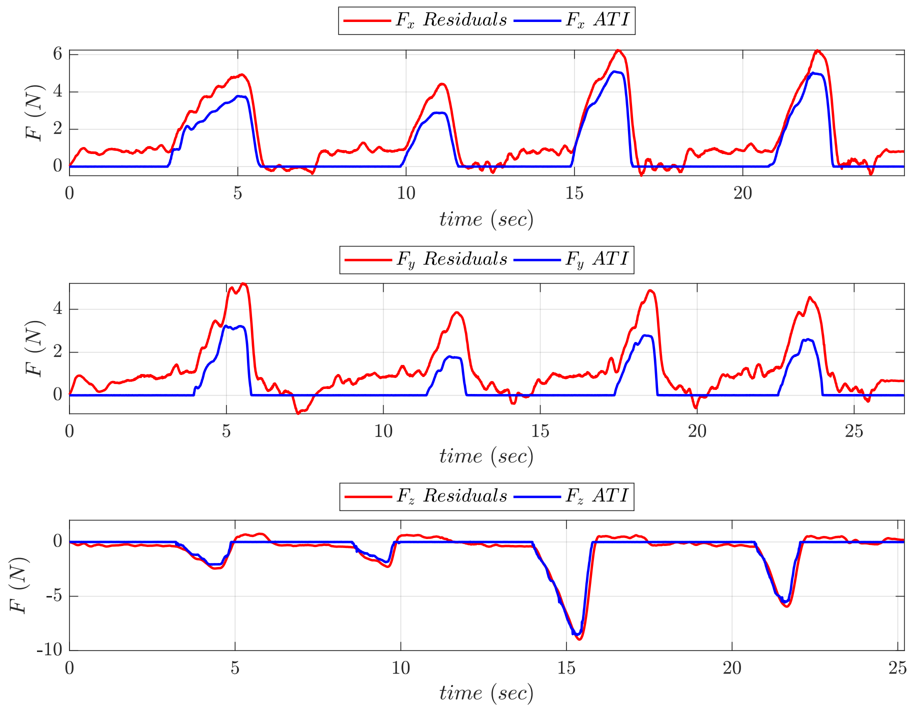

Figure 3.10. Measured and estimated force in the teleoperation tests: the red lines represent the estimated residual forces, while the blue lines define the measured ATI forces.

superposition method. The first stage focuses on determining the friction model parameters, which are vital for accurate torque prediction and control. The second stage deals with the identification of the remaining model parameters, such as inertia and mass distribution, which collectively form the barycentric parameters of the manipulator. Validation tests are conducted to assess the performance of the proposed dynamic model. The tests involve comparing the predicted torques obtained from the proposed model with the actual measured torques during the execution of a predefined test trajectory. The results demonstrate a significant improvement, with a reduction of approximately $\sim \%12$ in the RMSE relative error for all joints when compared to the existing model in the literature.

Furthermore, the proposed dynamic model is tested using an external force estimation method. Two different evaluation sessions are considered: autonomous mode, where the robot operates independently, and teleoperation mode, where the robot is controlled by a human operator. The experimental results show promising outcomes in dynamic model validation. The precise dynamic model enhances the reliability of force estimation during interactions with the environment. Notably, the model's capability to account for the prismatic joint movement significantly improves force estimation along the z-axis during insertion. While challenges persist in accurately reconstructing the x and y force components due to friction and tendon elasticity of surgical tools, the overall success of the force estimation results is largely attributed to the robust dynamic model and successful identification of dynamic parameters.

Chapter 4

Vision-based Dynamic Virtual Fixtures for Tools Collision Avoidance

In RAS, during the execution of typical bimanual procedures such as dissection, surgical tools can collide and create serious damage to the robot or tissues. The dVSS is one of the most advanced and certainly the most widespread robotic platforms dedicated to MIS. Although the procedures performed by da Vinci-like surgical robots are teleoperated, potential collisions between surgical tools are a very sensitive issue declared by surgeons. Shared control techniques based on VF can effectively help the surgeon prevent tool collision. This chapter presents a surgical tools collision avoidance method that uses FRVF. Tool clashing is avoided by rendering a repulsive force to the surgeon. To ensure the correct definition of the VF, a marker-less tool tracking method using deep neural network architecture for tool segmentation is adopted. The use of direct kinematics for tool collision avoidance is affected by tool position error introduced by robot component elasticity during tool interaction with the environment. On the other hand, kinematics information can help in case of camera obstructions. Therefore, this work proposes an EKF for pose estimation which ensures a more robust application of VF on the tool, coupling vision and kinematics information. The method is completely detailed in Section 4.2. The entire pipeline is tested in different tasks using the dVRK system, as explained in 4.3.

4.1 Introduction

MIRS has completely changed surgical procedures. Enhanced dexterity, ergonomics, motion scaling, and tremor filtering are well-known advantages introduced with respect to classical laparoscopy. With the dVSS the surgeon performs tasks in teleoperation mode using only visual information of the surgical scene provided by a 3D stereo viewer. During the execution of a surgical procedure, two or more tools can come dangerously close to each other. The surgeon has a very limited vision on the surgical site, which reduces dexterity and increases the cognitive workload, making the task most difficult to perform. The surgeon's view may be insufficient to avoid collisions, which could result in damage to the tools or surrounding tissue. Experienced surgeons develop strong capabilities to compensate for the lack of haptic information, recreating the perception of haptic feedback from visual cues of the surgical scene [85]. However, recent studies demonstrate different performances in MIRS procedures between experienced and novice surgeons, suggesting that haptic feedback affects performances differently based on the operator's level of experience with the robot [86]. Actually, haptic feedback could significantly affect the performances of novice surgeons, reducing training duration and improving the effectiveness of the procedures. A large number of surgical tasks can benefit from the introduction of collision avoidance techniques. During robotic polypectomy, one surgical tool has to cut around the polyp while another tool keeps raising the surface of the polyp [28]. In this procedure, the surgeon performs a first cutting operation, then lifts the surface of the polyp and executes another cutting task. Automatic robotic assistance to avoid collision between the surgical tools can alleviate the surgeon's workload during the execution of this task and can allow the surgeon to focus on following the polyp margins. In procedures requiring tissue removal with the use of electrocautery, the direct coupling that occurs with a conductor, such as another tool, could burn non-targeted tissue [87]. Collision between surgical tools in MIRS can be avoided by applying advanced shared control techniques. In particular, VF can impose collision avoidance by rendering haptic cues to the surgeon. FRVF restrict the motion of the robot's tool tip through a repulsive force rendered to the surgeon. The dVRK is an open-source mechatronic system, constituted by the first generation of the dVSS equipped with electronics, firmware, and software developed on purpose to create an open control architecture. The dVRK allows testing new control methods, and it is already used to test VF-based methods [28] [26]. Since dVRK robot joints are driven through cables that introduce elasticity, backlash and non-linear friction [88], tools position information obtained through direct kinematics is affected by errors and thus requires correction. Therefore, to ensure a correct application of the VF, a method for surgical tool tracking is strictly needed.

4.1.1 Contribution

This work proposes a surgical tool collision-avoidance method in MIRS. The goal is to improve safety in surgical procedures, enhancing especially novice surgeon's abilities. The method is tested on the dVRK. FRVF are used to avoid surgical tool clashing, by rendering a repulsive force to the surgeon which is inversely proportional to the distance between tools. The method includes a marker-less surgical tool tracking technique using an EKF that couples vision and kinematics information to enhance the robustness of VF application. Visual information allows to overcome the large position error that occurs on the dVRK kinematics, especially when the surgical tools interact with the environment. In contrast, kinematics data reinforce the method in the presence of visual occlusions. To validate the method, an extensive study involving human subjects is conducted on two groups of six surgeons, namely experts and novice surgeons. The goal is to demonstrate significant improvement in performances caused by the introduction of force cues. The pipeline of the method is articulated as follows:

1. Pre-operative calibration and stereo endoscopic image acquisition;

2. Tool segmentation and tooltip pose estimation from vision algorithm;

3. Kinematic and vision data fusion with EKF;

4. VF generation and force rendering.

4.2 System Description

4.2.1 dVRK Robot

The dVRK robot is composed of two PSMs and an ECM commanded by two MTMs. Full control of the dVRK robotic arms is possible thanks to an open controller developed by [89]. To generate force cues, as in [28] the MTMs are controlled through an impedance controller. The surgical scene can be seen by the surgeon thanks to an endoscope, including a stereo camera with a 5 mm baseline. In Figure 4.1, the reference frames definition is shown. The base frame, $\mathcal{F}_{b1} : (O_{b1} - x_{b1}y_{b1}z_{b1})$, is positioned at the PSM1 RCM. Likewise, $\mathcal{F}_{b2} : (O_{b2} - x_{b2}y_{b2}z_{b2})$ is the base frame centered in the PSM2 RCM. All the measurements in this work will be expressed referring to the base frame $\mathcal{F}_{b2}$ of the PSM2. The frames $\mathcal{F}_{g1} : (O_{g1} - x_{g1}y_{g1}z_{g1})$ and $\mathcal{F}_{g2} : (O_{g2} - x_{g2}y_{g2}z_{g2})$ are the grippers frames. The direct kinematics of the dVRK allows computing the current position of the tools in the Cartesian space, providing the coordinates of O_{g1} and O_{g2} in $\mathcal{F}_{b1}$ and $\mathcal{F}_{b2}$ respectively. The reference frames $\mathcal{F}_{t1} : (O_{t1} - x_{t1}y_{t1}z_{t1})$ and $\mathcal{F}_{t2} : (O_{t2} - x_{t2}y_{t2}z_{t2})$ have their origins in the PSM1 and PSM2 tooltips, respectively. The gripper frames $\mathcal{F}_{g1}$ and $\mathcal{F}_{g2}$ have the same orientation as the respective tip frames $\mathcal{F}_{t1}$ and $\mathcal{F}_{t2}$ and the origin of the tip frames are translated of 1 cm along the z-axis of the gripper frames. As in [28], Zhang stereo camera calibration is performed to define the camera reference frame $\mathcal{F}_c : (O_c - x_c y_c z_c)$ and a hand-eye calibration is performed to find the transformation $\boldsymbol{T}_c^{b2}$ between $\mathcal{F}_{b2}$ and $\mathcal{F}_c$. During the calibration process, the tool is placed in ten fixed positions, and the transformation is computed adopting an absolute orientation formulation [90]. A hand-eye calibration is performed to find the transformation $\boldsymbol{T}_{b1}^{b2}$ between the fixed frames of each robotic arm.

4.2.2 Tool Segmentation and 3D Reconstruction

The method directly uses laparoscopic images to track the surgical instrument. A deep learning solution for instrument semantic segmentation is employed. It is based on U-Net architecture, which is a fully convolutional neural network composed of a contracting path to capture context and an expanding path that enables precise localization [91]. The sys-

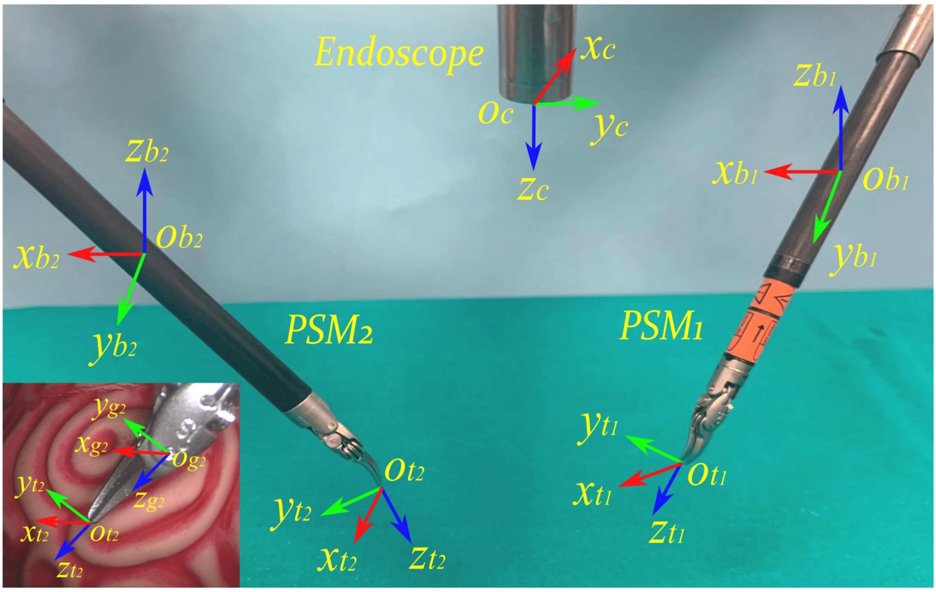

Figure 4.1. Experimental setup and frames definition.

tem adopts the U-Net modification proposed in [92], called TernausNet, which uses pre-trained VGG16 networks as an encoder. The network is trained using the dataset provided for MICCAI 2017 Endoscopic Vision Sub-Challenge: Robotic Instrument Segmentation consisting of 8×225-frame sequences of high-resolution stereo camera images acquired from a da Vinci Xi surgical system during several different porcine procedures, with 2 Hz frame rate. The model's output is an image in which each pixel is the probability value of belonging to the instrument or background area. Then, the binary segmentation is obtained, in which all the instrument pixel values are set as 255, and all the background pixel values are set as 0. The homographic transformation $\boldsymbol{H}$ between the original left and right images is computed, using SIFT for features detection and Fast Library for Approximate Nearest Neighbors (FLANN) for matching, as in [28]. To detect the tooltip on the image plane, the search area range is reduced by re-projecting the tip kinematic position on the image plane and by constructing a rectangle centered on the projected point. Then, the 3D position of the PSM2 tip, expressed in the camera frame $\mathcal{F}_c$, is reconstructed by using a triangulation method with direct linear transform. The tool orientation is computed by solving PnP problem, which allows computing the orientation of the object from a set of n correspondences between 3D points and their 2D projections [93]. In this case, the line of symmetry of the tool is computed, allowing the identification of four specific points on the line in the image plane and their corresponding 3D coordinates, thanks to the knowledge of the tool's geometry. Finally, using transformation $\boldsymbol{T}_c^{b2}$, the tooltip position and orientation of PSM2 is found, expressed in the base frame $\mathcal{F}_{b2}$. Figure 4.2 shows the results of the tool pose estimation method.

4.2.3 Surgical Tool Tracking

For the estimation and tracking of the instrument pose, the EKF is used. Kalman filtering allows combining visual information from the endoscope with the robot kinematics [94]. The entire formulation is referred to PSM2 and the subscript 2 is omitted in this subsection.

The filter provides an estimate of the tool tip pose $\boldsymbol{\zeta} = [\boldsymbol{p}_t, \boldsymbol{q}_t]^T$, being $\boldsymbol{p}_t$ the true tool position, and $\boldsymbol{q}_t = [\eta_t, \boldsymbol{\epsilon}_t]^T$ its quaternion-based true orientation in the base frame $\mathcal{F}_b$. The prediction step provides a preliminary estimation of the instrument pose through the linear and angular velocities of the gripper provided by the manipulator kinematics. Then, the vision-based estimated pose is used in the filter correction step. The process dynamics for the state vector $\boldsymbol{\zeta}$ is given by:

$$\begin{cases} \dot{\boldsymbol{p}}_t = \boldsymbol{v}_g + \boldsymbol{S}\left(\boldsymbol{\omega}_g\right)\boldsymbol{r}_{gt} + \boldsymbol{n}_p \ , \\ \dot{\boldsymbol{q}}_t = \dfrac{1}{2}\boldsymbol{\Omega}\left(\boldsymbol{\omega}_g\right)\boldsymbol{q}_t + \boldsymbol{n}_q \ , \end{cases} \tag{4.1}$$

where $[\boldsymbol{v}_g, \boldsymbol{\omega}_g]^T$ are the linear and angular velocity of the gripper in $\mathcal{F}_b$, $\boldsymbol{S}(\cdot)$ is the skew-symmetric operator, $\boldsymbol{r}_{gt}$ is the position vector of the tooltip respect to the gripper, $\boldsymbol{n} = [\boldsymbol{n}_p, \boldsymbol{n}_q]^T \sim \mathcal{N}(0, \boldsymbol{N})$ is the process noise and

$$\boldsymbol{\Omega}\left(\boldsymbol{\omega}\right) = \begin{bmatrix} 0 & -\boldsymbol{\omega}^T \\ \boldsymbol{\omega} & \boldsymbol{S}\left(\boldsymbol{\omega}\right) \end{bmatrix} . \tag{4.2}$$

The error state vector is defined as $\widetilde{\boldsymbol{\zeta}} = [\widetilde{\boldsymbol{p}}, \delta\widetilde{\boldsymbol{\theta}}]^T$. The orientation error $\delta\widetilde{\boldsymbol{\theta}}$

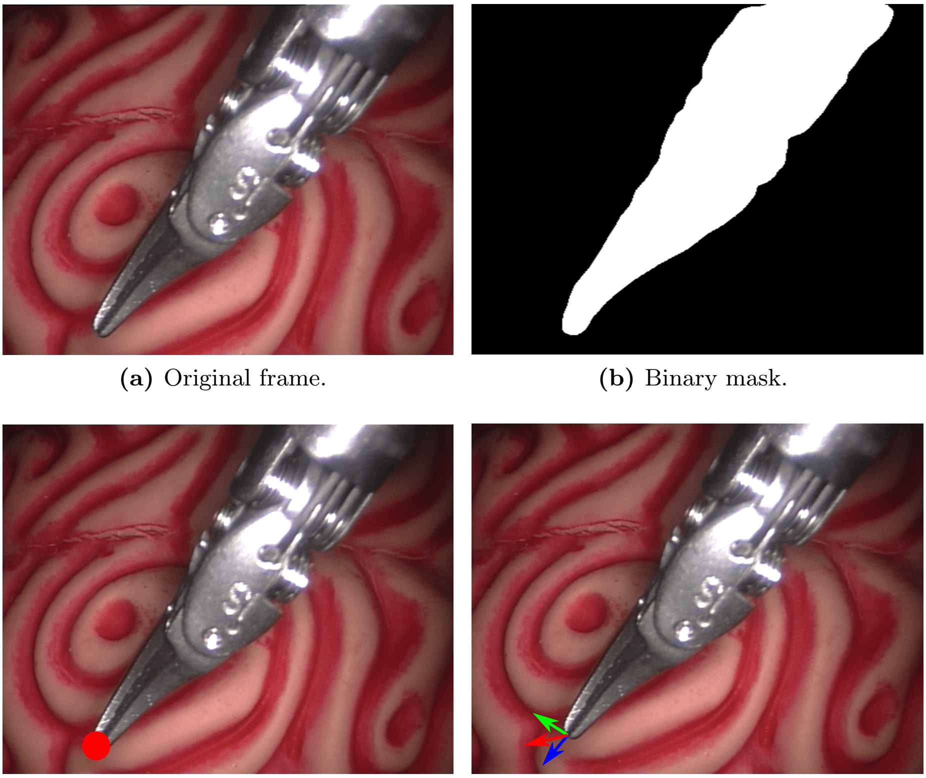

(a) Original frame.

(b) Binary mask.

(c) Point identification in the image plane.

(d) Reference frame definition.

Figure 4.2. Tooltip localization method.

is the 3×1 small-angle approximation vector of the quaternion orientation error. The vision algorithm computes the 3D pose of the tooltip, so the measurement model is given by:

$$\boldsymbol{y} = \boldsymbol{\zeta} + \boldsymbol{m} \,, \tag{4.3}$$

where $\boldsymbol{m} \sim \mathcal{N}(0, \boldsymbol{M})$ is the measurement noise. Then:

$$\boldsymbol{F} = \begin{bmatrix} \boldsymbol{S}(\boldsymbol{\omega}_g) & \boldsymbol{O}_3 \\ \boldsymbol{O}_3 & \boldsymbol{S}(\boldsymbol{\omega}_g) \end{bmatrix} , \qquad \boldsymbol{H} = \begin{bmatrix} \boldsymbol{I}_3 & \boldsymbol{O}_3 \\ \boldsymbol{O}_3 & \boldsymbol{I}_3 \end{bmatrix} , \tag{4.4}$$

where $\boldsymbol{F}$ and $\boldsymbol{H}$ are respectively the control and measurement matrix used in the EKF implementation. The output of the EKF consists in the current pose of frame of PSM2 with respect to the base frame $\mathcal{F}_b$.

4.2.4 Virtual Fixtures Generation

The collision avoidance between the two tools is ensured by the application of a FRVF. To this purpose, the VF is defined as the swept surface along the tool axis, the forbidden region is around the PSM2. The VF has a cylindrical shape with a radius that is double the tool radius.

Assuming that the last two joints are kept still, the cylinder axis direction corresponds to $\boldsymbol{z}_{t2}$ axis of $\mathcal{F}_{t2}$ tracked by the EKF. The current pose of PSM1 is tracked in $\mathcal{F}_{b1}$ using the dVRK kinematics and then mapped in $\mathcal{F}_{b2}$ through the transformation matrix $\boldsymbol{T}_{b1}^{b2}$. The minimum distance between the PSM1 tooltip position $\boldsymbol{x}$ and the cylindrical FRVF corresponds to the length of the line segment which joins perpendicularly the point to the axis minus the radius of the cylinder. A constraint enforcement method is defined, consisting of the application of a spring-damper-like force:

$$\boldsymbol{f}_{vf}(\tilde{\boldsymbol{x}}, \dot{\tilde{\boldsymbol{x}}}) = -\boldsymbol{K}_{vf}\tilde{\boldsymbol{x}} - \boldsymbol{D}_{vf}\dot{\tilde{\boldsymbol{x}}} \;, \tag{4.5}$$

where $\tilde{\boldsymbol{x}} = \boldsymbol{x}_d - \boldsymbol{x}$ is the displacement between the point $\boldsymbol{x}_d$, belonging to the constraint geometry having minimum distance from $\boldsymbol{x}$. The matrices $\boldsymbol{K}_{vf}$ and $\boldsymbol{D}_{vf}$ are properly designed diagonal and positive definite. The external force is not directly measurable. It is estimated by resorting to a non-linear dynamic observer [26], [83], and [84]. Finally, the force imposed by the VF is mapped on the MTM so that it exhibits a repulsive behavior, and it pulls the robot end-effector away from the forbidden region. The MTM impedance controller exhibits a closed-loop behavior that can be described by

$$\boldsymbol{M}\ddot{\tilde{\boldsymbol{x}}} + \hat{\boldsymbol{D}}\dot{\tilde{\boldsymbol{x}}} + \boldsymbol{K}_{vf}\tilde{\boldsymbol{x}} = \boldsymbol{f}_h \;, \tag{4.6}$$

where $\hat{\boldsymbol{D}} = \boldsymbol{D} + \boldsymbol{D}_{\boldsymbol{vf}}$ contains the damping assigned both by the impedance control and the constraint enforcement method.

4.3 Experimental Evaluation

The experimental validation is performed on dVRK robot, which is controlled at the MTM by an impedance controller as described in Section II-A, with $m_{ii} = 1.5$ and $d_{ii} = 0$, being the (i, i) entries of the matrices $\boldsymbol{M}$ and $\boldsymbol{D}$, respectively. The $\boldsymbol{D}_{vf}$ has been adapted according to the stiffness variation such that $d_{vf,ii} = 2\sqrt{m_{ii}k_{vf,ii}}$ where $d_{vf,ii}$ and $k_{vf,ii}$ are the diagonal values of the matrices $\boldsymbol{D}_{vf}$ and $\boldsymbol{K}_{vf}$, respectively and $k_{vf} = 8$ N/m, as in [26]. The dVRK dynamic parameters are identified in [88]. During the experiments, two Endowrist®da Vinci tools are used: curved scissors and Prograsp™ forceps. The kinematics data from the dVRK are acquired at 200 Hz, while the vision-based system estimated the tool position at the camera frame rate of 25 Hz. The EKF approach allows overcoming this limitation, providing tool pose at 200 Hz. The tool segmentation is performed using GPU implementation on an NVIDIA®GTX 1080 Ti to speed up computation.

4.3.1 Tracking Method Evaluation

The proposed tracking method is preliminarily evaluated on a simple task executed with dVRK robot. The task is planned ad hoc to reduce the variability introduced by the telemanipulation and, thus, to obtain a reference target to measure the error. Two specific points, placed on a phantom tissue at a distance of 15 mm, are recorded offline from kinematic data by holding the tool steady in the given positions. In this condition, the position error introduced by the kinematics in the two selected points is minimized since the tool is fixed and the interaction force with the phantom goes toward zero. After that, a linear path is defined analytically between the two points to serve as ground truth for the evaluation. The experiment, conducted to evaluate our tracking method, consists of moving the tool in teleoperation mode along the defined linear path drawn on the phantom. The task is performed slowly, with a duration of 12 seconds, to minimize the error along the linear path introduced by telemanipulation. During the task execution, the surgical tool is tracked using the EKF method. Then, the estimated pose is compared to the target linear path, obtaining mean absolute errors of $0.126 \pm 0.08\, mm$ along the x-axis and $0.02 \pm 0.01\, mm$ along the y-axis. The results demonstrate the goodness of our tracking method. Furthermore, the error obtained just using kinematics information has been computed, obtaining mean absolute errors of $0.135 \pm 0.08\,mm$ along the x-axis and $0.02 \pm 0.01\,mm$ along the y-axis. As expected, the pose error is similar to the one obtained with our tracking method because of the absence of interaction with the environment.

4.3.2 Collision Avoidance Evaluation

The collision avoidance strategy is evaluated in two different tasks. During the first evaluation test, the PSM1 tool is fixed, and the PSM2 is moved by the user in teleoperation mode towards PSM1. The collision avoidance strategy is applied during the entire duration of the test. Figure 4.3 shows the distance between the two surgical tools, computed considering the proposed tracking method, and the related haptic force norm rendered to the user through the master side MTM during the task. The maximum reached force is 3.2 N.

The second evaluation test consists of a human subject study to show significant differences in performance caused by the introduction of force feedback. The study involves 12 subjects divided into two groups, 6 experienced and 6 novice surgeons, based on self-evaluation about their experience using dVSS for minimally invasive surgical procedures. The study is articulated in two experiments using the dVRK robot in teleoperation mode. Taking inspiration from [87], the test simulates burning tissue with an electrocautery device. During each test, the subject keeps the PSM1 centered in the middle of a circle with a diameter of 20 mm. Meanwhile, the PSM2 has to follow the circular path for 270° from a definite starting point, as shown in Figure 4.4. In the first experiment, the subjects perform the test 5 times moving the surgical tool in free motion. In the second experiment referred to as VF constraint tasks, they perform the same task 5 times with the proposed collision avoidance constraint applied. Each task has an average execution time of 10 seconds. Each subject is asked to try the test in advance to become familiar with the task and the dVRK platform. The minimum distance between the tools is considered a performance parameter and computed using the proposed tracking method. In the VF constraint test the maximum force felt during the task is also computed.

Figure 4.5 and Figure 4.6 show the mean values of the minimum dis-

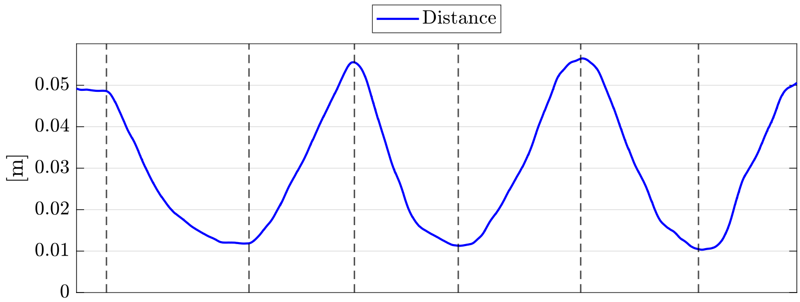

(a) Distance between surgical tools.

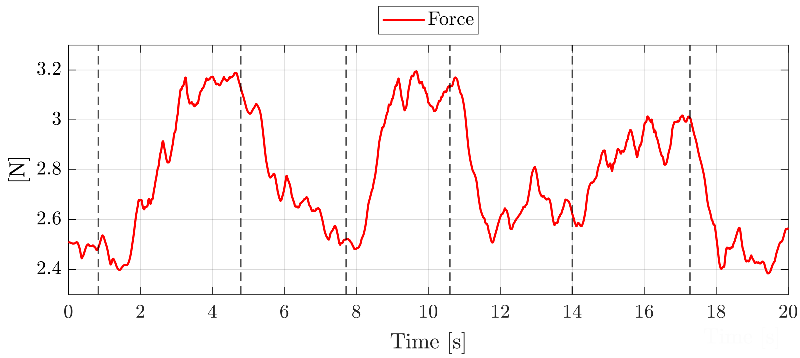

(b) Related estimated force norm.

Figure 4.3. First VF evaluation experiment. Duration: 20 seconds.

tance between tools for novice and expert subjects during free motion and VF constraint tasks. The error bars represent the standard error of the means. To demonstrate the statistical relevance of the results, a comparison is made between the mean values of minimum distance through a statistical unpaired t-test, with a significance level $\alpha = 0.05$. As presented in Table 4.1, the test shows statistically significant differences between the means for all subjects in the novice group. Moreover, it presents an increase in the minimum distance values of $\sim 10\%$ in collision tests with respect to free-hand tests. The estimated force norm, rendered to the novice users through the master side (MTM), during the collision avoidance tasks, has a mean value of $3.1822 \pm 0.5368\,N$. The expert group presents a mean

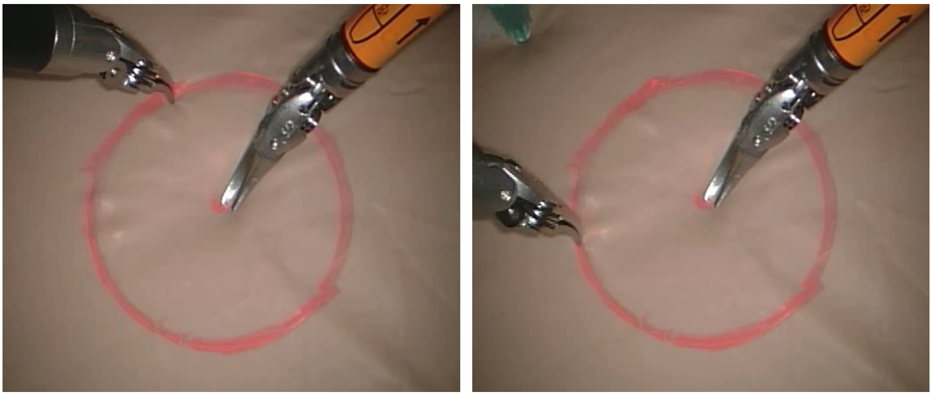

Figure 4.4. Two frames of the second VF evaluation experiment: PSM1 tool holds the center of the circle; PSM2 moves following the circle.

Table 4.1. Maximum force and t-test results on minimum distance for novice and expert users.

Novice	test	p	F_M [N]	Expert	test	p	F_M [N]
1	1	0.0044	2.4416	1	0	0.1352	3.4527
2	1	0.0127	3.0749	2	0	0.0856	2.8175
3	1	0.0030	3.3411	3	0	0.8286	3.5239
4	1	0.0219	2.8188	4	0	0.8757	2.6180
5	1	0.0206	3.9998	5	0	0.1140	3.0035
6	1	0.0012	3.4170	6	0	1	2.8800

force norm of $3.0493 \pm 0.3629\,N$.

Figure 4.4 shows the repulsive force felt at the MTM when the distance between PSMs decreases. The method to generate the force is designed to have small force values so that the surgeon can perceive it slightly. This is because the purpose is not to interfere with the surgeon's actions but to serve as an alarm to remind the presence of the other instrument in the proximity. Indeed, during the experiments, the maximum value of the force norm is 3.2 N.

The human subject study results in 4.5 and 4.6 has shown a statistically significant difference regarding the mean of the minimum distance between the tools for the novice subjects. The VF test outperformed the free-hand test of 75%. This result suggests that feeling a haptic force during the task allows for maintaining a safe distance between the surgical tools. On the

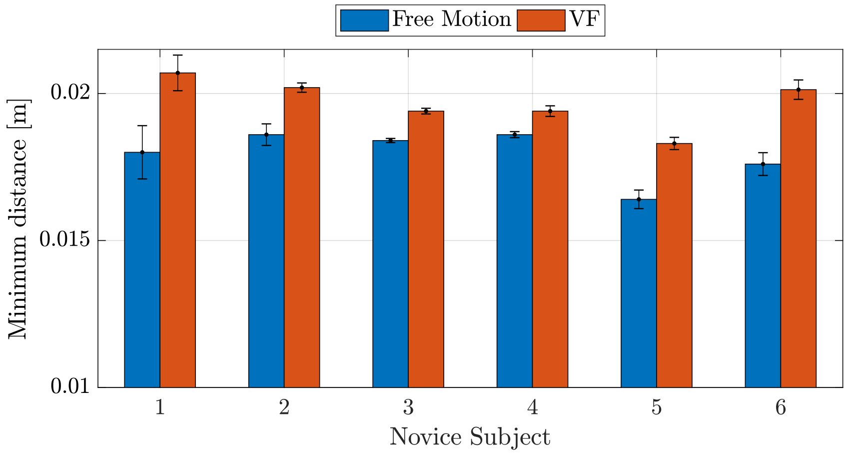

Figure 4.5. Novice subjects: Mean values of minimum distance between tools with standard error bars.

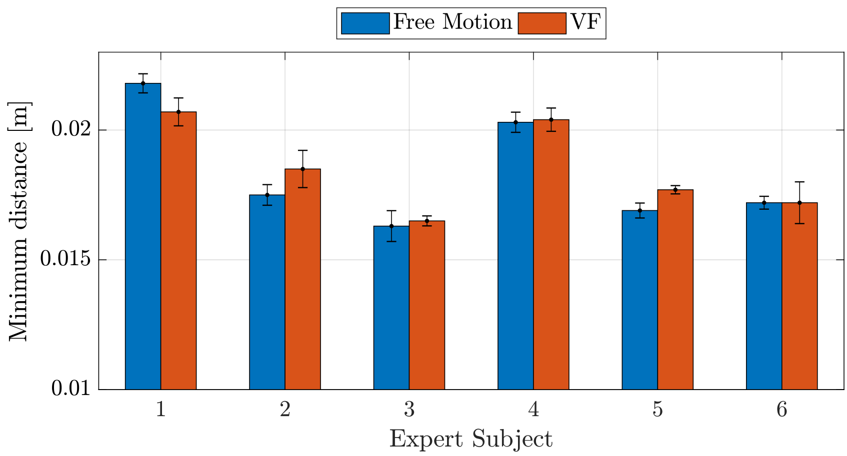

Figure 4.6. Expert subjects: Mean values of minimum distance between tools with standard error bars.

contrary, in the free-hand test, the subject has no force feedback during the task and could dangerously reduce the distance between the tools. The maximum reached force is lower than $4\,N$, and it does not create variation

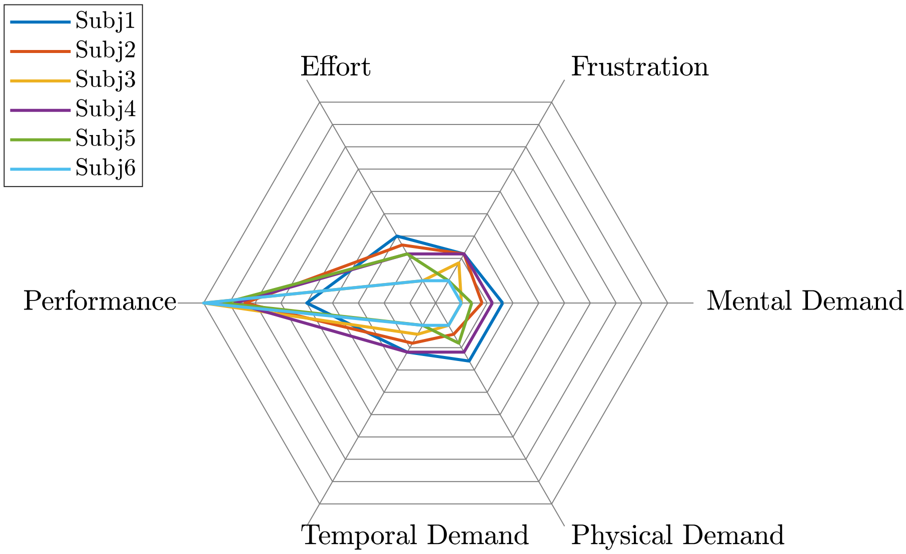

Figure 4.7. Radar graph of the TLX results on expert users.

in the task performance.

As concerns the expert subjects, the test does not show a statistically significant difference in the VF constraint task with respect to the free motion task. Nevertheless, they were asked to compile the NASA-TLX questionnaire [95] to assess the perceived workload. The results of the questionnaires shown in Figure 4.7 assess that the VF constrained task is not mentally, physically and temporally demanding, and the force feedback does not negatively affect the performances. On the contrary, it represents a comfortable reminder of the collision risk that diminishes the user's mental workload. The execution of the main task is not affected by the presence of the VF force since it reaches significant values only at dangerous distances between the tools. Moreover, the flexibility of the method allows us to easily tune the VF based on the level of expertise and confidence of the surgeon. Similar results were obtained for novice surgeons.

4.4 Conclusion

This chapter introduces a method based on VFs that allows avoiding surgical tools collision in MIRS. A marker-less algorithm allows estimating the PSM position and orientation using kinematic and visual information. The PSM estimated pose is used to generate a FRVF that aims to avoid collision between the two instruments through a repulsive force felt at the MTM during the surgical task execution. The proposed strategies are evaluated through multiple experiments on dVRK, showing good results in improving novice surgeon's performance. Furthermore, the use of VF allows an expert surgeon to better focus on the task, as far as the haptic force is small enough to suggest that the tools are dangerously close without affecting the performance. Therefore, the method can be considered effective both in the training stage of novice surgeons and when the level of expertise increases.

Chapter 5

Remote Center of Motion and Virtual Fixture Framework for Human-Robot Interaction

MIRS is characterized by restricted motions of the robotic arm that moves the tool through the entry point into the patient's body. To prevent harm to the patient, the manipulator motion is constrained with respect to a point known as RCM. The presence of a small incision on the patient's body, through which the whole operation is performed, permits less trauma and faster recovery of the patient. However, the drawbacks arising in this context are limited vision of the surgical site, reduced dexterity and increased cognitive workload. VFs have been proven to be an effective way to enhance safety, preventing damages to tissues by constraining the tool into a safe region. This chapter presents a control framework for human-robot interaction in medical application that is characterized by a RCM constraint, enforced in a manual guidance control framework, in which VFs enhance safety of the procedure.

5.1 Introduction

MIRS is a growing field of robotics that aims to enhance precision and dexterity, while reducing invasiveness and overall operation time, resulting in a faster patient recovery time. During MIRS, surgical tools enter the patient's body through a small incision, creating the kinematic constraint of the RCM. The RCM constraint can be active or passive. The passive constraint is maintained mechanically, while the active constraint is achieved with a software controller, as described in [44]. However, actively enforcing the constraint represents a cheaper and more flexible solution, and it allows the employment of a commercial arm in medical applications.

Passive compliant motion control typically involves utilizing either spherical mechanisms or dual-parallelogram structures to implement the RCM that coincide with the desired pivot point. The AESOP system and the dVRK are two examples of systems designed specifically for passive motion control. In [42], Ortmaier *et al.* implemented a Cartesian control algorithm for the AESOP robot, which incorporates passive joints to prevent any force from being applied to the trocar. However, actively enforcing the constraint provides a more flexible solution and enables the use of a commercial arm in medical applications.

In traditional laparoscopic surgeries, surgical tools are inserted into the patient's body through a trocar point. However, there is no control over the stress caused to the tissues by the movement of the tool during the operation. Enforcing an RCM on the shaft will reduce the stress on the tissue, assuring more safety and less post-operative pain. The RCM constraint is not required only in minimally invasive systems but can also be used in various surgical and non-surgical applications. One of the examples is dental implant surgery, where the RCM point can be identified as the entry point of the osteotomy. Another example is mammography, where the scanner needs to move along a spiral on a woman's breast, and the vertex of the spiral can represent an RCM point.

Moreover, during surgical procedures, it may be necessary for the surgical tool to operate in a limited workspace to avoid touching sensitive or dangerous areas. In such cases, VFs can be used to restrict the movement of the robotic arm to specific regions or guide it along a predetermined path. This can help the operator to perform the procedure more accurately and with less mental effort, ultimately reducing task completion time.

In light of the two scenarios mentioned earlier, namely the dental implant surgery and the mammography, it is important to consider different attractive VFs. In the case of oral surgery, a point-like active constraint can be used to align the manipulator with the surgical site. On the other hand, during mammography, the VF needs to be modeled with a spiral shape, which corresponds to the desired path for the procedure on women. In order to address both scenarios, a shared control framework will be investigated.

In this work, a control strategy that ensures both the RCM kinematic constraint and repulsive VFs constraint in a human-robot interaction framework is implemented, in which the doctor guides the manipulator throughout the surgical application. A compliant behavior is obtained thanks to an impedance control. The theory and implementation of impedance control of robotics manipulators have been described in detail in Hogan's work [96] and [97]. The basic idea underlying this control algorithm is to manage the relationship between the robot's motion and external forces, hence reshaping the impedance of the manipulator. There have been different approaches according to the task to be performed and the knowledge about the robot's dynamic model. The control framework has been validated by considering a minimally invasive surgical scenario.

Sections 5.2.1 and 5.2.2 present the implementation of the RCM and the proposed approach for manual guidance and VF enforcement respectively.

5.2 Methods

The proposed control framework allows the surgeon to manually guide the robot while ensuring that the RCM point $\boldsymbol{p}_{RCM} \in \mathbb{R}^3$ is enforced on the trocar point, which is a fixed point in the world frame.

5.2.1 RCM Constraint

The kinematic constraint at the RCM has been implemented following the approach proposed by [46] as it allows direct control over the penetration of the instruments into the patient's body and requires minimal knowledge of the trocar geometry.

The RCM is assumed to lie on a shaft attached to the manipulator's end effector. The position of the RCM over time is given by:

$$\boldsymbol{p}_{RCM} = \boldsymbol{p}_i + \lambda(\boldsymbol{p}_{i+1} - \boldsymbol{p}_i)\ , \qquad 0 \leq \lambda \leq 1 \tag{5.1}$$

where $\boldsymbol{p}_i$ and $\boldsymbol{p}_{i+1}$ denote the boundaries of the shaft. The dependencies of the points coordinate from joint variables and time are omitted for brevity. Differentiating (5.1) and exploiting the differential mapping between the joint space and the operational space, it is obtained:

$$\dot{\boldsymbol{p}}_{RCM} = \boldsymbol{J}_{RCM}(\boldsymbol{q}, \lambda) \begin{bmatrix} \dot{\boldsymbol{q}} \\ \dot{\lambda} \end{bmatrix} , \tag{5.2}$$

where $\boldsymbol{J}_{RCM}$ is the Jacobian of the RCM, given by:

$$\boldsymbol{J}_{RCM} = \begin{bmatrix} \boldsymbol{J}_i + \lambda(\boldsymbol{J}_{i+1} - \boldsymbol{J}_i) & \boldsymbol{p}_{i+1} - \boldsymbol{p}_i \end{bmatrix} . \tag{5.3}$$

To satisfy the RCM constraint, it has to be $\boldsymbol{p}_{RCM} \equiv P_T$, where P_T is the trocar point. Therefore $\dot{\boldsymbol{p}}_{RCM} = \boldsymbol{0}$.

Indicating with $\boldsymbol{t} = \boldsymbol{f}(\boldsymbol{q})$ a generic desired task, and considering the differential kinematics between task and joints velocities, it is possible to derive the differential kinematics of the extended task which includes the above mentioned RCM constraint:

$$\dot{\boldsymbol{t}}_{EXT} = \begin{bmatrix} \dot{\boldsymbol{t}} \\ \boldsymbol{0}_{3\times1} \end{bmatrix} = \begin{bmatrix} \boldsymbol{J}_t & \boldsymbol{0}_{n_t\times1} \\ \multicolumn{2}{c}{\boldsymbol{J}_{RCM}} \end{bmatrix} \begin{bmatrix} \dot{\boldsymbol{q}} \\ \dot{\lambda} \end{bmatrix} = \boldsymbol{J}_{EXT} \begin{bmatrix} \dot{\boldsymbol{q}} \\ \dot{\lambda} \end{bmatrix} , \tag{5.4}$$

where n_t is the dimension of the task space.

To guarantee exponential decoupled convergence of the extended task to a desired value, the following kinematic control has been employed:

$$\begin{bmatrix} \dot{\boldsymbol{q}} \\ \dot{\lambda} \end{bmatrix} = \boldsymbol{J}^{\dagger}_{EXT} \begin{bmatrix} \boldsymbol{K}_t & \boldsymbol{0}_{nt\times3} \\ \boldsymbol{0}_{3\times nt} & \boldsymbol{K}_{RCM} \end{bmatrix} \boldsymbol{e}_t , \tag{5.5}$$

where $\boldsymbol{e}_t = \begin{bmatrix} \boldsymbol{t}_d - \boldsymbol{t} & \boldsymbol{p}_T - \boldsymbol{p}_{RCM} \end{bmatrix}^T$ is the vector containing the task and RCM errors.

The chosen formulation considers the fact that the RCM is a three-dimensional constraint but the modeling of the variation of penetration, $\dot{\lambda}$ in (5.2), adds an extra DOF, which effectively reduces the constraint's dimension to 2. Anyhow, the variation of penetration is necessary in many surgical tasks and must be modeled. In addition, in [47], the equation of the plane tangent to the body is necessary to compute the jacobian of the RCM. This assumption is critical in practical applications since this equation should be determined through a registration procedure prone to

(a) Kuka LBR Med 7 robot, ATI Force/Torque sensor and a shaft mounted mounted on it.

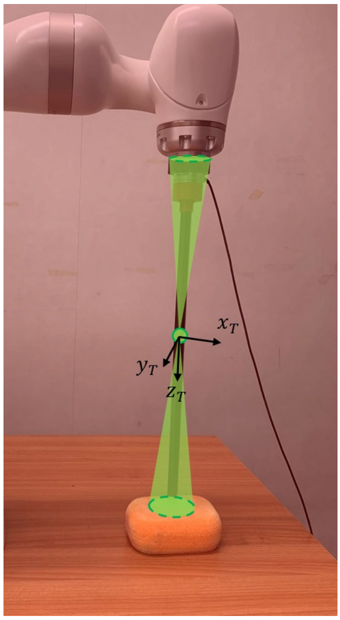

(b) Conical VF.

Figure 5.1. Experimental Setup.

approximations. With the formulation proposed by [46], the computation of this plane is not required. In (5.5), additional tasks could be considered and projected into the null-space of the extended jacobian $\boldsymbol{J}_{EXT}$, thus determining a hierarchical control structure.

5.2.2 Manual Guidance and Repulsive Virtual Fixture

The manual guidance of the manipulator is obtained by implementing an admittance control law following the equation:

$$\boldsymbol{M}\ddot{\boldsymbol{p}} + \boldsymbol{D}\dot{\boldsymbol{p}} + \boldsymbol{K}\boldsymbol{p} = \boldsymbol{f} \ , \tag{5.6}$$

where $\boldsymbol{f} \in \mathbb{R}^3$ is the external force, $\boldsymbol{M}$, $\boldsymbol{D}$, $\boldsymbol{K} \in \mathbb{R}^{3\times 3}$ are positive definite matrix, suitably tuned in order to obtain the desired behavior, and $\boldsymbol{p} \in \mathbb{R}^3$

is the desired Cartesian position, which corresponds to the desired position $\boldsymbol{t}$ as in (5.4).

The reference acceleration $\ddot{\boldsymbol{p}}$, velocity $\dot{\boldsymbol{p}}$ and position $\boldsymbol{p}$ are computed from the force $\boldsymbol{f}$ by integrating the following expression:

$$\ddot{\boldsymbol{p}} = \boldsymbol{M}^{-1}\left(\boldsymbol{f} - \boldsymbol{D}\dot{\boldsymbol{p}} - \boldsymbol{K}\boldsymbol{p}\right) . \tag{5.7}$$

In other words, the quantities $\ddot{\boldsymbol{p}}$, $\dot{\boldsymbol{p}}$ and $\boldsymbol{p}$ represent the desired compliant motion of a virtual body located at tip of the sensor force with mass $\boldsymbol{M}$, damping $\boldsymbol{D}$ and stiffness $\boldsymbol{K}$ under the action of the force $\boldsymbol{f}$ [98]. In the specific application, the parameters are chosen as follows: $\boldsymbol{M} = 8\,\boldsymbol{I}_3\,\mathrm{kg}$, $\boldsymbol{D} = 90\,\boldsymbol{I}_3\,\mathrm{kg/s}$, $\boldsymbol{K} = \boldsymbol{0}_3\,\mathrm{kg/s^2}$. The above parameters are chosen in such a way as to guarantee a desired behavior empirically experimented. The robot should promptly respond to input impulse-like forces by moving in the desired direction, ensuring smoothness without any oscillations and with a damping effect. Nevertheless, the parameters can be easily changed and adapted to modify the behavior depending on the application and the confidence of the operator.

To limit the movement of the tool so as to remain within a safe volume of work, a method based on the application of a FRVF has been proposed. In the following, two geometrically different FRVFs have been explored: conical and linear. Both geometries can be helpful in multiple scenarios. The former can guide the surgeon during a dissection task, preventing extra tissue removal. The latter VF, instead, can be helpful for organ/tissue retraction. In this case, it is more helpful for the doctor to have an attractive VF that reduces the workload to drag the tissue to the desired position. The constraint enforcement method is defined as a spring-damper-like force:

$$\boldsymbol{f}_{VF} = \boldsymbol{K}_{VF}\boldsymbol{d} + \boldsymbol{D}_{VF}\dot{\boldsymbol{d}} , \tag{5.8}$$

where $\boldsymbol{d} = \boldsymbol{p}_t - \boldsymbol{p}_{VF}$, $\boldsymbol{p}_t$ is tool end position ($\boldsymbol{p}_{i+1}$ in (5.2)), $\boldsymbol{p}_{VF}$ is the position on the VF with respect to which the distance is computed, $\boldsymbol{K}_{VF}$ and $\boldsymbol{D}_{VF}$ are constant positive definite diagonal matrices suitably tuned. The force $\boldsymbol{f}_{VF}$ is summed to the input force $\boldsymbol{f}$ of (5.6), so the second order control law will be:

$$\boldsymbol{M}\ddot{\boldsymbol{p}} + \boldsymbol{D}\dot{\boldsymbol{p}} + \boldsymbol{K}\boldsymbol{p} = \boldsymbol{f} - \boldsymbol{f}_{VF} \,. \tag{5.9}$$

Conical VF

To confine the tool movement in a small workspace, the VF has been defined as a circular conical surface of opening angle 2α, with the apex in the trocar point $\boldsymbol{p}_T$, and suitably oriented axis. For convenience, the following measures have been considered to be referred with respect to a trocar frame $\mathcal{F}_T : (O_T - x_T y_T z_T)$, centered in the trocar point $\boldsymbol{p}_T$, and with the axis $\boldsymbol{z}_T$ correspondent to the axis of the cone, coincident with the shaft. Figure 5.1b shows the VF definition.

The conical surface is parametrically described respect to frame $\mathcal{F}_T$ as:

$$\boldsymbol{S}(v, h) = \begin{bmatrix} h\ \tan(\alpha)\cos(v) \\ h\ \tan(\alpha)\sin(v) \\ -h \end{bmatrix} \,, \tag{5.10}$$

with $v \in [0, 2\pi)$ and $h \in [0, H]$. Given the end tool position $\boldsymbol{p}_t$, the point on the VF is computed following the (5.10), where

$$\begin{aligned} h &= -z_t \,, \\ v &= \theta \,, \\ \theta &= \arctan \frac{y_t}{x_t} \,. \end{aligned} \tag{5.11}$$

Differentiating the resulting expression, the following expression is obtained:

$$\dot{\boldsymbol{p}}_{VF} = \begin{bmatrix} \tan(\alpha)\left(z_t \sin\theta\dot{\theta} - \dot{z}_t\cos(\theta)\right) \\ \tan(\alpha)\left(z_t \cos\theta\dot{\theta} + \dot{z}_t\sin(\theta)\right) \\ \dot{z}_t \end{bmatrix} \,. \tag{5.12}$$

Linear VF

If the environment is not too complex, it can be useful to constrain the surgical tool so that it can only move in a certain safe region, where no VF force is applied, divided from the forbidden region by a plane. A frame

$\mathcal{F}_\Pi : (O_\Pi - x_\Pi y_\Pi z_\Pi)$ has been associated to the plane Π, with the axis z_Π orthogonal to the VF plane.

The coordinate of the tool end can be expressed in $\mathcal{F}_\Pi$ as:

$$ {}^{\Pi}\boldsymbol{p}_t = {}^{\Pi}T_b \, {}^{b}\boldsymbol{p}_t \, . \tag{5.13}$$

Given the end tool position ${}^{\Pi}\boldsymbol{p}_t$, the projected point on the plane is computed as:

$$ {}^{\Pi}\boldsymbol{p}_{VF} = \begin{bmatrix} {}^{\Pi}x_t \\ {}^{\Pi}y_t \\ 0 \end{bmatrix} \, , \tag{5.14}$$

obtaining:

$$ {}^{\Pi}\widetilde{\boldsymbol{p}}_{VF} = {}^{\Pi}\boldsymbol{p}_t - {}^{\Pi}\boldsymbol{p}_{VF} = \begin{bmatrix} 0 \\ 0 \\ {}^{\Pi}z_t \end{bmatrix} \, . \tag{5.15}$$

5.3 Experiments

The proposed control framework has been validated with a 7-DOFs Kuka LBR Med 7 robot, dedicated to collaborative applications in medical scenarios. An ATI Force and Torque sensor has been mounted on the flange between the end-effector of the robot and the shaft. The weight of the shaft has been compensated to avoid influencing the robot's motion. The experimental setup is shown in Figure 5.1. The performed experiments aim to show the benefits related to the proposed framework. As the manipulator is hand-guided, the trajectory of the end effector, thus of the tool, is not the same between different experiments. All the considerations made are related to the execution of a specific task.

Section 5.3.1 shows the reduction of the stress on tissues at the trocar point resulting from imposing the RCM constraint in a dissection task. In Section 5.3.2 two experiments are presented to evaluate the effectiveness of the VF enforcement: (i) simulation of a dissection task with and without the constraint enforcement; (ii) evaluation of the magnitude of the VF force when violating the safe workspace determined by the constraint surface. In each experiment, only the quantities in the $x - y$ plane have been considered, as the penetration of the instrument inside the patient's body is allowed as mentioned in Section 5.2.

5.3.1 Stress on the tissue

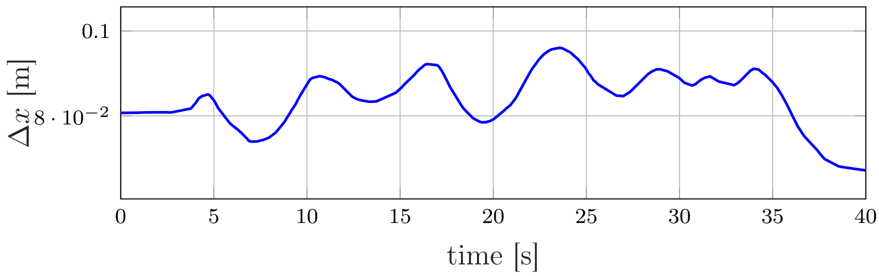

(a) Without the RCM.

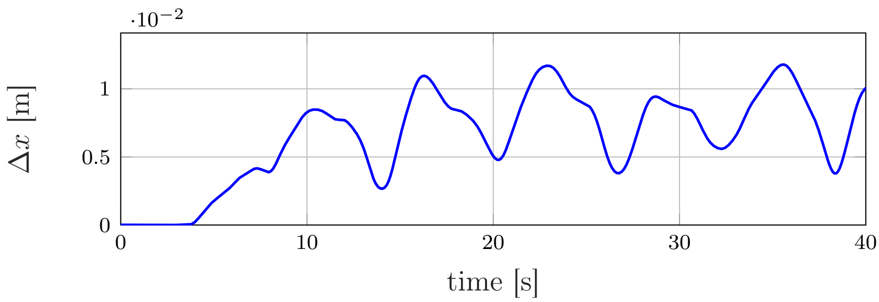

(b) With the RCM.

Figure 5.2. Displacement of trocar point when performing a circular path.

Under the assumption of small displacement and linearity, it can be considered that the stress on tissue at the incision point is proportional to the displacement of the tool at the trocar point, according to Hooke's law. An experiment articulated in two tests is performed to show the stress reduction on tissues at the trocar point imposing the RCM constraint. During each test, the user manually guides the end effector along a circular path with a radius of 3.5 cm. During the first test, the task was performed by simulating a laparoscopic intervention through an incision point without any mechanical or software RCM imposition. On the other hand, the second test is performed while imposing the RCM constraint, following the proposed method.

Figure 5.2a shows the displacement of the trocar point when no constraint is imposed to enforce an RCM to the manipulator kinematics. This can be compared to Figure 5.2b, in which the displacement of the same point is shown when the proposed RCM constraint is imposed. From the data obtained during these two experiments, the mean value of the distance is $\mu = 0.083\,\mathrm{m}$ when there is no constraint enforcement. This value is reduced by one order of magnitude to $\mu = 0.0071\,\mathrm{m}$, with the RCM constraint enforcement. Moreover, in Figure 5.2a the maximum displacement is of $\Delta x = 0.0961\,\mathrm{m}$, which falls to $\Delta x = 0.0128\,\mathrm{m}$ imposing the RCM constraint.

5.3.2 Manual Guidance and Virtual Fixture evaluation

To evaluate the effects of the VF constraint in maintaining the tool in a safe region, two experiments have been performed while still enforcing the RCM.

In the first experiment, the same task examined in Section 5.3.1 of the trocar point is considered. The opening angle α of the conical VF, shown in Figure 5.1b, is chosen to have:

$$\tan(\alpha) = \frac{h}{r} \,, \tag{5.16}$$

where h and r are shown in Fig 5.1b. Figure 5.3a shows the comparison between the performed path with and without the VF enforcement. It can be seen that when the VF is enforced, the tool hardly overcomes the prescribed safe space. To prove that, the length of the paths taken during the tests has been computed. When the VF is not applied the average length of the path computed on four lapses is $0,2354\,\mathrm{m}$, which is reduced to $0,2128\,\mathrm{m}$ when the VF is enforced. However, based on the control structure, the VF does not affect the satisfaction of the RCM constraint, as can be seen in Figure 5.3b and from Table 5.1 where the mean and the standard deviation of the RCM error are reported.

A second experiment has been considered to highlight the effect of the VF force on the performed movements. The task consists of manually moving the tool back and forward, exiting the safe region. The results of this experiment are shown in Figure 5.4. Figure 5.4a shows the applied force during the manual guidance. In Figure 5.4b the VFs force applied

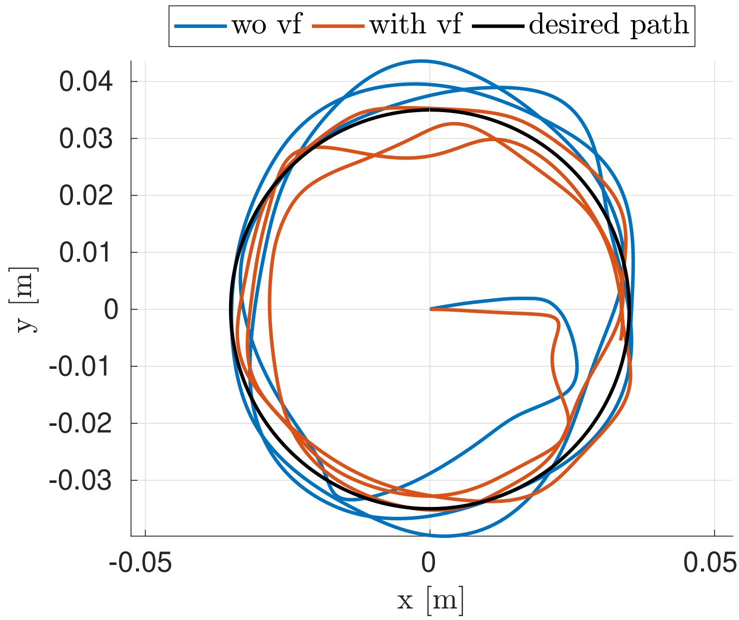

(a) Comparison of the performed path.

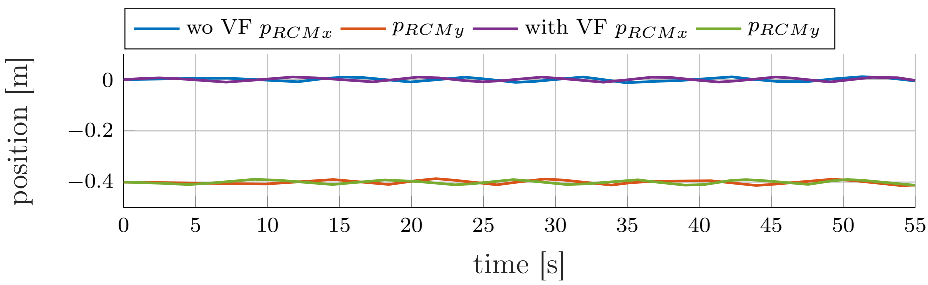

(b) Comparison of the RCM positions.

Figure 5.3. Manual guidance along a circular path with and without the VF.

on the end effector is shown while the manipulator is moved to obtain the distance as in Figure 5.4c. Finally, Figure 5.4d shows the movement of the end-effector during the experiment.

Table 5.1. Mean and standard deviation of RCM error.

	μ_x	μ_y	σ_x	σ_y
WO VF	$6 \cdot 10^{-4}$	$7 \cdot 10^{-4}$	$7.4 \cdot 10^{-3}$	$7.8 \cdot 10^{-3}$
With VF	$-3 \cdot 10^{-4}$	$7 \cdot 10^{-4}$	$7 \cdot 10^{-3}$	$7.2 \cdot 10^{-3}$

5.4 Conclusions

In this work, a human-robot interactive framework with a RCM constraint has been proposed. A constrained kinematic controller has been used to guarantee the exponential convergence of the manual guidance task, with stable satisfaction of the RCM constraint. This approach also has the advantage of requiring minimal knowledge of the trocar geometry and allowing direct control of the penetration of the instruments inside the patient's body. Also, VF are used to restrict the workspace to a safe region and help the surgeon perform a desired path. Application to a dissection task has been proposed to validate the approach.

The results show the effectiveness of constraining the motion at the RCM, as this reduces the stress on the entry point in the patient's body as can be seen in Figure 5.2. The VF enforcement effectively eases the surgeon in following more precisely the path, as shown in Figure 5.3a, and constrains the movement into the safe workspace by applying a force that completely counteracts the one applied by the operator the more the end effector penetrates in the forbidden region as shown in Figure 5.4.

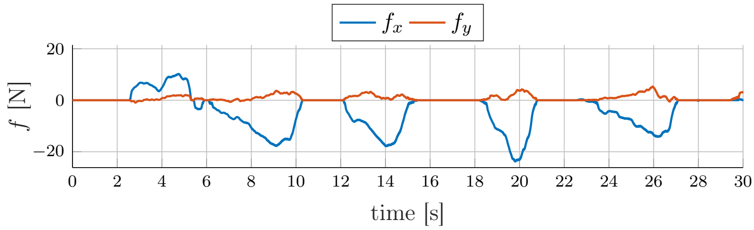

(a) Force measured during the manual guidance.

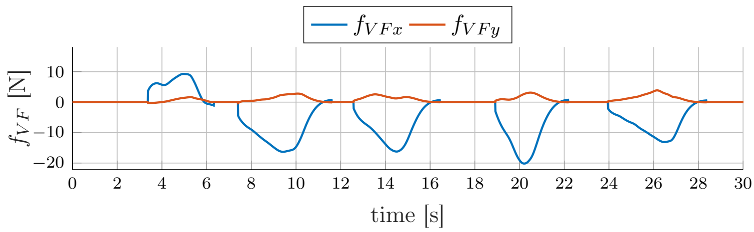

(b) Force exerted by the VF.

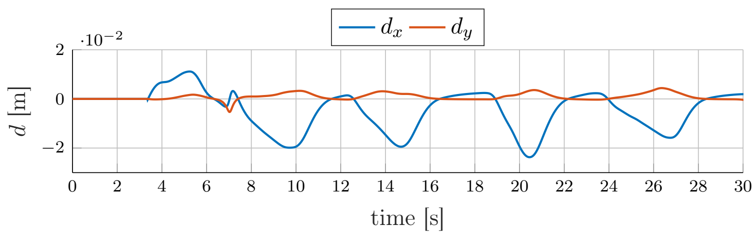

(c) Distance od the manipulator end effector from the VF.

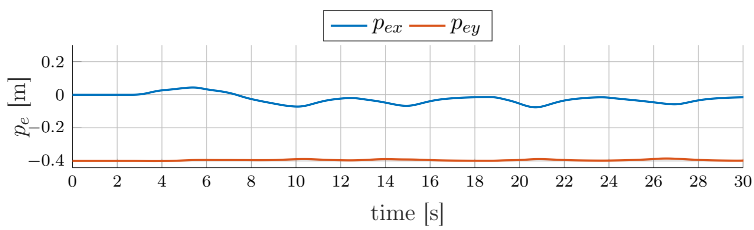

(d) Position of the end-effector in the cartesian space.

Figure 5.4. Analysis of forces when the end-effector crosses the VF.

Chapter 6

Localization of the biliary tract in laparoscopic images

LC is a minimally invasive procedure whereby the gallbladder is removed using laparoscopic techniques. With more than 500,000 cholecystectomies performed per year, great interest has developed in LC. The significant advantages of LC with respect to traditional cholecystectomies are the short hospital stay and early return to regular activity. Morbidity is low, but there is a concern about bile duct injuries. The following chapter introduces and discusses a possible approach to the biliary tract injury clinical problem during LS, explained in Section 6.2. The goal is to detect the biliary tract in white-light images acquired during standard surgical practice. The results are shown in Section 6.3.

6.1 Introduction

One of the most commonly performed surgical procedures in the gastrointestinal field is cholecystectomy. It is mostly performed now using LS when treating cholecystolithiasis, chronic and acute cholecystitis. Since the introduction of the laparoscopic approach, surgeons have focused on preventing complications. The LC approach shows faster recovery and better cosmetic results compared to the traditional approach. However, it carries a higher risk of bile duct injury, which can severely affect the patient's quality of life. To mitigate this risk, some measures have been implemented.

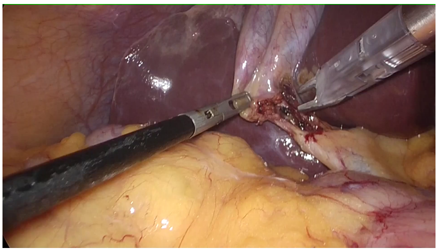

(a) White-light image.

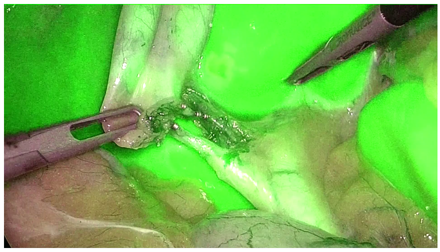

(b) Infra-red light with indocyanine green.

Figure 6.1. Images acquired during cholecystectomy.

One of them implicates the use of near-infrared light for visualization after injecting a fluorescent dye called Indocyanine Green (ICG) to emphasize the bile duct visualization during surgery. This technique enables intraoperative visualization of the bile duct and helps prevent bile duct injury.

The problem in using ICG is that, while enhancing the bile duct, it makes it challenging to see all the other anatomical structures, as can be seen in Figure 6.1 This work aims to address this problem, helping the surgeon better visualize the biliary tract without the use of ICG. To this end, a deep-learning algorithm for the localization of the biliary tract from white-light images acquired during standard surgical practice has been implemented. This work also includes the construction and annotation of an image database to train the deep learning algorithm.

This work proposes a deep learning-based algorithm for localization of the biliary tract during laparoscopic surgical procedures, based on YOLO localization algorithm. A dataset consisting of videos of standard surgical practice has been collected and used to train the deep learning algorithm.

6.2 Methods

While image classification is the process of detecting an object in an image, localization consists of both detecting the presence of the object and its location in the image. This means that the algorithm outputs four more parameters to define the bounding box of the detected object, representing its midpoint coordinates, height and width.

6.2.1 YOLO

The proposed method directly uses laparoscopic images to localize the biliary duct. To this end, YOLO, a state-of-the-art convolutional neural network, has been used [99]. YOLO is a regression-based object detector that looks at the whole image once to perform the detection. It consists of a single CNN that simultaneously predicts bounding boxes and their class probabilities.

YOLO, treats object detection as a regression task, where the detector directly obtains the coordinates of the bounding boxes and the class probabilities from the image pixels. Unlike Recurrent Convolutional Neural Network (R-CNN) or its variants, YOLO examines the image once to predict object presence and location. It learns only global object representations, allowing it to detect objects regardless of their position or whether they are fully or partially visible. Moreover, YOLO can encode contextual information by processing the entire image during training, leading to fewer background errors compared to R-CNN or Fast R-CNN. For enhanced efficiency, YOLO is combined with CNN, exploiting the convolution layer to predict multiple bounding boxes and their class probabilities simultaneously. In addition, YOLO looks at the entire image to encode contextual information during prediction, and thus, it is extremely fast and found suitable to detect or localize objects in real time.

However, YOLO has some limitations. It imposes strict constraints on the bounding box predictions; in fact, each box can only detect one class of objects. Additionally, the algorithm struggles to detect small objects in an image. To address these drawbacks, a new version called YOLOv3 has been introduced.

In this work, the upgraded version of the algorithm, YOLOv3, has been used. It incorporates several improvements to enhance training efficiency and overall performance. These improvements include multi-scale predictions, an improved backbone classifier, and additional features. The backbone network, Darknet-53, is a key enhancement that utilizes residual connections and brings refinements to the bounding box prediction process. It also employs three distinct scales for feature extraction to improve accuracy. YOLOv3 optimizes bounding box predictions by employing dimension clusters as anchor boxes. The model predicts four coordinates for each box and computes an objectivity score for each using logistic regression. In addition, YOLOv3 maintains full image training without negative mining and incorporates multi-scale training, extensive data augmentation, batch normalization, and other standard methodologies. For training and testing, it utilizes the Darknet neural network framework. Historically, YOLO struggled with detecting small objects, but YOLOv3 shows marked improvement in this area, particularly with its multi-scale predictions. Its performance on medium and large objects is comparatively weaker. When comparing accuracy versus speed using the AP50 metric, YOLOv3 demonstrates significant advantages over other detection systems, notably in terms of speed and effectiveness.

For the training phase, the following parameters were used:

- Batch size: 64,
- Learning rate: 0.001,
- Epochs number: 1748,
- Average loss: 0.18.

The Intersection over Union (IoU) was used as evaluation metrics: IoU compares the annotated bounding boxes with the bounding boxes predicted by the network. IoU is an evaluation metric utilized to measure the accuracy of object detectors on specific datasets. Commonly applied to assess the performance of object detection algorithms like HOG + Linear SVM, as well as various convolutional neural network-based detectors (e.g., R-CNN, Faster R-CNN, YOLO), IoU measures the precision of predicted bounding boxes against ground truth data. To effectively use IoU for evaluating any given object detector, two key elements are required:

- Ground truth bounding boxes: These are the manually annotated bounding boxes in the test set that precisely indicate the object's location in an image.
- The bounding boxes provided by our model

With these two sets of bounding boxes at hand, IoU can be implemented. Considering the model-predicted bounding box and the ground truth bounding box, the IoU metric is calculated as the ratio between the area of overlap and the union area of the two. This obtained score serves as a quantitative measure of the model's accuracy in predicting the location and size of objects within an image, with higher scores indicating greater accuracy.

$$IoU = \frac{Area\,of\,Overlap}{Area\,of\,Union} \quad (6.1)$$

Table 6.1. Dataset composition.

	Total Frames	***Training***	***Test***
Patient 1	142	15	15
Patient 2	171	34	14
Patient 3	219	-	39
Patient 4	152	74	20
Patient 5	48	5	5
Patient 6	144	-	29
Patient 7	168	14	10
Patient 8	89	18	10
Patient 9	153	14	10
Patient 10	73	20	10
Patient 11	27	14	10
Patient 12	135	-	19

6.2.2 Dataset

An image dataset has been collected from 12 video clips of 12 different patients who underwent LC during 2020. The videos collected from patients who presented complications that did not fall within the scope of this study were rejected. The videos were acquired through a high-definition endoscopic camera system with a 25 Hz frame rate during surgical endoscopic procedures. The frames extracted from the videos were sampled once every ten frames, obtaining a total of 399 frames. The frames were then manually annotated by drawing a bounding box on the bile duct. The video frames were split into 208 frames for the training set and 191 frames for the test set, as illustrated in Table 6.1. The training set was used to train the neural network, while the test set was used for evaluation purposes only. To avoid overfitting, the frames of three patients out of twelve (Patients 3, 6 and 12) have been used only in the test set.

6.3 Results

The performance of the proposed method was evaluated on the test set. Table 6.2 shows the results of the bile duct detection on each patient. Based on the experimental results, the overall IoU is 0.67.

Table 6.2. Detection Results.

	IoU	***STD***
Patient 1	0.65	0.04
Patient 2	0.70	0.07
Patient 3	0.53	0.02
Patient 4	0.63	0.11
Patient 5	0.73	0.02
Patient 6	0.65	0.04
Patient 7	0.80	0.01
Patient 8	0.63	0.08
Patient 9	0.76	0.02
Patient 10	0.84	0.02
Patient 11	0.65	0.02
Patient 12	0.58	0.04

Regarding the videos that have frames in the training set, the worst-case scenario happened for Patient 4, where the lowest values of the IoU are found. This is probably due to the fact that the ground truth bounding boxes have been annotated manually, and therefore, in some cases, they may be less precise than others, and also because in the video, the biliary tract is not easily distinguishable from the background. However, as can be seen from Figure 6.2, the localization of the surgical site of interest is accurate enough for the aim of the work.

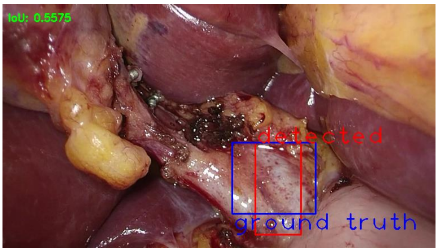

(a) Patient 3.

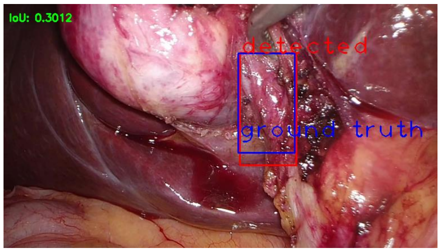

(b) Patient 4.

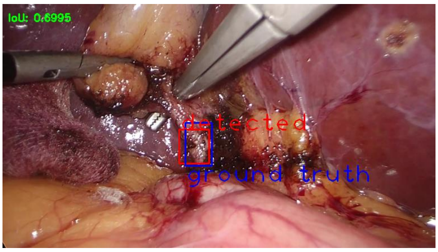

(c) Patient 6.

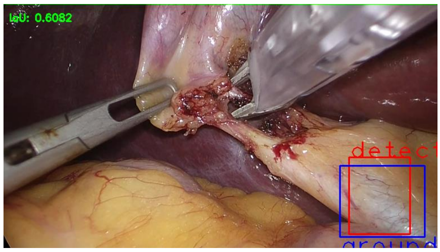

(d) Patient 12.

Figure 6.2. Results of the localization algorithm: Patient 3 in (a), Patient 6 in (c) and Patient 12 in (d) belong only on the test set.

The frames of patients 3, 6 and 12 were used only in the test set. The algorithm recognized the area of interest in 26 of 29 images in video 6 and in 14 of 19 images in video 12. The worst-case scenario happened in video 3, where only 6 of the 39 images were correctly recognized.

6.4 Conclusion

This work addresses the problem of biliary tract injury during LC, using an innovative approach in relation to the work suggested by the literature. The method proposes the application of YOLO for the localization of the biliary tract, creating a dataset of annotated frames of the surgical scene. The average IoU is equal to 67%, despite the small size of the dataset. The future goal is to use the localization of the biliary tract in real-time and implement an augmented reality system in order to help the surgeon correctly and more easily recognize the area of interest in the crucial phases.

Chapter 7

Prisma Dataset

The following chapter presents the Prisma Dataset (MATA), a surgical suture robotics dataset, collected using the dVRK. The chapter is organized as follows: Section 7.2 provides a detailed description of the materials and methods used for data collection and their organization.

7.1 Introduction

The shift from OS to MIRS has resulted in significant improvements in the quality of operations, execution times, and patient rehabilitation times. As discussed in Section 2.1, autonomy is a crucial aspect of robotics in general, as well as surgical robotics, to gain precision, consistency and quality. Although achieving full autonomy for entire surgical procedures is currently unfeasible from a technological viewpoint, it is feasible to automate a smaller portion of surgical procedures by breaking them into smaller tasks [100]. A large part of ongoing research in this field aims to automate tedious and complex tasks, relieving surgeons of their burden [101]. Among the most common surgical procedures, the suturing technique deserves special attention since it is critical, strongly relies on the surgeon's abilities, and remains a tedious, complex, and time-consuming task for surgeons. The importance of the suturing results has been demonstrated through the correlation between the risk of post-surgical complications, including death, and poor surgical technical skill [102]. In fact, surgical technical errors are the primary cause of many post-surgical adverse events, such as re-operation and re-admission [103]. Hence, improving the surgical training method can significantly enhance the safety and effectiveness of surgical patient care. Correctly identifying entry and exit points for the needle is fundamental for the success of the suture and the patient's outcomes. During the suturing procedure, the surgeon has to frequently adjust the orientation of the needle to ensure that it is in the correct pose for needle insertion. The reorientation phase is done through a sequence of grasping, releasing, positioning, and re-grasping operations performed using both robotic arms [104]. Moreover, with the teleoperation of the dVRK, the surgeons do not have the benefit of haptic feedback during the needle insertion and extraction phase of the suturing process. As a result, they have to rely solely on visual cues to compensate for this lack of feedback, which requires a significant amount of training to master. Lastly, viewing the operating field through endoscope images results in a loss of depth perception and adds to the surgeon's workload by presenting additional challenges.

Automation of suturing tasks offers the opportunity to achieve more advanced safety and quality standards through cutting-edge control for specific surgical procedures. This involves various robotics disciplines such as robot control, imaging/sensing, and real-time signal processing, which is linked to Artificial Intelligence (AI) and Machine Learning (ML). Ongoing research uses ML strategies to enable robots to assist surgeons by automating certain time-consuming and elementary tasks and have as a main requirement the access to large datasets to train the ML algorithm. Such datasets allow the robot to learn and replicate complex surgical procedures with unprecedented accuracy. Furthermore, analyzing this data can lead to identifying patterns and techniques that may otherwise be imperceptible to the human eye. Researchers have also been using surgical datasets for skill assessment to evaluate trainee surgeons and improve their training [105].

Teleoperated robots like the dVRK facilitate motor learning by providing access to the operator's hand motion data. This information can be used to analyze gestures, rate technical proficiency, and enhance learning through training augmentation.

Only a few datasets are available in surgical robotics, and JHU-ISI Gesture and Skill Assessment Working Set (JIGSAWS) [106] is one of the best-known and widely used for surgical gesture recognition as it provides a complete kinematic and video dataset labeled. It is also used for studying surgical motion to improve the surgeon's skills. Data in the JIGSAWS are collected with the dVRK from eight surgeons with different expertise levels while they are performing three elementary surgical tasks: Suturing, Needle-Passing, and Knot-Tying, which are very popular and part of surgical training courses. Nevertheless, it is too limited and fragmented: the identified gestures are comparable and do not appear in all of the trials. The performance of the dataset is decreased by the low frequency at which these gestures occur. Other datasets have been subsequently proposed. the UCL dVRK dataset [107] contains 14 videos using the dVRK on five different kinds of animal tissue. For each video frame, an associated image of the virtual tools is produced using a dVRK simulator. Furthermore, the Robotic Surgical Maneuvers (ROSMA) dataset has been collected using the dVRK containing 36 kinematic variables, divided into 154-dimensional data, recorded at 50 Hz for 206 trials of three common training surgical tasks [108].

Nevertheless, each surgical gesture is defined not only from kinematic values but also from specific muscular activation. Electromyography plays a crucial role in the Human-Machine Interface field [109], and it brings many features that can be extracted to improve the current state-of-art of robotic surgery. In fact, during laparoscopic suturing maneuvers, surgeons with varying levels of technical expertise reveal differences in limb positions. By placing sensors directly on the surgeon, human motion and intention can be assessed from the surgeon's perspective. Analyzing in which part of the task there is greater muscle effort or what the optimal angle of the grip of the needle to perform a good suture operation can provide new information on the efficient acquisition of technical skills and the reduction of physical stress during laparoscopic surgery [110].

For these reasons, this work presents the design and evaluation of a novel suturing gesture dataset, the MATA. The dataset is made by the data collected from seven surgeons with different skill levels who performed the suturing task on the dVRK. In particular, the dataset encompasses a comprehensive set of data, including kinematics, video footage, interaction force, electromyographic signals, acceleration metrics, angles, and angular velocity related to the surgeon's right wrist. Additionally, it provides annotations for surgical gestures and the results of a post-trial questionnaire administered to assess surgeons' quality and the required levels of physical and mental effort during the task.

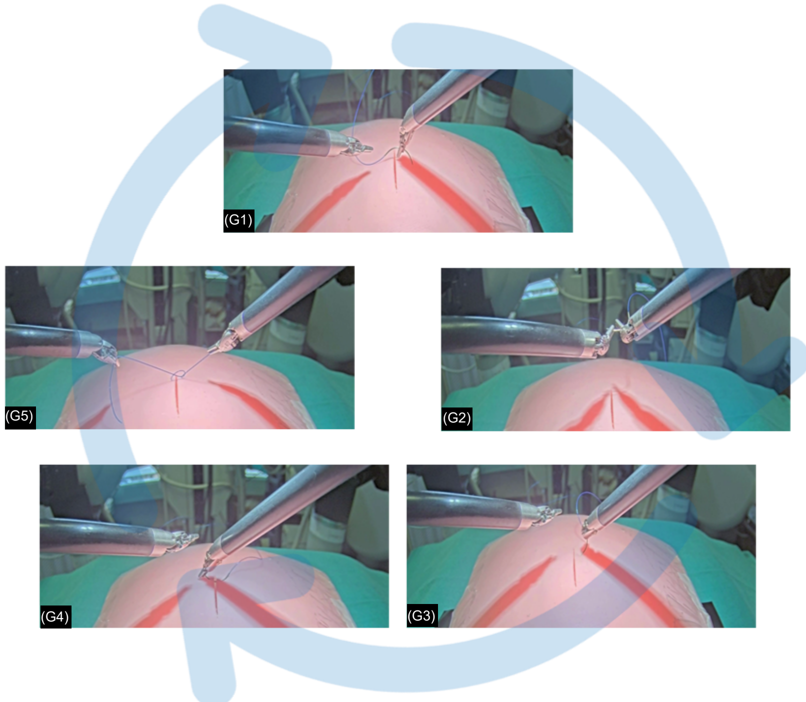

Figure 7.1. Suturing Task Gesture: (G1) Needle Grasping; (G2) Gripper Reconfiguration; (G3) Needle Insertion; (G4) Needle Extraction; (G5) Knot–Tying.

7.2 The MATA dataset

7.2.1 Suture Taxonomy

When creating a surgical dataset, one of the main challenges is using a language that accurately describes the surgeon's activities. Surgical procedures can be described at varying levels of detail, similar to how natural language can be used at different levels of granularity, namely the level of abstraction for describing the surgical process. The granularity determines at which level of detail the surgical procedure is modeled. However, there is no universal taxonomy or vocabulary to define the differences between granularity levels. Following the definition given in [111, 112], the surgical workflow can be modelled at different levels: (i) dexemes, (ii) surgemes, (iii) activities, (iv) steps, (v) phases, (vi) procedure, (vii) state.

The most detailed level for observing the surgical workflow is through *dexemes*. These are short gestures without any medical relevance made by the surgeon using one hand. A sequence of *dexemes* is called a *surgeme*, which represents a specific surgical gesture performed for a particular purpose, for example, knot-tying. An *activity* refers to the physical action described by the surgical tool, the anatomical structure it is used on, and the action performed. A *step* is a set of *activities* done towards a surgical objective. A *phase* is a longer period that includes several steps and may involve interactions with other members of the surgical team. Finally, a *procedure* refers to the entire surgery, starting from the first incision and ending with the last stitch that closes the patient.

Segmentation at different levels highlights distinct aspects of the surgical procedure, leading to a range of applications. On one side, Maktabi et al. [113] demonstrate that a high-level situation awareness is better for workflow optimization, scheduling and resource management. On the other side, low-level analysis better describes atomic actions or motion patterns [114].

The MATA divides the suturing task into five surgemes shown in Figure 7.1:

(G1) Needle Grasping: The subject picks up the needle;

(G2) Grasping Reconfiguration: The subject adjusts the needle grasping pose, passing the needle between the two instruments;

(G3) Needle Insertion: The subject inserts the needle into the tissue, entering at the dot marked on one side of the incision and exiting at the corresponding dot marked on the other side of the incision;

(G4) Needle Extraction: The subject extracts the needle out of the tissue;

(G5) Knot-Tying: The subject ties the knot securing the single point of the suture.

Gesture Index	Gesture Description
G1	Needle Grasping
G2	Gripper Reconfiguration
G3	Needle Insertion
G4	Needle Extraction
G5	Knot-Tying

Table 7.1. Gesture vocabulary.

(a) Wireless Electromyography (EMG) sensors. **(b)** Inertial Measurement Unit (IMU) sensor.

Figure 7.2. External sensors.

From here and in the following of this chapter, the terms surgemes and gestures will be used to identify the same set reported in Table 7.1. Gesture recognition through surgemes classification allows working with short motion segments that are less complex and easier to generalize and can be treated singularly or composed modularly to define long-term goals or in surgical automation [115]. In addition, this makes segmentation and gesture classification easier in real time.

7.2.2 Data Collection

The MATA focuses on single-point suture: the needle passes through one side of the wound, penetrating the outer and underlying layers, and exits on the opposite side. Each stitch in the broken suture is secured individually by tying and cutting.

The setup is composed as follows:

dVRK allows direct recording video, kinematic, dynamic, and foot pedal information from both the surgeon and patient side;

External Camera is used to capture video from a different point-of-view and in higher quality;

Wireless Electromyography (EMG) Sensors , Freeemg 1000 from BTS Bioengineering, positioned on the flexor and extensor Carpi Radialis Longus of the left and right arm, allow the computation of the electrical activities of the aforementioned muscles,

Inertial Measurement Unit (IMU) Sensor , placed on the wrist of the main surgeon's skilled arm, measures the acceleration, rotation speed and angles of the wrist with respect to a reference system;

Questionaires : compiled by the surgeons at the end of the trial to gauge the physical and mental effort.

During the data collection procedure, each subject followed the steps listed below:

1. the EMG sensors are placed on the surgeon and the Maximum Voluntary Contraction (MVC) of the flexor and extensor Carpi Radialis Longus are registered to normalize the muscular activity;

2. Place the IMU Sensor;

3. The surgeon starts the task and all the data are recorded and synchronized with a global time. Each surgeon repeats the task twice;

4. At the end, the surgeon completes the questionnaire to register the mental and physical stress.

The task consists of a single-point suture performed on a medical phantom using the dVRK. During each trial, the subject performed the task twice. The surgeon is asked to announce the beginning of each gesture during the execution of the suture to automatically label the data, following Table 7.1.

Col. Indices	N. of Variables	Description of Variables
1-24	24	ECM Body Jacobian
25-48	24	ECM Space Jacobian
49-54	6	ECM Body Wrench
55-60	6	ECM Spacial Wrench
61-66	6	ECM Cartesian Pose
67-108	42	Left MTM Body Jacobian
109-114	6	Left MTM Body Wrench
115-120	6	Left MTM Local Cartesian Pose
121-126	6	Left MTM Cartesian Pose
127-132	6	Left MTM Velocity
133-174	42	Left MTM Space Jacobian
175-180	6	Left MTM Spacial Wrench
181-294	114	Right MTM Kinematics
295-330	36	PSM1 Body Jacobian
331-336	6	PSM1 Body Wrench
337-342	6	PSM1 Local Cartesian Pose
343-348	6	PSM1 Cartesian Pose
349-354	6	PSM1 Velocity
355-390	36	PSM1 Space Jacobian
391-396	6	PSM1 Spatial Wrench
397-498	102	PSM2 Kinematics
498-503	6	Interaction Force
504	1	Footpedal Camera
505	1	Footpedal Clutch
506	1	Footpedal Coag
507	1	Teleoperation Scale
508-513	6	MTMR\PSM1 alignment
514-519	6	MTMR\PSM1 following
520-525	6	MTML\PSM2 alignment
526-531	6	MTML\PSM2 following
532-535	4	EMG
536-542	7	User Data
-	-	Video ECM Right
-	-	Video ECM Left
-	-	Video External Camera

Table 7.2. MATA Data Variables.

7.2.3 Data Description

The MATA includes data from seven subjects, indexed from A to G. The hour-of-practice on the robot classifies them into three levels of robotic surgical expertise: Expert (E), more than 100 hours of practice; Intermediate (I), between 100 hours and 10 hours of practice; Novice (N), less than 10 hours of practice. In detail, subjects from A to E are classified as Expert, while subjects F and G are Novice. From each of them, the data collected are listed in Table 7.2 and organized in folders as follows:

- ***Kinematics***: includes data captured at 100 Hz from MTMs, PSMs, ECM. The motion was described using 33 kinematic variables to describe the kinematics for all five manipulators listed above. For each manipulator, the variables include Cartesian pose, linear and angular velocities and Body and Space Jacobian;

- ***dVRK Data***: encompasses pedal and console variables, along with SUJ variables, where the pedalboard includes *Coag* and *Clutch* pedals, with boolean variables indicating their status;

- ***Videos***: includes the three video files captured from endoscopic and external cameras;

- ***Force***: comprises six variables of interaction force calculated with the residue theory [116] and already tested on the dVRK [62, 117] and presented in Chapters 3 and 4;

- ***EMG Signals***: contains electromyographic signal values captured at 1000 Hz during the trial, including EMG values of maximum contraction;

- ***IMU* Sensor**: includes xyz components of acceleration, angular velocity, and angles of the right wrist, captured at 100Hz with the IMU sensor;

- ***Transcriptions***: contains gesture annotations with the gesture name and corresponding start and end frames, synchronized using a common global time;

- ***User Suturing***: contains a text file detailing the competence level (E, I, N) of each surgeon and questionnaire results, providing scores on mental demand, physical demand, temporal demand, effort, frustration level, and performance rated from 1 to 10.

In Table 7.2, the Column Indices and the Number of Variables related to the Video are omitted due to potential changes in this information during post-processing. A unique identifier has been assigned to each test in the form of "$SuturingS_{id}Rep$", where $\mathrm{S_{id}}$ is the letter identifying the surgeon and Rep is the repetition number.

7.3 Conclusions

Nowadays, research can benefit a lot from creating new datasets, which can improve those currently present in the literature. The work presented in this chapter is intertwined in this perspective. Thanks to the collaboration of surgeons with different levels of experience, a set of suturing data has been collected and organized to form a dataset that is a valid alternative to the one most used today, the JIGSAWS. The suturing task has been divided by identifying five different gestures: the needle grasping, the reconfiguration of the needle aimed at getting the right angle with respect to the wound, the needle in the tissue, the extraction of the needle from the opposite point of the wound and finally the knot. The data collected in the dataset are labeled from 1 to 5 to identify each gesture. The dataset comprises 14 single-point suture trials and a large number of parameters with respect to the JIGSAWS dataset. Moreover, the dataset comprises EMG sensors and IMU sensors data collected from the surgeon's wrist that can be significant in future works aimed at identifying gestures and considering the effort of the surgeon. The dataset can also be used to improve the skills of surgeons or train new recruits. At the end of the tests, a questionnaire has been administered to the surgeon to evaluate his physical and mental effort as well as their performance.

Chapter 8

Conclusions

This thesis had the objective to address the limitations of current surgical robotics procedures. Commercially available teleoperated robots have improved classical surgical practice by reducing the invasiveness, tremors and hospital stay enhancing precision, accuracy, and the whole surgeon experience. Still, there are some limitations that can be overcome by incrementing the autonomy capabilies of surgical robots. This theme encompasses different fields connected to robotics comprising modeling, control, vision, haptics and AI.

After an introduction to surgical robotics, the contribution of the thesis has been presented. A review of the state-of-the-art methods for the topic discussed in the thesis is given in Chapter 2, relating the various topics with the autonomy levels they allow in surgical robotics. Advanced model-based control algorithms need accurate knowledge of the robot's kinematics and dynamics to obtain robust behavior in such an unpredictable environment as the surgical context. Chapter 3 proposes a novel dynamic model of the PSM of the dVRK. The tests performed, and the confrontations with other models present in the literature demonstrate the model's validity.

Scientific contributions present in Chapter 5 and 4 concern assistive methods based on haptic-guided shared control applications surgical procedures. The first work is presented in Chapter 5 and presents a human-robot interface that enables robots like the Kuka Med to respect the RCM constraint required for MIRS. Moreover, a shared control technique, namely the application of VF, in an impedance control framework has been considered to constrain the robot in a certain safe region. In particular, a conical safe region is considered tested in a manually guided modality where the operator moves the robot along a circular trajectory. The tests prove that the application of the VF helps the surgeon avoid the dangerous area while still maintaining the RCM constraint.

The second work presented in Chapter 4 uses haptic cues and FRVF to avoid collisions between tools. This is an influential topic in surgical robotics research, particularly in MIRS, since surgeons do not have a complete vision of the surgical site and instruments work very close to each other. Haptic cues have been demonstrated to be a valid tool to release part of the surgeon's mental workload and help in the execution of some tasks. In this work, the tool position is estimated through vision without the use of markers and the already available kinematical data have been integrated with the vision-based positions in order to avoid errors by adopting an EKF. The whole framework has been tested on an extensive user study with surgeons that showed the effectiveness of the control method on novice surgeons.

An important factor of 4 is the utilization of the vision as a fundamental perception source. Vision perception is indeed critical in surgical robotics since the surgeon only relies on that information. Chapter 6 focuses on an application of an advanced image localization technique that is YOLO and implemented it for the localization of the bile duct in LC. Raw images have been collected and manually annotated in collaboration with clinicians to localize the biliary tract in white-light images with the aim of avoiding the use of infra-red visualization and ICG.

Lastly, Chapter 7 presents a novel dataset that collects robotics and electromyographic data from surgeons performing a single-point suture procedure. The dataset is of paramount importance since it opens the way for the training AI-based algorithm that can help in different ways the surgeon experience: from training assistance to task recognition to enhance the surgical workflow, to the automation of specific subtasks, to the surgeon's performance assessing.

Bibliography

[1] M. J. Mack, "Minimally invasive and robotic surgery," *Jama*, vol. 285, no. 5, pp. 568–572, 2001.

[2] A. Kumar, N. Yadav, S. Singh, and N. Chauhan, "Minimally invasive (endoscopic-computer assisted) surgery: Technique and review," *Annals of maxillofacial surgery*, vol. 6, no. 2, p. 159, 2016.

[3] A. F. Mavrogenis, K. Markatos, T. Saranteas, I. Ignatiadis, S. Spyridonos, M. Bumbasirevic, A. V. Georgescu, A. Beris, and P. N. Soucacos, "The history of microsurgery," *European Journal of Orthopaedic Surgery & Traumatology*, vol. 29, pp. 247–254, 2019.

[4] R. Bittner, "Laparoscopic surgery—15 years after clinical introduction," *World journal of surgery*, vol. 30, pp. 1190–1203, 2006.

[5] F. Ficuciello, G. Tamburrini, A. Arezzo, L. Villani, and B. Siciliano, "Autonomy in surgical robots and its meaningful human control," *Paladyn, Journal of Behavioral Robotics*, vol. 10, no. 1, pp. 30–43, 2019. [Online]. Available: https://doi.org/10.1515/pjbr-2019-0002

[6] A. Gözen, T. Tokas, A. Tschada, A. Jalal, J. Klein, and J. Rassweiler, "Comparison of operating positions and ethos surgical platform for laparoscopic pelvic surgery simulation," *J Endourol*, vol. 29, pp. 95–99, 2015.

[7] J. J. Rassweiler and D. Teber, "Advances in laparoscopic surgery in urology," *Nature Reviews Urology*, vol. 13, no. 7, pp. 387–399, 2016.

[8] B. S. Peters, P. R. Armijo, C. Krause, S. A. Choudhury, and D. Oleynikov, "Review of emerging surgical robotic technology," *Surgical endoscopy*, vol. 32, pp. 1636–1655, 2018.

[9] A. Hussain, A. Malik, M. U. Halim, and A. M. Ali, "The use of robotics in surgery: a review," *International journal of clinical practice*, vol. 68, no. 11, pp. 1376–1382, 2014.

[10] D. Oleynikov, "Robotic surgery," *Surgical Clinics of North America*, vol. 88, no. 5, pp. 1121–1130, 2008, advances and Controversies in Minimally Invasive Surgery. [Online]. Available: https://www.sciencedirect.com/science/article/pii/S0039610908000832

[11] Intuitive, "Sustainability report 2021," Intuitive corp. 2021, Tech. Rep., 2022.

[12] A. Simorov, R. S. Otte, C. M. Kopietz, and D. Oleynikov, "Review of surgical robotics user interface: what is the best way to control robotic surgery?" *Surgical endoscopy*, vol. 26, pp. 2117–2125, 2012.

[13] B. Siciliano, O. Khatib, and T. Kröger, *Springer handbook of robotics*. Springer, 2008, vol. 200.

[14] A. Attanasio, B. Scaglioni, E. De Momi, P. Fiorini, and P. Valdastri, "Autonomy in surgical robotics," *Annual Review of Control, Robotics, and Autonomous Systems*, vol. 4, pp. 651–679, 2021.

[15] G.-Z. Yang, J. Cambias, K. Cleary, E. Daimler, J. Drake, P. E. Dupont, N. Hata, P. Kazanzides, S. Martel, R. V. Patel *et al.*, "Medical robotics—regulatory, ethical, and legal considerations for increasing levels of autonomy," p. eaam8638, 2017.

[16] D. Bouget, M. Allan, D. Stoyanov, and P. Jannin, "Vision-based and marker-less surgical tool detection and tracking: a review of the literature," *Medical Image Analysis*, vol. 35, pp. 633–654, 2017.

[17] S. Bodenstedt *et al.*, "Comparative evaluation of instrument segmentation and tracking methods in minimally invasive surgery," *Medical Image Analysis*, 2018.

[18] S. Allan, M. Thompson, M. J. Clarkson, S. Ourselin, D. J. Hawkes, J. Kelly, and D. Stoyanov, "2D-3D Pose Tracking of Rigid Instruments in Minimally Ivasive Surgery," *Information Processing in Computer-Assisted Interventions*, vol. 8498, pp. 1–10, 2014.

[19] X. Du, M. Allan, A. Dore, S. Ourselin, D. Hawkes, J. D. Kelly, and D. Stoyanov, "Combined 2D and 3D tracking of surgical instruments for minimally invasive and robotic-assisted surgery," *International Journal of Computer Assisted Radiology and Surgery*, vol. 11, no. 6, pp. 1109–1119, 2016.

[20] X. Du, T. Kurmann, P.-L. Chang, S. Allan, M. Ourseln, R. Sznitman, J. D. Kelly, and D. Stoyanov, "Articulated Multi-Instrument 2-d Pose Estimation Using Fully Convolutional Networks," *IEEE Transaction on Medical Imaging*, vol. 37, no. 5, pp. 1276–1287, 2018.

[21] H. Sang, J. Yun, R. Monfaredi, E. Wilson, H. Fooladi, and K. Cleary, "External force estimation and implementation in robotically assisted minimally invasive surgery," *The International Journal of Medical Robotics and Computer Assited Surgery*, vol. 13, no. 2, p. e1824, 2017.

[22] F. Piqué, M. N. Boushaki, M. Brancadoro, E. De Momi, and A. Menciassi, "Dynamic modeling of the da vinci research kit arm for the estimation of interaction wrench," *Proc. IEEE International Symposium on Medical Robotics*, pp. 1–7, 2019.

[23] L. B. Rosenberg, "Virtual fixtures: Perceptual tools for telerobotic manipulation," *Proc. IEEE Virtual Reality Annual International Symposium*, pp. 76–82, 1993.

[24] S. A. Bowyer, B. L. Davies, and F. R. y Baena, "Active constraints/virtual fixtures: A survey," *IEEE Transactions on Robotics*, vol. 30, no. 1, pp. 138–157, 2013.

[25] N. Enayati, E. De Momi, and G. Ferrigno, "Haptics in robot-assisted surgery: Challenges and benefits," *IEEE reviews in biomedical engineering*, vol. 9, pp. 49–65, 2016.

[26] M. Selvaggio, G. A. Fontanelli, F. Ficuciello, L. Villani, and B. Siciliano, "Passive Virtual Fixtures adaptation in minimally invasive robotic surgery," *IEEE Robotics and Automation Letters*, vol. 3, no. 4, pp. 3129–3136, 2018.

[27] Z. Chen, A. Malpani, P. Chalasani, A. Deguet, S. S. Vedula, P. Kazanzides, and R. H. Taylor, "Virtual fixture assistance for needle passing and knot tying," in *2016 IEEE/RSJ International Conference on Intelligent Robots and Systems (IROS)*, 2016, pp. 2343–2350.

[28] R. Moccia, M. Selvaggio, L. Villani, B. Siciliano, and F. Ficuciello, "Vision-based Virtual Fixtures Generation for Robotic-Assisted Polyp Dissection Procedures," *Proc. IEEE International Conference on Intelligent Robots and Systems*, 2019.

[29] M. Li, M. Ishii, and R. H. Taylor, "Spatial Motion Constraints Using Virtual Fixtures Generated by Anatomy," *IEEE Transaction on Robotics*, vol. 23, no. 1, pp. 4–19, 2007.

[30] J. Ren, R. V. Patel, K. A. McIsaac, G. Guiraudon, and T. M. Peters, "Dynamic 3-D Virtual Fixtures for Minimally Invasive Beating Heart Procedures," *IEEE Transactions on Medical Imaging*, vol. 27, no. 8, pp. 1061–1070, 2008.

[31] T. Xia, C. Baird, G. Jallo *et al.*, "An integrated system for planning, navigation and robotic assistance for skull base surgery," *International Journal of Medical Robot*, vol. 4, no. 4, pp. 321–330, 2008.

[32] F. Rydén and H. J. Chizeck, "Forbidden-region virtual fixtures from streaming point clouds: Remotely touching and protecting a beating heart," *Proc. IEEE/RSJ International Conference on Intelligent Robots and Systems*, pp. 3308–3313, 2012.

[33] K.-W. Kwok, G. P. Mylonas, L. W. Sun, M. Lerotic, J. Clark, T. Athanasiou, A. Darzi, and G.-Z. Yang, "Dynamic active constraints for hyper-redundant flexible robots," in *International Conference on Medical Image Computing and Computer-Assisted Intervention.* Springer, 2009, pp. 410–417.

[34] N. V. Navkar, Z. Deng, D. J. Shah, K. E. Bekris, and N. V. Tsekos, "Visual and force-feedback guidance for robot-assisted interventions in the beating heart with real-time mri," in *2012 IEEE International Conference on Robotics and Automation*, 2012, pp. 689–694.

[35] T. L. Gibo, L. N. Verner, D. D. Yuh, and A. M. Okamura, "Design considerations and human-machine performance of moving virtual fixtures," in *2009 IEEE International Conference on Robotics and Automation.* IEEE, 2009, pp. 671–676.

[36] M. M. Marinho, B. V. Adorno, K. Harada, and M. Mitsuishi, "Active constraints using vector field inequalities for surgical robots," in *2018 IEEE International Conference on Robotics and Automation (ICRA).* IEEE, 2018, pp. 5364–5371.

[37] ——, "Dynamic active constraints for surgical robots using vector-field inequalities," *IEEE Transactions on Robotics*, vol. 35, no. 5, pp. 1166–1185, 2019.

[38] A. Banach, K. Leibrandt, M. Grammatikopoulou, and G.-Z. Yang, "Active contraints for tool-shaft collision avoidance in minimally invasive surgery," in *2019 International Conference on Robotics and Automation (ICRA).* IEEE, 2019, pp. 1556–1562.

[39] R. H. Taylor and P. Kazanzides, "Medical robotics and computer-integrated interventional medicine," in *Biomedical Information Technology.* Elsevier, 2008, pp. 393–416.

[40] R. H. Taylor, A. Menciassi, G. Fichtinger, P. Fiorini, and P. Dario, "Medical robotics and computer-integrated surgery," in *Springer handbook of robotics*. Springer, 2016, pp. 1657–1684.

[41] C.-H. Kuo and J. S. Dai, "Robotics for minimally invasive surgery: a historical review from the perspective of kinematics," in *International symposium on history of machines and mechanisms*. Springer, 2009, pp. 337–354.

[42] T. Ortmaier and G. Hirzinger, "Cartesian control issues for minimally invasive robot surgery," in *Proceedings. 2000 IEEE/RSJ International Conference on Intelligent Robots and Systems (IROS 2000)(Cat. No. 00CH37113)*, vol. 1. IEEE, 2000, pp. 565–571.

[43] P. J. From, "On the kinematics of robotic-assisted minimally invasive surgery," *Modeling, Identification and Control Journal*, 2013.

[44] J. Sandoval, G. Poisson, and P. Vieyres, "Improved dynamic formulation for decoupled cartesian admittance control and rcm constraint," in *IEEE International Conference on Robotics and Automation (ICRA)*. IEEE, 2016, pp. 1124–1129.

[45] H. Su, G. Ferrigno, E. De Momi *et al.*, "Adaptive decoupling control of a serial redundant robot for teleoperated minimally invasive surgery," in *IEEE ICRA Workshop on Supervised Autonomy in Surgical Robotics*, 2018, pp. 1–6.

[46] N. Aghakhani, M. Geravand, N. Shahriari, M. Vendittelli, and G. Oriolo, "Task control with remote center of motion constraint for minimally invasive robotic surgery," in *IEEE Int. Conf. on Robotics and Automation*, 2013, pp. 5807–5812.

[47] H. Azimian, R. V. Patel, and M. D. Naish, "On constrained manipulation in robotics-assisted minimally invasive surgery," in *2010 3rd IEEE RAS EMBS Int. Conf. on Biomedical Robotics and Biomechatronics*, 2010, pp. 650–655.

[48] B. van Amsterdam, M. J. Clarkson, and D. Stoyanov, "Gesture recognition in robotic surgery: A review," *IEEE Transactions on Biomedical Engineering*, vol. 68, no. 6, pp. 2021–2035, 2021.

[49] A. Esteva, K. Chou, S. Yeung, N. Naik, A. Madani, A. Mottaghi, Y. Liu, E. Topol, J. Dean, and R. Socher, "Deep learning-enabled medical computer vision," *NPJ digital medicine*, vol. 4, no. 1, p. 5, 2021.

[50] J. Peng, Q. Chen, L. Kang, H. Jie, and Y. Han, "Autonomous recognition of multiple surgical instruments tips based on arrow obb-yolo network,"

IEEE Transactions on Instrumentation and Measurement, vol. 71, pp. 1–13, 2022.

[51] Z. Li, M. Dong, S. Wen, X. Hu, P. Zhou, and Z. Zeng, "Clu-cnns: Object detection for medical images," *Neurocomputing*, vol. 350, pp. 53–59, 2019.

[52] B. Tian, L. Li, Y. Qu, and L. Yan, "Video object detection for tractability with deep learning method," in *2017 Fifth International Conference on Advanced Cloud and Big Data (CBD)*, 2017, pp. 397–401.

[53] T. Chheda, R. Iyer, S. Koppaka, and D. Kalbande, "Gastrointestinal tract anomaly detection from endoscopic videos using object detection approach," in *Advances in Visual Computing: 15th International Symposium, ISVC 2020, San Diego, CA, USA, October 5–7, 2020, Proceedings, Part II 15*. Springer, 2020, pp. 494–505.

[54] Y. I. Cho and M. Doniyorjon, "Wireless endoscopic image detection using yolo-inception-res-a," in *2022 13th International Conference on Information and Communication Technology Convergence (ICTC)*, 2022, pp. 751–753.

[55] R. Qureshi, M. G. RAGAB, S. J. ABDULKADER, A. ALQUSHAIB, E. H. SUMIEA, H. Alhussian *et al.*, "A comprehensive systematic review of yolo for medical object detection (2018 to 2023)," *Authorea Preprints*, 2023.

[56] da Vinci Research Kit wiki community, [Online]. [Online]. Available: http://research.intusurg.com/dvrkwiki/

[57] J. H. U. D. controller git repositories, [Online]. Available: https://github.com/jhu-dvrk. [Online]. Available: http://research.intusurg.com/dvrkwiki/

[58] P. Kazanzides, Z. Chen, A. Deguet, G. S. Fischer, R. H. Taylor, and S. P. DiMaio, "An open-source research kit for the da vinci surgical system," in *IEEE Intl. Conf. on Robotics and Auto. (ICRA)*, Hong Kong, China, 2014, pp. 6434–6439.

[59] ——, "An open-source research kit for the da Vinci®Surgical System," *Proc. IEEE International Conference on Robotics and Automation*, pp. 6434–6439, 2014.

[60] M. Ferro, A. Mirante, F. Ficuciello, and M. Vendittelli, "A coppeliasim dynamic simulator for the da vinci research kit," *IEEE Robotics and Automation Letters*, vol. 8, no. 1, pp. 129–136, 2022.

[61] C. D'Ettorre, A. Mariani, A. Stilli, F. Rodriguez y Baena, P. Valdastri, A. Deguet, P. Kazanzides, R. H. Taylor, G. S. Fischer, S. P. DiMaio, A. Menciassi, and D. Stoyanov, "Accelerating surgical robotics research: A review of 10 years with the da vinci research kit," *IEEE Robotics and Automation Magazine*, vol. 28, no. 4, p. 56–78, Dec 2021.

[62] R. Moccia, C. Iacono, B. Siciliano, and F. Ficuciello, "Vision-based dynamic virtual fixtures for tools collision avoidance in robotic surgery," *IEEE Robotics and Automation Letters*, vol. 5, no. 2, pp. 1650–1655, 2020.

[63] R. Moccia and F. Ficuciello, "Autonomous endoscope control algorithm with visibility and joint limits avoidance constraints for da vinci research kit robot," in *2023 IEEE International Conference on Robotics and Automation (ICRA)*. IEEE, 2023, pp. 776–781.

[64] G. A. Fontanelli, F. Ficuciello, L. Villani, and B. Siciliano, "Modelling and identification of the da Vinci Research Kit robotic arms," *Proc. IEEE/RSJ International Conference on Intelligent Robots and Systems*, pp. 1464–1469, 2017.

[65] Y. Wang, R. Gondokaryono, A. Munawar, and G. S. Fischer, "A convex optimization-based dynamic model identification package for the da vinci research kit," *IEEE Robotics and Automation Letters*, vol. 4, no. 4, pp. 3657–3664, 2019.

[66] B. Siciliano, L. Sciavicco, L. Villani, and G. Oriolo, *Robotics: Modelling, Planning and Control*. New York, NY, USA: Springer-Verlag, 2009.

[67] G. A. Fontanelli, F. Ficuciello, L. Villani, and B. Siciliano, "Modelling and identification of the da vinci research kit robotic arms," in *2017 IEEE/RSJ International Conference on Intelligent Robots and Systems (IROS)*, Sep. 2017, pp. 1464–1469.

[68] F. Shao and F. Ficuciello, "Dynamic parameter identification of the kuka lbr med robot," in *2023 IEEE 19th International Conference on Automation Science and Engineering (CASE)*, 2023, pp. 1–6.

[69] F. Ficuciello, G. Tamburrini, A. Arezzo, L. Villani, and B. Siciliano, "Autonomy in surgical robots and its meaningful human control. paladyn j behav robot 10: 30–43," 2019.

[70] G. A. Fontanelli, L. R. Buonocore, F. Ficuciello, L. Villani, and B. Siciliano, "An external force sensing system for minimally invasive robotic surgery," *IEEE/ASME Transactions on Mechatronics*, vol. 25, no. 3, pp. 1543–1554, 2020.

[71] C. Sousa and R. Cortesão, "Physical feasibility of robot base inertial parameter identification: A linear matrix inequality approach," *The International Journal of Robotics Research*, vol. 33, no. 6, pp. 931–944, 2014.

[72] K. Sedlaczek and P. Eberhard, "Using augmented lagrangian particle swarm optimization for constrained problems in engineering," *Structural and Multidisciplinary Optimization*, vol. 32, no. 4, pp. 277–286, 2006.

[73] B. Armstrong-Hélouvry, P. Dupont, and C. C. De Wit, "A survey of models, analysis tools and compensation methods for the control of machines with friction," *Automatica*, vol. 30, no. 7, pp. 1083–1138, 1994.

[74] M. Gautier, "Numerical calculation of the base inertial parameters of robots," *Journal of robotic systems*, vol. 8, no. 4, pp. 485–506, 1991.

[75] C. Gaz, M. Cognetti, A. Oliva, P. R. Giordano, and A. De Luca, "Dynamic identification of the franka emika panda robot with retrieval of feasible parameters using penalty-based optimization," *IEEE Robotics and Automation Letters*, vol. 4, no. 4, pp. 4147–4154, 2019.

[76] O. F. Argin and Z. Y. Bayraktaroglu, "Consistent dynamic model identification of the stäubli rx-160 industrial robot using convex optimization method," *Journal of Mechanical Science and Technology*, vol. 35, no. 5, pp. 2185–2195, 2021.

[77] T.-H. Kim, I. Maruta, and T. Sugie, "Robust pid controller tuning based on the constrained particle swarm optimization," *Automatica*, vol. 44, no. 4, pp. 1104–1110, 2008.

[78] R. E. Perez, P. W. Jansen, and J. R. Martins, "pyopt: a python-based object-oriented framework for nonlinear constrained optimization," *Structural and Multidisciplinary Optimization*, vol. 45, no. 1, pp. 101–118, 2012.

[79] A. C. Bittencourt, E. Wernholt, S. Sander-Tavallaey, and T. Brogårdh, "An extended friction model to capture load and temperature effects in robot joints," *Proc. IEEE/RSJ International Conference on Intelligent Robots and Systems*, pp. 6161–6167, 2010.

[80] C. L. Lawson and R. J. Hanson, *Solving least squares problems.* SIAM, 1995.

[81] M. Gautier and W. Khalil, "Exciting trajectories for the identification of base inertial parameters of robots," *The International Journal of Robotics Research*, vol. 11, no. 4, pp. 362–375, 1992.

[82] J. Swevers, C. Ganseman, D. B. Tukel, J. De Schutter, and H. Van Brussel, "Optimal robot excitation and identification," *IEEE transactions on robotics and automation*, vol. 13, no. 5, pp. 730–740, 1997.

[83] A. De Luca and R. Mattone, "Actuator failure detection and isolation using generalized momenta," *Proc. IEEE International Conference on Robotics and Automation*, pp. 634–639, 2003.

[84] ——, "Sensorless robot collision detection and hybrid force/motion control," *Proc. IEEE International Conference on Robotics and Automation*, pp. 999–1004, 2005.

[85] M. E. Hagen, J. J. Meehan, I. Inan, and P. Morel, "Visual clues act as a substitute for haptic feedback in robotic surgery," *Surgical Endoscopy*, vol. 22, no. 6, pp. 1505–1508, 2008.

[86] J. K. Koehn and K. J. Kuchenbecker, "Surgeons and non-surgeons prefer haptic feedback of instrument vibrations during robotic surgery," *Surgical Endoscopy*, vol. 29, no. 10, pp. 2970–2983, 2015.

[87] A. Banach, K. Leibrandt, M. Grammatikopoulou, and G. Yang, "Active Constraints for Tool-Shaft Collision Avoidance in Minimally Ivasive Surgery," *Proc. IEEE International Conference on Robotics and Automation*, pp. 1556–1562, 2019.

[88] G. A. Fontanelli, F. Ficuciello, L. Villani, and B. Siciliano, "Modelling and identification of the da Vinci Research Kit robotic arms," *Proc. IEEE/RSJ International Conference on Intelligent Robots and Systems*, pp. 1464–1469, 2017.

[89] P. Kazanzides, Z. Chen, A. Deguet, G. S. Fischer, R. H. Taylor, and S. P. DiMaio, "An open-source research kit for the da Vinci®Surgical System," *Proc. IEEE International Conference on Robotics and Automation*, pp. 6434–6439, 2014.

[90] B. K. Horn, "Closed-form solution of absolute orientation using unit quaternions," *Journal of the Optical Society of America A*, vol. 4, no. 4, pp. 629–642, 1987.

[91] O. Ronneberger, P. Fischer, and T. Brox, "U-Net: Convolutional Networks for Biomedical Image Segmentation," *Proc. International Conference on Medical Image Computing and Computer-Assisted Intervention - MICCAI 2015*, pp. 234–241, 2015.

[92] A. A. Shvets, A. Rakhlin, A. A. Kalinin, and V. I. Iglovikov, "Automatic Instrument Segmentation in Robot-Assisted Surgery using Deep Learning," *Proc. 17th IEEE International Conference on Machine Learning and Applications*, pp. 624–628, 2018.

[93] V. Lepetit, F. Moreno-Noguer, and P. Fua, "EPnP: An Accurate O(n) Solution to the PnP Problem," *International Journal of Computer Vision*, vol. 81, no. 2, p. 155, 2008.

[94] S. G. Hart and L. E. Staveland, "Vision-based suturing needle tracking with extended kalman filter," *Proc. Computer/Robot Assisted Surgery Workshop*, 2017.

[95] ——, "Development of nasa-tlx (task load index): Results of empirical and theoretical research," *Advances in Psychology*, vol. 52, pp. 139–183, 1988.

[96] N. Hogan, "Impedance control: An approach to manipulation: Part i—theory," *Journal of Dynamic Systems Measurement and Control*, 1985.

[97] ——, "Impedance control: An approach to manipulation: Part ii—implementation," *Journal of Dynamic Systems Measurement and Control*, 1985.

[98] A. Cirillo, F. Ficuciello, C. Natale, S. Pirozzi, and L. Villani, "A conformable force/tactile skin for physical human–robot interaction," *IEEE Robotics and Automation Letters*, vol. 1, no. 1, pp. 41–48, 2016.

[99] J. Redmon, S. Divvala, R. Girshick, and A. Farhadi, "You only look once: Unified, real-time object detection," in *Proceedings of the IEEE conference on computer vision and pattern recognition*, 2016, pp. 779–788.

[100] M. Yip and N. Das, "Robot autonomy for surgery," in *The Encyclopedia of MEDICAL ROBOTICS: Volume 1 Minimally Invasive Surgical Robotics*. World Scientific, 2019, pp. 281–313.

[101] C. D'Ettorre, A. Mariani, A. Stilli, F. R. y Baena, P. Valdastri, A. Deguet, P. Kazanzides, R. H. Taylor, G. S. Fischer, S. P. DiMaio *et al.*, "Accelerating surgical robotics research: A review of 10 years with the da vinci research kit," *IEEE Robotics & Automation Magazine*, vol. 28, no. 4, pp. 56–78, 2021.

[102] J. D. Birkmeyer, J. F. Finks, A. O'reilly, M. Oerline, A. M. Carlin, A. R. Nunn, J. Dimick, M. Banerjee, and N. J. Birkmeyer, "Surgical skill and complication rates after bariatric surgery," *New England Journal of Medicine*, vol. 369, no. 15, pp. 1434–1442, 2013.

[103] S. E. Regenbogen, C. C. Greenberg, D. M. Studdert, S. R. Lipsitz, M. J. Zinner, and A. A. Gawande, "Patterns of technical error among surgical malpractice claims: an analysis of strategies to prevent injury to surgical patients," *Annals of surgery*, vol. 246, no. 5, pp. 705–711, 2007.

[104] G. A. Fontanelli, M. Selvaggio, L. R. Buonocore, F. Ficuciello, L. Villani, and B. Siciliano, "A new laparoscopic tool with in-hand rolling capabilities for needle reorientation," *IEEE Robotics and Automation Letters*, vol. 3, no. 3, pp. 2354–2361, 2018.

[105] M. Levin, T. McKechnie, S. Khalid, T. P. Grantcharov, and M. Goldenberg, "Automated methods of technical skill assessment in surgery: A systematic review," *Journal of Surgical Education*, vol. 76, no. 6, pp. 1629–1639, 2019. [Online]. Available: https://www.sciencedirect.com/science/article/pii/S1931720419301643

[106] Y. Gao, S. S. Vedula, C. E. Reiley, N. Ahmidi, B. Varadarajan, H. C. Lin, L. Tao, L. Zappella, B. Béjar, D. D. Yuh *et al.*, "Jhu-isi gesture and skill assessment working set (jigsaws): A surgical activity dataset for human motion modeling," in *MICCAI workshop: M2cai*, vol. 3, no. 3, 2014.

[107] E. Colleoni, P. Edwards, and D. Stoyanov, "Synthetic and real inputs for tool segmentation in robotic surgery," in *International Conference on Medical Image Computing and Computer-Assisted Intervention.* Springer, 2020, pp. 700–710.

[108] I. Rivas-Blanco, C. J. P. Del-Pulgar, A. Mariani, G. Tortora, and A. J. Reina, "A surgical dataset from the da vinci research kit for task automation and recognition," in *2023 3rd International Conference on Electrical, Computer, Communications and Mechatronics Engineering (ICECCME)*, 2023, pp. 1–6.

[109] M. Zheng, M. S. Crouch, and M. S. Eggleston, "Surface electromyography as a natural human–machine interface: a review," *IEEE Sensors Journal*, vol. 22, no. 10, pp. 9198–9214, 2022.

[110] K. Takayasu, K. Yoshida, T. Mishima, M. Watanabe, T. Matsuda, and H. Kinoshita, "Upper body position analysis of different experience level surgeons during laparoscopic suturing maneuvers using optical motion capture," *The American Journal of Surgery*, vol. 217, no. 1, pp. 12–16, 2019.

[111] F. Lalys and P. Jannin, "Surgical process modelling: a review," *International journal of computer assisted radiology and surgery*, vol. 9, pp. 495–511, 2014.

[112] O. Dergachyova, "Knowledge-based support for surgical workflow analysis and recognition," Ph.D. dissertation, Université Rennes 1, 2017.

[113] M. Maktabi and T. Neumuth, "Online time and resource management based on surgical workflow time series analysis," *International journal of computer assisted radiology and surgery*, vol. 12, pp. 325–338, 2017.

[114] T. N. Judkins, D. Oleynikov, and N. Stergiou, "Objective evaluation of expert and novice performance during robotic surgical training tasks," *Surgical endoscopy*, vol. 23, pp. 590–597, 2009.

[115] T. D. Nagy and T. Haidegger, "A dvrk-based framework for surgical subtask automation," *Acta Polytechnica Hungarica*, pp. 61–78, 2019.

[116] A. De Luca and R. Mattone, "Sensorless robot collision detection and hybrid force/motion control," in *Proceedings of the 2005 IEEE international conference on robotics and automation.* IEEE, 2005, pp. 999–1004.

[117] R. Moccia, C. Iacono, B. Siciliano, and F. Ficuciello, "Vision-based dynamic virtual fixtures for tools collision avoidance in robotic surgery," *IEEE Robotics and Automation Letters*, vol. 5, no. 2, pp. 1650–1655, 2020.

Author’s Publications

The works presented in this thesis has been published in the following articles:

- R. Moccia, **C. Iacono**, B. Siciliano and F. Ficuciello, "Vision-Based Dynamic Virtual Fixtures for Tools Collision Avoidance in Robotic Surgery" in IEEE Robotics and Automation Letters, vol. 5, no. 2, pp. 1650-1655, April 2020.
- **C. Iacono**, R. Moccia, B. Siciliano, F. Ficuciello, ”Vision-Based Dynamic Virtual Fixtures for Tools Collision Avoidance in MIRS”, 10th Joint Workshop on New Technologies for Computer/Robot Assisted Surgery, Barcelona, Spain, September 28-30, 2020.
- **C. Iacono**, R. Moccia, B. Siciliano, F. Ficuciello, ”Forbidden Region Virtual Fixtures for Surgical Tools Collision Avoidance”, Proc. Institute for Robotics and Intelligent Machine Conference, Rome, Italy, October 18-20, 2020.
- **C. Iacono**, S. Moccia, A. Marzullo, E. De Momi, U. Bracale, F. Ficuciello, "Deep learning-based localization of the biliary tract in laparoscopic images acquired during surgical robotic procedures", Proc. Institute for Robotics and Intelligent Machine Conference, Rome, Italy, October 8-10, 2021.
- **C. Iacono**, S. Moccia, A. Marzullo, E. De Momi, F. Ficuciello, U. Bracale, "Deep learning-based localization of the biliary tract on white-light images acquired during laparoscopic cholecystectomy", 11th Joint Workshop on New Technologies for Computer/Robot Assisted Surgery, Naples, Italy, April 25-27, 2022.
- M. Caianiello, **C. Iacono**, A. Imperato, F. Ficuciello, "Deep Deterministic Policy Gradient from Success: A New Approach for Robot-Assisted Suturing", Proc. Institute for Robotics and Intelligent Machine Conference, Rome, Italy, October 20-22, 2023.

- M. Caianiello, **C. Iacono**, A. Imperato, F. Ficuciello, "Exploring the Use of Deep Reinforcement Learning Algorithms for Wound-Approaching Trajectories in Robot-Assisted Minimally Invasive Surgery", 2023 21th International Conference on Advanced Robotics (ICAR), Abu Dhabi, United Arab Emirates, 2023
- C. Pecorella, **C. Iacono**, B. Siciliano, F. Ficuciello. "Human-Robot Interactive Framework with Remote Center of Motion and Virtual Fixtures for Minimally Invasive Robotic Surgery", 2024 International Symposium on Advances in Robot Kinematics.
- **C. Iacono**, M. Caianiello, S. Bartiromo, A. Smaldone, F. Ficuciello, "Design and Validation of a Multimodal Dataset of Robot-Assisted Suturing Gestures based on Kinematic and Force Information", submitted to 2024 IEEE International Conference on Advanced Robotics and Its Social Impacts.
- M. Caianiello, M. Ricci, A. Smaldone, S. Hussain, **C. Iacono**, F. Ficuciello, "Optimizing Safety and Efficiency in the Suturing Task: A Comparison of Model Predictive Control and Control Barrier Function Framework", submitted to 2024 IEEE International Conference on Advanced Robotics and Its Social Impacts.
- O. F. Argin, R. Moccia, **C. Iacono**, F. Ficuciello, "da Vinci Research Kit Patient Side Manipulator Dynamic Model using Augmented Lagrangian Particle Swarm Optimization", submitted to IEEE Transaction on Medical Robotics and Bionics.